

Comparing low-mass and high-mass protostellar
outflows

MSc thesis

Femke Ballieux



Universiteit
Leiden
Observatory

Comparing low-mass and high-mass protostellar outflows

A thesis submitted in partial fulfillment
of the requirements for the degree of

Master of Science
in
Astronomy

Author:
Student ID:
Supervisor:
Second supervisor:
Second corrector:
Project duration:

Femke Ballieux
s2124149
Prof.dr. S. Viti
Dr. M.M.E. Bouvier
Dr. M.R. Hogerheijde
February 2024 – December 2024

Cover image:
Template style:
Template licence:

Night sky by Evgeni Tcherkasski
Thesis style by Richelle F. van Capelleveen
Licenced under CC BY-NC-SA 4.0



Universiteit
Leiden
Observatory

P.O. Box 9513, 2300 RA Leiden, The Netherlands

Abstract

To be written

Acknowledgements

To be written

Contents

Abstract	iii
Acknowledgements	iv
List of Tables	vii
List of Figures	viii
1 Introduction	1
1.1 High- and low-mass star formation	1
1.2 Protostellar outflows	4
1.3 Aims of this research	8
2 Observations	10
2.1 High-mass protoclusters	10
2.2 Low-mass protoclusters	12
3 Rotational temperatures and CO column densities	15
3.1 Methodology	15
3.1.1 Inspecting the datacubes	15
3.1.2 Smoothing and regridding	15
3.1.3 Integrated emission maps	15
3.1.4 Determination of noise levels and clipping	16
3.1.5 Local thermodynamic equilibrium	17
3.1.6 Radiative transfer	18
3.1.7 Rotation diagram method	19
3.1.8 T_{rot} and $N_{\text{tot}}(\text{CO})$ determination	20
3.2 Results	21
3.2.1 Optically thick transitions in high-mass fields	21
3.2.2 Non-LTE or multiple component emission in low-mass fields	22

4 Morphology and outflow properties	25
4.1 Methodology	25
4.1.1 Integrated CO (2-1) maps	25
4.1.2 Outflow classifications	25
4.1.3 Radius determination	25
4.1.4 Outer velocity determination	26
4.1.5 Dynamical age determination	26
4.1.6 Opening angle determination	27
4.2 Results	29
4.2.1 Radii, velocities, and dynamical timescales	30
4.2.2 Opening angles	31
4.2.3 Details of individual outflows	31
5 Discussion	39
5.1 High-mass outflows might be warmer than low-mass outflows.	39
5.2 High-mass fields have more molecular material than low-mass outflows	40
5.3 High-mass outflows are larger and move faster than low-mass outflows	42
5.4 High-mass outflows show longer periods of dynamical activity than low-mass outflows	43
5.5 High-mass outflows are more collimated than low-mass outflows	45
5.6 The evolution of opening angles with age	46
6 Conclusions	49
A Appendix	50
A.1 Constraining the physical high-mass parameters using <i>RADEX</i>	50
A.2 LTE rotational temperature and column density maps	52
A.3 Angle determination plots	52
Bibliography	66

List of Tables

2.1	Overview of the observations of the high-mass sample	12
2.2	Overview of the observations of the low-mass sample	14
3.1	The velocity ranges over which the CO emission was integrated	17
4.1	The morphological parameters for all outflows in this work	30

List of Figures

1.1	Overview of the constituents of a molecular cloud	2
1.2	Overview of the evolutionary sequence low-mass stars	3
1.3	Overview of different stages of high-mass star formation	4
1.4	Overview of a protostellar outflow	5
1.5	A proposed evolutionary sequence for the widening of high-mass protostellar outflow with time	8
2.1	Overview of the high-mass protoclusters studied in this work	11
2.2	JWST NIRCam image of the ρ Ophiuchi cloud complex	13
3.1	CO (2-1) red-shifted integrated emission of the high-mass source G008.67	16
3.2	Example of a well-behaved rotational diagram of CO	20
3.3	T_{rot} and $N_{tot}(\text{CO})$ maps for G338.93.	23
3.4	Example of a deviated rotational diagram of CO	24
4.1	Integrated blue- and red-shifted CO (2-1) emission showing the G328.25 outflow	28
4.2	Integrated blue- and red-shifted CO (2-1) emission showing the Oph 26 outflow	29
4.3	Integrated blue- and red-shifted CO (2-1) maps maps of sources in our low-mass sample.	32
4.4	Integrated blue- and red-shifted CO (2-1) maps of sources in our low-mass and high-mass sample.	33
4.5	Integrated blue- and red-shifted CO (2-1) maps maps of sources in our high-mass sample.	34
5.1	Mean values of the rotational temperatures	40
5.2	Mean column densities over the high- and low-mass fields	41
5.3	Dynamical timescales	44
5.4	Opening angles	45
5.5	Opening angles of low-mass and high-mass outflow lobes	47

5.6 The opening angles of low-mass outflow lobes, as a function of the evolutionary stage	48
---	----

1. Introduction

1.1 High- and low-mass star formation

Understanding star formation is at the core of the majority of contemporary astronomical research. Stars are the building blocks of the universe, star formation determines the structure and evolution of galaxies, almost all elements around us have been formed in stars, and the formation of planets is intrinsically linked to star formation.

Low-mass stars ($M \lesssim 8 M_{\odot}$) are the most abundant, since they dominate the initial mass function (IMF), which is the distribution of stellar masses as they reach the main sequence (e.g. Kroupa, 2002; Chabrier, 2003). High-mass stars ($M \gtrsim 8 M_{\odot}$) are much rarer, constituting less than approximately 1% of IMF Rosen et al. (2020). However because of their extremely large luminosities ($> 2 \cdot 10^3 L_{\odot}$, Kuiper, 1938) and mechanical impact on their environments (such as stellar winds and ionization), they play a dominant role in all kinds of processes (Tan et al., 2014). Examples are the reionization of the universe and the evolution of galaxies. They further regulate the ISM by producing heavy elements, which are injected into the ISM through supernova explosions (e.g. Woosley et al., 2002). Furthermore, they enrich the ISM with dust (Dunne et al., 2003). Through feedback processes, they might also play a role in dispersing stellar clusters (Fall et al., 2010).

Although the process of low-mass star formation ($M \lesssim 8 M_{\odot}$) is quite well understood, the details of high-mass star formation process are still widely debated (e.g. Tan et al., 2014), due to the rarity of high-mass stars and their consequent greater distance.

Star formation is a complex process, that occurs in large ($L \sim 10$ pc), dense ($N_H \gtrsim 10^3 \text{ cm}^{-3}$), and cold ($T \sim 10$ K) giant molecular clouds (GMC) (e.g. Lada & Lada, 2003; Rosen et al., 2020). These clouds have a hierarchical structure, with increasing densities towards smaller structures.

A widely discussed hypothesis is that high-mass stars form through a scaled-up version of low-mass star formation (Shu et al., 1987). GMCs contain networks of filaments and clumps with a scale of ~ 1 pc and higher densities than the surrounding cloud. Within these clumps, gravitationally bound dense cores exist with typical sizes 0.1 pc. If these cores become gravitationally unstable, they undergo gravitational collapse via a central disk, to form one or multiple low-mass

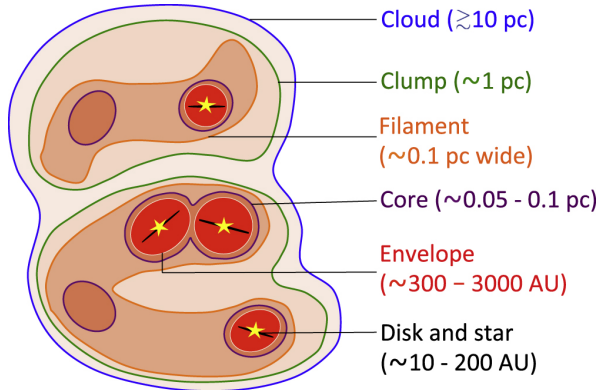


Figure 1.1: Schematic overview of the constituents of a molecular cloud, showing the low-mass star formation mechanism, in which clumps fragment into cores, which undergo gravitational collapse to eventually form stars. The image is not drawn to scale. Figure taken from Pokhrel et al. (2018).

young stellar objects (YSOs), with a surrounding envelope. The core in which the YSO has formed is then referred to as a protostellar core. In Figure 1.1, a schematic overview of the different stages of low-mass star formation is given.

The scenario in which high-mass stars form through a scaled-up version of the low-mass star formation model is called the 'Core Accretion' model. Similarly to low-mass star formation, self-gravitating, centrally concentrated cores form from a fragmenting clump. As these cores undergo gravitational collapse through a central disk, one or multiple high-mass YSOs form. In this scenario, the core represents the entire mass reservoir available for the formation of one massive, or multiple low-mass stars, and no mass is accreted from outside the core. A distinguishing feature of the Core Accretion model is that the shape of the pre-stellar core-mass function (CMF) is the same as the shape of the initial mass function (IMF) (e.g. Tan et al., 2014).

Another widely considered hypothesis for high-mass star formation is 'Competitive Accretion' (Bonnell et al., 2001), in which high-mass stars accrete their mass chaotically from a wider region of the clump, that has never formed a consistent, gravitationally bound core. In this scenario, accretion occurs more efficiently near the center of the gravitational potential, and therefore the most massive stars would form in the center of a cluster. According to this model, high-mass stars would always form in a cluster in which the mass is dominated by low-mass stars, indicating that high- and low-mass stars form simultaneously. If the density of stars in the cluster center is sufficiently high, collisions might also assist in the formation of extremely massive stars. Competitive Accretion has been said to naturally produce the IMF (Bonnell et al., 2001), where massive stars form only a small fraction of the total stars formed. Observations show that high-mass star formation occurs in clustered environments, characterized by higher surface densities and larger velocity dispersions (e.g. Tan et al., 2014; Zhang et al., 2015), which might be evidence for the Competitive Accretion model.

Low-mass YSOs are most often classified based on their infra-red spectral

slope (Lada, 1987; Andre & Montmerle, 1994; Greene et al., 1994), where Class 0 YSOs represent the earliest, deeply embedded stage of star formation. Class I sources are slightly more evolved YSOs, and Class II sources are T Tauri stars with gas-rich circumstellar disks.

A different low-mass YSO classification mechanism has been proposed (Whitney et al., 2003; Robitaille et al., 2006) that is based on physical characteristics, rather than observational properties. According to this mechanism, sources are either stage 0 in which they are deeply embedded, stage 1 in which they are less embedded, stage 2 in which they are classical T Tauri stars with gas-rich disks, and stage 3 in which they are main-sequence stars. An overview of the different evolutionary stages of low-mass YSOs is given in Figure 1.2.

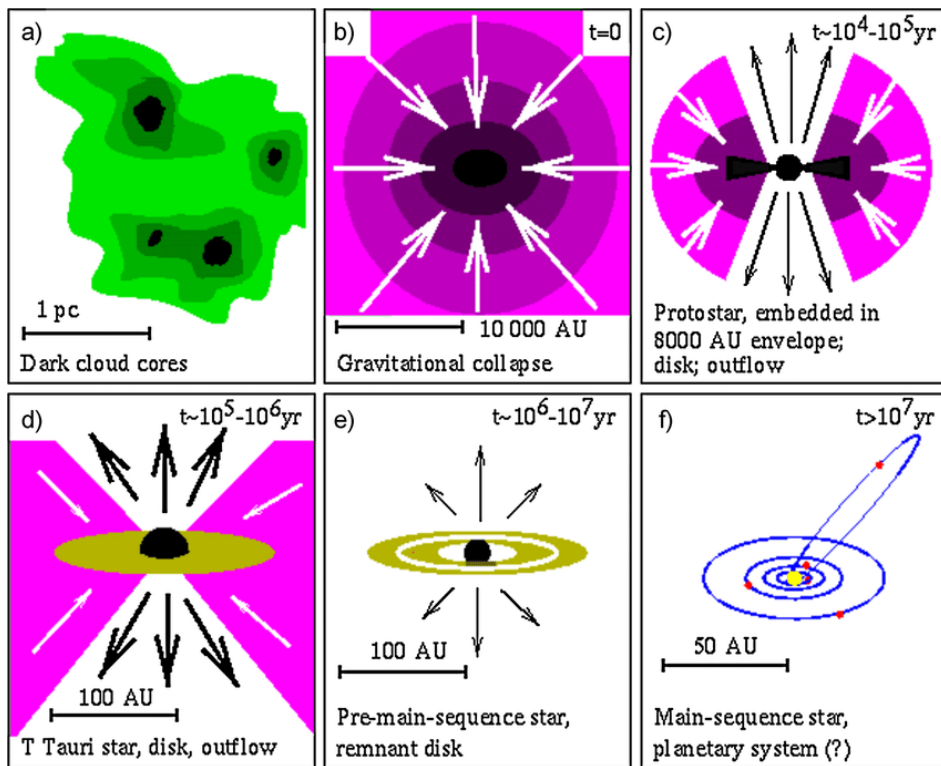


Figure 1.2: Schematic overview of the evolutionary sequence of a low-mass star. As cores undergo gravitational collapse, a protostar embedded in an envelope forms, accompanied by a disk and protostellar outflows. These protostars eventually evolve into T Tauri stars, which still have a disk and outflows. Eventually, a pre-main-sequence star forms, which evolves into a main-sequence star. The image was taken from Hogerheijde (1998).

An evolutionary sequence for high-mass star formation has been proposed (e.g. Walsh et al., 1999; Minier et al., 2003), which differs from the evolutionary sequence of low-mass star formation. After the initial collapse, the newly formed protostar will begin emitting UV photons. These photons cause the surrounding envelope to ionize, which is referred to as an ultra-compact HII (UCHII) region. As the ionization front expands, it forms a giant HII region. Eventually the surrounding gas is blown away, revealing a high-mass star cluster. An overview of this evolutionary sequence can be found in Figure 1.3.

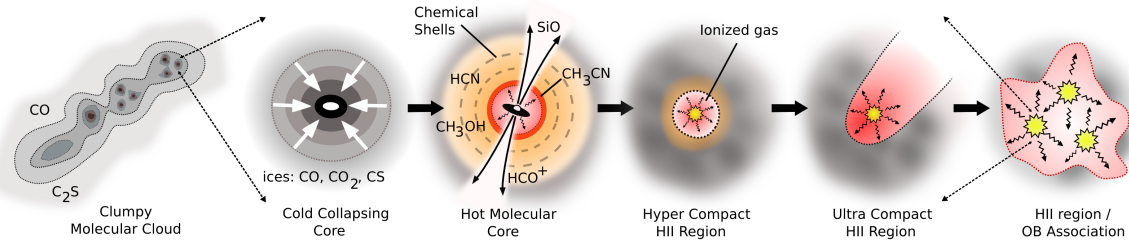


Figure 1.3: Schematic overview of different stages of high-mass star formation. Clumpy molecular clouds collapse through cold cores to hot cores, at which point protostellar outflows and heat from the central protostar evaporates ices from grains, causing a rich time-dependent chemistry. Due to UV photons emitted by the protostar, the surrounding medium becomes ionized (HII region). Massive stars often form in clusters. Image adapted from Purcell (2006)

1.2 Protostellar outflows

In the vicinity of the vast majority of both high- and low-mass YSOs, bipolar molecular outflows of high-velocity gas are detected (e.g. Bally & Lada, 1983; Edwards & Snell, 1982, 1983, 1984). These protostellar outflows consist of a range of morphologies, from collimated jets to less-collimated lobes, to barely-collimated spherical winds (Reipurth & Bally, 2001; Arce et al., 2011; Arce et al., 2013; Nakamura & Li, 2012). They range in velocity from a few km s⁻¹ to over 10³ km s⁻¹. Shocks further complicate the morphology of the outflow.

Their exact launching mechanism is still under debate (e.g. Bachiller, 1996; Tan et al., 2014), but for low-mass sources it is generally accepted that magnetocentrifugal acceleration from the disk region launches a jet, which entrains gas from the surrounding envelope (Bally, 2016; Pudritz & Ray, 2019). High-mass outflows rely on additional mechanisms, such as accretion via stellar collisions (Bonnell et al., 1998), radiative Rayleigh-Taylor instabilities (Krumholz & Matzner, 2009; Rosen et al., 2016), or dense filaments (Rosen et al., 2016). Protostellar outflows can be observed around low-mass sources from Class 0 to Class II sources (e.g. Bachiller, 1996; Bally, 2016). Although high-mass YSOs are rare, it has been found that protostellar outflows are ubiquitous around high-mass protostars as well (Beuther et al., 2002). Outflows are associated with significant mass loss. Low mass Class 0 YSOs have been seen to have a mass-loss rate up to $\sim 10^{-5} M_{\odot} \text{ yr}^{-1}$ (Bally, 2016), and high-mass outflows have been shown to have mass-loss rates from 10^{-5} to a few $\times 10^{-3} M_{\odot} \text{ yr}^{-1}$ (Arce & Sargent, 2006).

A natural consequence of star formation is the launching of protostellar outflows, as these carry away angular momentum that would otherwise prevent core collapse. Conversely, protostellar outflows can start a negative feedback process, by clearing the dense gas surrounding the YSO, which limits further accretion (e.g. Nakano et al., 1995; Matzner & McKee, 2000; Hansen et al., 2012; Cunningham et al., 2018; Rohde et al., 2020). Therefore, these outflows likely set

the star formation efficiency, which has been estimated to be $\sim 0.3 - 0.5$ (Alves et al., 2007; Enoch et al., 2008; Könyves et al., 2015, 2020).

Protostellar outflows are most often observed using low-J pure rotational transitions of CO. CO is abundant, the upper-energy levels of the lowest transitions are easily populated by collisions, and the rotational transitions trace the typical temperatures and column densities of molecular clouds. Furthermore, these CO rotational transitions are observable from the ground. Warmer regions in the outflows, such as shocks, are often traced by higher-J pure rotational transitions of CO, and by SiO, as these shocks can cause grain sputtering, which increases the abundance of SiO significantly compared to the surrounding cold gas (e.g. Schilke et al., 1997; Caselli et al., 1997; Gusdorf et al., 2008).

A schematic overview of the components of a protostellar outflow can be found in Figure 1.4, although it should be noted that real outflows are often more complex than indicated in the figure, since interactions with the ISM, episodic activity and neighboring YSOs influence the shape of the outflow.

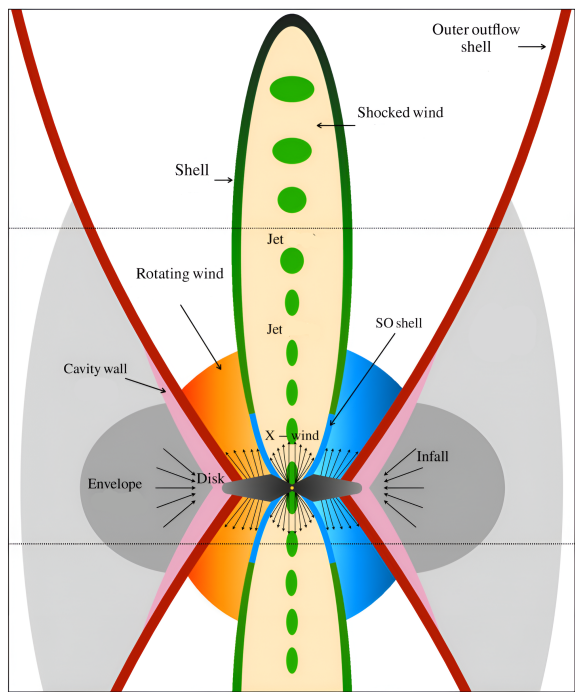


Figure 1.4: Schematic overview of a protostellar outflow, adapted from López-Vázquez et al. (2024). Indicated are the envelope, the protostellar disk, the jet, the outflow, and the infall regions. Further indicated are the shocked wind, the SO shell, a rotating wind, and the X-wind, which are components we do not further discuss in this thesis. Not indicated are possible cavities within the outflow.

Outflow temperatures

Rotational temperatures for (low-mass) outflows are usually determined using low-J ($J_u \leq 3$) pure rotational lines of CO and CO isotopologues in the mm and sub-mm regime. These lines trace the cold gas ($T_{\text{ex}} \leq 10 - 50$ K) in the outflow

and the envelope (e.g. Lada, 1985; Blake et al., 1995; Bontemps et al., 1996; Yıldız et al., 2012; Dunham et al., 2014). Observations of high excitation lines of CO trace warmer gas and find cavity walls with temperatures of $T \sim 100$ K (Yıldız et al., 2012). There are thus multiple different components of the outflow and envelope, with a range of temperatures. In this project, we only study low-J transitions, and therefore only trace the colder component.

Van Kempen et al. (2016) study intermediate-mass outflows and find temperature limits of $T_{\text{ex}} \lesssim 50$ K, which is in agreement with temperature limits found for low-mass protostars.

Due to the rarity of high-mass YSOs, no general temperature range is known for high-mass outflows. McKee & Tan (2003) state that once a massive star is formed, temperatures of the surrounding gas may rise to $T \sim 50 - 100$ K, however at earlier stages they emerge from gas that has the same temperature range as low-mass stars.

Outflow column densities

Tychoniec et al. (2019) study five outflow sources in the Serpens Main star-forming region, two low-mass YSOs, and one (SMM1, a multiple system containing three outflow-hosting sources) is in between a low-mass and an intermediate-mass outflow. They determine CO column densities separately for slow, fast, and extremely high velocity (EHV) outflows. For the low-mass outflows, they find that the slow outflows have CO column densities ranging from $4 \cdot 10^{16}$ to $5 \cdot 10^{17} \text{ cm}^{-2}$, while the fast outflows have CO column densities ranging between $5 \cdot 10^{15}$ and $3 \cdot 10^{17} \text{ cm}^{-2}$. For the slightly more massive outflows (although not yet high-mass outflows), they find the slow outflows have CO column densities ranging between $6 \cdot 10^{16}$ and $6 \cdot 10^{17} \text{ cm}^{-2}$, while the fast outflows have CO column densities ranging between $1 \cdot 10^{16}$ and $3 \cdot 10^{17} \text{ cm}^{-2}$.

Lefloch et al. (2015) study the Cepheus E protostellar outflow, which is an intermediate-mass outflow. They find that the emission traced by low-J CO lines is cold ($T_{\text{kin}} = 80 - 100$ K), with a typical column density of $N(\text{CO}) = 9 \cdot 10^{16} \text{ cm}^{-2}$, while the emission traced by high-J lines is warm ($T_{\text{kin}} = 400 - 750$ K) with lower column densities $N(\text{CO}) = 1.5 \cdot 10^{16} \text{ cm}^{-2}$.

Although a specific range for low-J CO column densities is not known for high-mass protostellar outflows due to their rarity, Li et al. (2018) find that properties like outflows mass, momentum, and energy are typically two orders of magnitude higher for their high-mass outflows, compared to typical values for low-mass outflows. Therefore, we expect high-mass sources to have higher CO column densities than low-mass sources.

Dynamical timescales

In many protostellar outflows, a 'Hubble-like' relationship in outflows between velocity and distance to the YSO has been observed (e.g. Stahler, 1994; Lada & Fich, 1996), where the velocity of the outflow increases linearly with the distance from the YSO. Such a relationship suggests that the dynamical timescale, defined as the radius divided by the velocity of an outflow, remains constant throughout

the outflow.

Outflows are associated with accretion and can be highly episodic, on timescales from weeks to years (e.g. Billot et al., 2012; Safron et al., 2015; Mairs et al., 2017). Mass loss from protostellar outflows seems to increase with accretion rate (e.g. Ellerbroek et al., 2013). Li et al. (2020) find that the time between consecutive ejection events, and therefore episodic accretion events, decreases as a source evolves. They also find that the dynamical timescale increases with core masses, which indicates that more massive cores have longer accretion timescales than less massive cores. Therefore, we expect outflows in our high-mass sample to have longer dynamical timescales.

Opening angles

In low-mass protostars, the increase of the opening angle with age seems to be a general trend, which has been shown both observationally and through simulations (e.g. Velusamy & Langer, 1998; Arce & Sargent, 2006; Lee & Ho, 2005). As a source matures, the outflow becomes less collimated, until outflows around Class II sources have no definable structure.

Staff et al. (2019) find a similar relation for high-mass sources from 3D magnetohydrodynamic simulations. They find that as the high-mass sources evolve and accrete more mass, their opening angles increase as well. They state that the reason for this widening is likely related to the outflow eroding the protostellar envelope and widening the outflow cavity over time.

Richer et al. (2000) find a lack of well-collimated outflows in samples of high-mass protostellar outflows, suggesting low-mass outflows have smaller opening angles than high-mass outflows. However, this result might be biased by selection effects, as relatively few massive outflows were identified at the time. Wu et al. (2004) study a sample of low- and high-mass protostellar outflows, and determine the collimation factor of these outflows by considering the outflow to be an ellipsoid, calculating the area and the major axis, and then deriving the minor axis. The ratio between the major and minor axes is the collimation factor. They find average collimation factors of 2.05 ± 0.96 for the high-mass sample, and 2.81 ± 2.16 for the low-mass sample, and therefore find that low-mass protostellar outflows are more collimated than high-mass outflows. Beuther et al. (2002) disagree with these findings, and instead find similar collimation factors between high- and low-mass protostellar outflows.

Beuther & Shepherd (2005) indicate several different reasons for this discrepancy; either some observations were wrongly interpreted, there exist multiple physically different modes of massive star formation, or the observed sources might not be comparable due to different evolutionary stages. The first might be true for some single-dish observations since low spatial resolution can significantly bias the determination of opening angles. Furthermore, the bias in distance to high-mass outflows, and unknown inclinations, could influence the determined opening angles. However, high-resolution observations also show contradictory results in terms of opening angles in high-mass outflows. It is possible that multiple modes of high-mass star formation exist, however a link

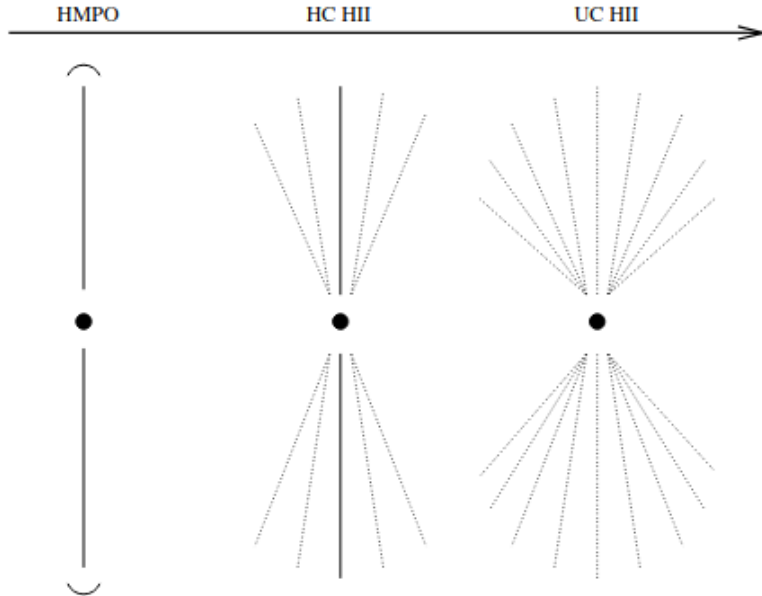


Figure 1.5: A proposed evolutionary sequence for the widening of high-mass protostellar outflows with time. A jet-like outflows dominates initially, until in a hyper-compact HII (HC HII) region forms, that launched an additional wide-angled wind component. Eventually an UC HII region forms, and the winds start to dominate. Image was taken from Beuther & Shepherd (2005).

between accretion and outflows has been established between different spectral types, making it unlikely that there is more than one mechanism to form high-mass stars. Therefore it is more likely that different evolutionary stages cause the contradiction in observed high- and low-mass opening angles. An evolutionary scenario is proposed by Beuther & Shepherd (2005), in which a very early massive protostar, that is not surrounded by an UC HII region, is able to launch a well-collimated jet-like outflow. Eventually winds from the massive protostar launch an additional wider-angled component. Finally, an UC HII region forms, and the wide-angled winds begin to dominate over the entire system. An overview of this evolutionary sequence is given in Figure 1.5.

In recent work, Mignon-Risse et al. (2021) perform radiation-magnetohydrodynamic (RMHD) simulations on high-mass protostellar outflows, and they find smaller opening angles than the opening angles observed by Wu et al. (2004) and Beuther et al. (2002), in a range of 20–30° when magnetic fields dominate, and a range of 30–70° overall. Their simulated opening angles are larger than those of collimated jets but smaller than wide-angle outflows.

1.3 Aims of this research

In this project, we study a sample of high- and low-mass star forming regions, using CO observations from the Atacama Large Millimeter/Submillimeter Array (ALMA), which is especially well suited for research into outflows due to its

high spectral and spatial resolution. We aim to determine whether there are differences in the outflow properties of these high- and low-mass YSOs, and to couple these potential differences back to various theories of high- and low-mass star formation.

Our high-mass sample consists of five high-mass protostellar clusters, selected from the ALMA-IMF program (e.g. Motte et al., 2022). Our low-mass sample consists of seven YSOs in the ρ Ophiuchi molecular cloud. We will introduce these samples in Chapter 2. In Chapter 3, we determine rotational temperatures and column densities for all outflows in our fields. In Chapter 4 we determine outflow properties such as radii, dynamical timescales and opening angles. We compare our results with each other and with literature in Chapter 5. Conclusions are found in Chapter 6.

2. Observations

2.1 High-mass protoclusters

The five high-mass protoclusters considered in this project were selected from the ALMA-IMF sample (e.g. Motte et al., 2022, , project code 2017.1.01355.L). The ALMA-IMF sample consists of 15 high-mass ($2.5 \cdot 10^3 - 33 \cdot 10^3 M_{\odot}$), nearby (2–5.5 kpc) protoclusters in various evolutionary stages. A wide range of spectral lines have been observed with ALMA, including the CO (2-1) line. For a full description of the observational setup, see Motte et al. (2022).

In this project, we selected a sub-sample of the ALMA-IMF sample consisting of sources with additional higher-J level ALMA CO measurements, which yielded six sources with additional CO (3-2) observations. One protocluster (G327.29) was removed from this sample as the resolution of the available CO (3-2) observation was low (3.673"). The project codes for the CO (3-2) observations are 2018.1.01679.S for G328.25, and 2017.1.00914.S for the other four sources, (PI: Csengeri). The high-mass sample that was left thus consisted of five protoclusters with CO (2-1) and CO (3-2) observations. Observational details of the high-mass sample are described in Table 2.1. Continuum images of the fields are indicated in Figure 2.1.

Motte et al. (2022) determines the evolutionary stage of the protoclusters, based on the 1.3 mm-to-3 mm flux ratio and the free-free emission at the frequency of the H41 α recombination line. According to their classification, three of the high-mass protoclusters we consider (G328.25, G337.92 and G338.93) are 'Young', and two (G008.67 and G351.77) are 'Intermediate'. No 'Evolved' protoclusters were available with additional ALMA CO-line observations, which thus limits our high-mass sample to 'Young' and 'Intermediate' protoclusters. It should be noted that these classifications describe the evolutionary stage of the protocluster, not of any individual YSO in these clusters.

Using the SiO (5-4) line, Towner et al. (2023) identified outflows in the ALMA-IMF sample, which were classified as either 'likely', 'possible', or 'complex or cluster'. SiO is often found to trace high-velocity jets, as the energetic shocks cause silicon to be released from dust grains (e.g. Bally, 2016; Towner et al., 2023). Low-level CO transitions instead trace the lower velocity outflow, which is less compact than the jets traced by SiO. Therefore we do not directly use the SiO outflow identifications in this project. Rather, they are used as visual



Figure 2.1: Overview of the high-mass protoclusters studied in this work. Shown are Spitzer three-color images, where red = 24 μ m, green = 8 μ m, and blue = 3.6 μ m. Overlaid are ATLASGAL 870 μ m contours, logarithmically spaced from 0.45 Jy beam $^{-1}$ to 140 Jy beam $^{-1}$ with a 19.2'' beam. The green and red contours outline the primary beam response of the ALMA 12 m array mosaics down to 15% at 3 mm and 1.3 mm, respectively. All images were taken from Motte et al. (2022). *TODO: find sharper versions of these images*

Source ⁽¹⁾	Coordinates ⁽¹⁾ [ICRS]	d ⁽²⁾ [kpc]	Stage ⁽³⁾	Line	Beam ⁽⁴⁾ [" x "]
G008.67	18:06:21.12 -21:37:16.7	3.4 ± 0.3	I	CO (2-1)	0.72×0.59
				CO (3-2)	4.9×2.7
G328.25	15:57:59.68 -53:58:00.2	2.5 ± 0.5	Y	CO (2-1)	0.62×0.47
				CO (3-2)	0.35×0.29
G337.92	16:41:10.62 -47:08:02.9	2.7 ± 0.7	Y	CO (2-1)	0.61×0.48
				CO (3-2)	0.50×0.47
G338.93	16:40:34.42 -45:41:40.6	3.9 ± 1.0	Y	CO (2-1)	0.56×0.51
				CO (3-2)	0.50×0.46
G351.77	17:26:42.62 -36:09:20.5	2.0 ± 0.7	I	CO (2-1)	0.89×0.67
				CO (3-2)	0.90×0.61

Table 2.1: Overview of the observations of the high-mass sources. 1) The names and central coordinates of the mosaics for the high-mass protoclusters considered in this project. 2) Distances to the sun from Csengeri et al. (2017) (G338.93, G008.67, and G328.25), and from Motte et al. (2022) (G351.77 and G337.92). 3) The evolutionary stages of the ALMA-IMF protoclusters, where Y = young and I = intermediate, taken from Motte et al. (2022), who refined it from Csengeri et al. (2017). 4) The values for the beam that are indicated in bold font are the limiting resolution, and any higher resolution observation is smoothed to this resolution in Chapter 3.

guidance to help confirm the presence and morphology of outflows detected in CO.

2.2 Low-mass protoclusters

For our low-mass sample, we selected seven fields in the ρ Ophiuchi molecular cloud, which is one of the most actively studied low-mass star-forming regions. In Figure 2.2, an image of the cloud is given. In this project, we adopt a distance of 140 ± 10 pc to the cluster (Bontemps et al., 2001). Star formation in the ρ Ophiuchus cloud was likely triggered by supernovae, ionization-fronts and winds from the Upper Scorpius OB association, which is located to the west of the Ophiuchus cloud (Preibisch & Zinnecker, 1999; Nutter et al., 2006; Wilking et al., 2008). The seven fields in our low-mass sample have been observed in CO (1-0) (2013.1.00187.S, PI: Schnee), CO (2-1) (2019.1.01792.S, PI:Mardones) and CO (3-2) (2018.1.01634.S, PI: Segura-Cox, for Oph 34, 2022.1.00236.S, PI: Artur de la Villarmois for all other fields). The observational details of the low-mass sample can be found in Table 2.2. Values for the systematic velocity V_{LSR} were taken from Van der Marel et al. (2013) when available, and were otherwise defined in this paper using the peak of the CO transitions.

For the low-mass sources, no systematic outflow identifications using SiO are available. However, ρ Ophiuchi is a well-studied molecular cloud, which allows for comparison to literature in outflow identifications. The majority of the low-mass



Figure 2.2: NIRCam image of the ρ Ophiuchi cloud complex, made by the James Webb Space Telescope. The image was taken in F187N = blue, F200W = Light Blue, F335W = Cyan, F444W = Yellow, F470N = Red. Image taken from Pontoppidan (2023). **TODO: find a different image that shows individual sources.**

YSOs in this sample have been classified by Van Kempen et al. (2009) as either Stage 1, Stage 2, or as the transition phase Stage 1(T), based on the classification scheme by (Whitney et al., 2003; Robitaille et al., 2006). The majority of sources in our low-mass sample are Stage 1 embedded YSOs.

Source ⁽¹⁾	Coordinates ⁽¹⁾ [ICRS]	Stage ⁽²⁾	Transition	Beam ⁽³⁾ ["x"]
Oph 12	16:26:44.100 -24:34:48.000	1	CO (1-0)	3.5 x 1.8
			CO (2-1)	1.2 x 0.9
			CO (3-2)	4.5 x 2.6
Oph 26	16:27:26.900 -24:40:50.000	1	CO (1-0)	3.5 x 1.9
			CO (2-1)	1.2 x 0.9
			CO (3-2)	4.6 x 2.6
Oph 27	16:27:27.900 -24:39:33.000	1	CO (1-0)	3.5 x 1.9
			CO (2-1)	1.2 x 0.9
			CO (3-2)	4.6 x 2.6
Oph 29	16:27:30.100 -24:27:43.000	1	CO (1-0)	3.5 x 1.9
			CO (2-1)	1.2 x 0.9
			CO (3-2)	4.6 x 2.6
Oph 31	16:27:39.900 -24:43:13.200	2	CO (1-0)	3.4 x 1.8
			CO (2-1)	1.2 x 0.9
			CO (3-2)	4.6 x 2.6
Oph 34	16:31:35.600 -24:01:29.000	1(T)	CO (1-0)	3.4 x 1.9
			CO (2-1)	1.2 x 0.9
			CO (3-2)	0.7 x 0.6
Oph 39	16:32:00.900 -24:56:42.000	-	CO (1-0)	3.4 x 1.9
			CO (2-1)	1.2 x 1.0
			CO (3-2)	4.6 x 2.6

Table 2.2: Overview of the observations of the low-mass sources. (1) The names and central coordinates of the mosaics for the high-mass protoclusters considered in this project. (2) Evolutionary stages as defined in Van Kempen et al. (2009) when available, where 1 indicates a stage 1 embedded YSO, 2 indicates a stage 2 disk, and 1(T) is a source in transition from a stage 1 embedded YSO to a stage 2 disk. (3) The values for the beam that are indicated in bold font are the limiting resolution, in Chapter 3 lower resolution observations are smoothed to this resolution.

3. Rotational temperatures and CO column densities

I think some introductory text, here or before, is needed to introduce why you are doing what you are doing e.g. why are you getting the T_{rot} and column density? In other words somewhere (maybe just after the title of Methodology? you need to introduce/summarize what you do and why

3.1 Methodology

3.1.1 Inspecting the datacubes

We download the continuum-subtracted primary beam corrected data cubes that were introduced in Chapter 2, and visually inspect the data quality. All observations were re-framed to the rest-frequency of their respective lines, using the *imreframe* function in *casa*, to ensure that the transition coincides with the systematic velocity of each source. This property allows us to describe all spectral lines in terms of the relative velocity, rather than in terms of frequency or wavelength.

3.1.2 Smoothing and regridding

We aim to create maps of T_{rot} and $N_{tot}(CO)$ for each field in our high- and low-mass sample, which requires observations with consistent beams between different transitions. For each field, we smoothed all high-resolution observations to the lowest resolution available for that source, using the *imsmooth* function in *casa*. This function requires parameters for the input image, the major and minor axis of the beam, and the position angle of the beam. It uses Fourier-based convolution to smooth the image to the required beam. The limiting resolutions, to which the higher-resolution images were smoothed, are indicated in bold in Table 2.1 and Table 2.2. As a result of this smoothing, the flux density per beam increases, as the beam becomes larger. An example of the smoothing process is indicated in Figure 3.1, for the high-mass field G008.67.

As a final calibration step, all fields that were smoothed to a lower resolution were re-gridded to the same pixel grid as the field it was smoothed to. This step is required to be able to compare pixels to each other. The regridding was allowed since all images were well-sampled. We used the *reproject* python package (Deil & Ginsburg, 2024) to perform the regridding.

3.1.3 Integrated emission maps

Through visual inspection of the high- and low-mass data cubes, we defined the velocity ranges in which the red- and blue-shifted lobes are detected. Channels near the systemic velocity v_{LSR} were excluded, as here the envelope emission

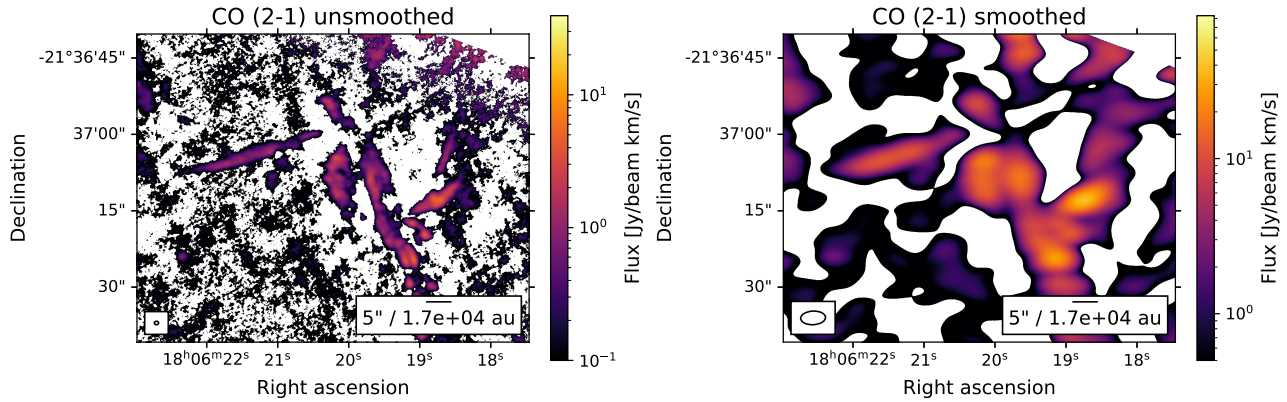


Figure 3.1: CO (2-1) red-shifted integrated emission of the high-mass source G008.67, before and after smoothing to the resolution of the CO (3-2) maps. The maps were both integrated over the same velocity range, as indicated in Table 3.1. This image merely serves as an example of the smoothing process, therefore the clipping was done at arbitrary values.

dominates over the outflows. If multiple outflows were detected in a single field, we extended the velocity ranges to that of the outflow with the broadest velocity range. The chosen velocity ranges can be found in Table 3.1. Using these velocity ranges, red- and blue-shifted velocity-integrated maps were constructed of all observations.

3.1.4 Determination of noise levels and clipping

The noise levels of each velocity-integrated emission map were determined by selecting a region without a source in it. Then, the root mean square (rms) was taken over all pixels in this 'empty' region. This number was then convolved with a percentage of the emission, to obtain the noise level σ per pixel. The percentage of the integrated emission that was used is 5% for the CO (1-0) line, and 10% for the CO (2-1) and CO (3-2) line, in line with ALMA systematic uncertainties (Braatz et al., 2021). We then define the signal-to-noise ratio (SNR) to be the integrated emission divided by σ for each pixel.

Only pixels with a 3σ detection in two transitions (CO (2-1) and CO (3-2)) for the high-mass sample, or in three transitions (CO (1-0), CO (2-1), and CO (3-2)) for the low-mass sample are included in further calculations. Since emission near the systematic velocity was not included, most of the 3σ emission that is included will be part of an outflow. In this chapter, we make no attempt to identify the outflows. We use a different selection limit for the high- and low-mass samples, since we require that pixels are detected in two transitions for the high-mass sample, and in three transitions for the low-mass sample. Outflow identifications at this stage would therefore introduce an unwanted bias between the high- and low-mass samples. Outflow identifications will be made in Chapter 4 using unsmoothed CO (2-1) observations, which are more reliable for this purpose.

Source	$v_{LSR}^{(1)}$ [km s ⁻¹]	$v_{red,min}^{(2)}$ [km s ⁻¹]	$v_{red,max}^{(2)}$ [km s ⁻¹]	$V_{blue,min}^{(2)}$ [km s ⁻¹]	$V_{blue,max}^{(2)}$ [km s ⁻¹]
Oph 12	4.3 ^(a)	5.1	10.5	-3.2	1.9
Oph 26	3.8 ^(a)	4.3	11.8	-6.3	1.9
Oph 27	3.8 ^(a)	5.9	11.0	-10.0	1.0
Oph 29	4.5 ^(a)	5.0	8.0	-6.0	1.3
Oph 31	2.7 ^(b)	4.5	9.0	-1.0	1.0
Oph 34	2.7 ^(a)	3.0	7.0	-9.0	0.9
Oph 39	3.0 ^(b)	4.5	11.0	-5.0	2.4
G008.67	37.6 ^(c)	48	82	-20	26
G328.25	-43 ^(c)	-35	35	-115	53
G337.92	-40 ^(c)	-31	23	-105	-50
G338.93	-62 ^(c)	-55	0	-130	-73
G351.77	-3 ^(c)	20	90	-120	-13

Table 3.1: The velocity ranges over which the CO emission was integrated to create the integrated blue- and red-shifted CO emission maps, which were used to create maps of T_{rot} and N_{tot} . In this chapter, we do not identify individual outflows, instead we calculate T_{rot} and N_{tot} for the entire field. (2) Values for the systematic velocity v_{LSR} , where (a)=Van der Marel et al. (2013), (b)=this project, (c)=Wienen et al. (2015). (4) The upper and lower velocity limit over the CO emission was integrated. The spectral resolution for the low-mass sources is 0.08 km s⁻¹, and for the high-mass sources 1.3 km s⁻¹.

3.1.5 Local thermodynamic equilibrium

If the interstellar medium (ISM) is in thermodynamic equilibrium (TE), its macroscopic properties such as temperature T and density n are uniform and do not change over time. These conditions imply there are no flows of energy, and any chemical reaction is in equilibrium. TE does not generally hold, as we observe a wide range of temperatures and densities in the ISM. A weaker condition is local thermodynamic equilibrium (LTE), in which macroscopic energy flows do exist, but temperature and density vary slowly enough for particles to behave as if they are in TE on small scales.

The velocities v of particles in LTE follow a Maxwell distribution

$$f(v) = \sqrt{\frac{2}{3}} \left(\frac{m}{kT}\right)^3 v^2 e^{-mv^2/kT}, \quad (3.1)$$

where m is the particle mass and k is the Boltzmann constant.

The population of energy levels in LTE can be described by a Boltzmann distribution

$$\frac{n_u}{n_l} = \frac{g_u}{g_l} e^{-(E_u - E_l)/kT}, \quad (3.2)$$

where n_u and n_l are the densities in the upper and lower level, respectively, g_u

and g_u and g_l are the degeneracies of the upper and lower levels, and E_u and E_l are the energies of the upper and lower levels.

In LTE, the radiation field follows the Planck function

$$B_\nu(T) = \frac{2h\nu^3}{c^2} \frac{1}{e^{\frac{h\nu}{kT}} - 1}, \quad (3.3)$$

also referred to as the blackbody function. Here, ν is the frequency, h is the Planck constant and c is the speed of light.

LTE does not generally hold in the ISM, due to the low densities and consequent low collision rates, however Equations 3.1 through 3.3 might still hold under certain conditions. The Maxwell distribution holds outside of LTE if the density is high enough to cause frequent collisions. In this case, we describe the Maxwell distribution by the kinetic temperature T_{kin} .

The Boltzmann distribution is not generally valid outside of LTE, however, we can still use the Boltzmann distribution to describe the population levels between any two levels using Equation 3.2, by replacing T with the excitation temperature T_{ex} . T_{ex} is not a physical temperature, it merely represents the ratio of level populations. In LTE, we then retrieve $T_{kin} = T_{ex} = T$.

The Planck function does not generally hold in the ISM either, due to discrete energy sources (e.g. stars), absorption, and emission processes. We can define the brightness temperature T_b as the temperature a blackbody radiator would need to have to reproduce the observed intensity of the region, at a specific frequency.

3.1.6 Radiative transfer

As light travels through the ISM, light can be absorbed or emitted through interactions with the ISM, which can change the observed specific intensity I_ν . In LTE, if the excitation properties remain constant along the line of sight, we can describe I_ν as

$$I_\nu = I_\nu(0)e^{-\tau_\nu} + B_\nu(T_{ex})(1 - e^{-\tau_\nu}), \quad (3.4)$$

where $I_\nu(0)$ is the initial specific intensity of the source, which gets attenuated as the light traverses the interstellar medium. This attenuation is governed by the optical depth τ_ν , which is frequency-dependent. As the light traverses from its original source, it gets thermalized with the ISM, until at sufficient optical depth the light is fully described as $B_\nu(T_{ex})$, a blackbody at T_{ex} of the ISM. It should be noted that T_{ex} is frequency dependent. All spectral line dependence is encoded in T_{ex} .

Generally, we state that the ISM is optically thin at a specific frequency ν , if $\tau_\nu \ll 1$, in which case we can write

$$I_\nu \approx I_\nu(0) + e^{-\tau_\nu} \tau_\nu B_\nu(T_{ex}). \quad (3.5)$$

If $\tau_\nu \gg 1$, we state the ISM is optically thick and thus opaque. Any background radiation is now fully thermalized, and we can only see the outer layers of the cloud.

3.1.7 Rotation diagram method

For a given species, if we detect enough transitions with a wide range of upper-level energies E_u , a rotation diagram (RD) can be constructed. The RD allows us to derive the rotational temperature T_{rot} , which is a proxy for the kinetic temperature T_{kin} of the gas, and the column density N_{tot} of the species (e.g. Turner, 1991; Sutton et al., 1995). The RD assumes that all transitions are optically thin ($\tau < 1$), and a single excitation temperature T_{ex} characterizes all transitions (i.e. the observed object is in LTE). If the system is not in LTE, T_{ex} is not a good proxy for T_{kin} .

In this project, we are allowed to assume that the size of the emission is larger than the size of the beam of the observation, as we study well-resolved protostellar outflows. Therefore, we do not need to correct for beam dilution.

For a single transition, the column density of molecules in the upper energy level, N_u^{thin} , can be derived using the following equation for optically thin lines:

$$N_u^{thin} = \frac{4\pi \int F_\nu dV}{A_{ji}\Omega hc}. \quad (3.6)$$

In this equation, $\int F_\nu dV$ is the velocity-integrated specific flux density, ν is the frequency of the transition, A_{ji} is the Einstein coefficient of the transition, Ω is the size of the beam, h is the Planck constant, and c is the speed of light.

In LTE, the total column density relates to the upper-level column density as

$$\frac{N_u^{thin}}{g_u} = \frac{N_{tot}}{Q(T_{kin})} e^{-E_u/kT_{kin}}, \quad (3.7)$$

where g_u denotes the upper-level degeneracy, $Q(T_{kin})$ is the partition function at T_{kin} , E_u is the upper-state energy, and k is the Boltzmann constant. Taking the natural logarithm of both sides of Equation 3.7 gives

$$\ln\left(\frac{N_u^{thin}}{g_u}\right) = \left(\frac{-1}{T_{kin}}\right)\left(\frac{E_u}{k}\right) + \ln\left(\frac{N_{tot}}{Q(T_{kin})}\right). \quad (3.8)$$

This equation allows us to derive T_{rot} and N_{tot} . By plotting $\ln\left(\frac{N_u^{thin}}{g_u}\right)$ against $(\frac{E_u}{k})$ and fitting a line ($y = a \cdot x + b$), the slope $a = \frac{-1}{T_{rot}}$, and the intercept $b = \ln\left(\frac{N_{tot}}{Q(T_{rot})}\right)$. The latter gives N_{tot} by interpolating Q at T_{rot} , which was derived from the slope, using values for $Q(T)$ found in molecular databases such as the CDMS (Müller et al., 2001, 2005; Endres et al., 2016). An example of a rotational diagram is shown in Figure 3.2.

The RD method requires a minimum of two observed transitions, although it is preferable to perform the analysis on more than two transitions. If the assumption that all lines are optically thin fails, if the observed object is not in LTE, or if it consists of multiple gas components with different temperatures, a well-sampled rotational diagram will not show a straight line. When only observing two transitions, this nonlinearity cannot be detected, and one cannot determine

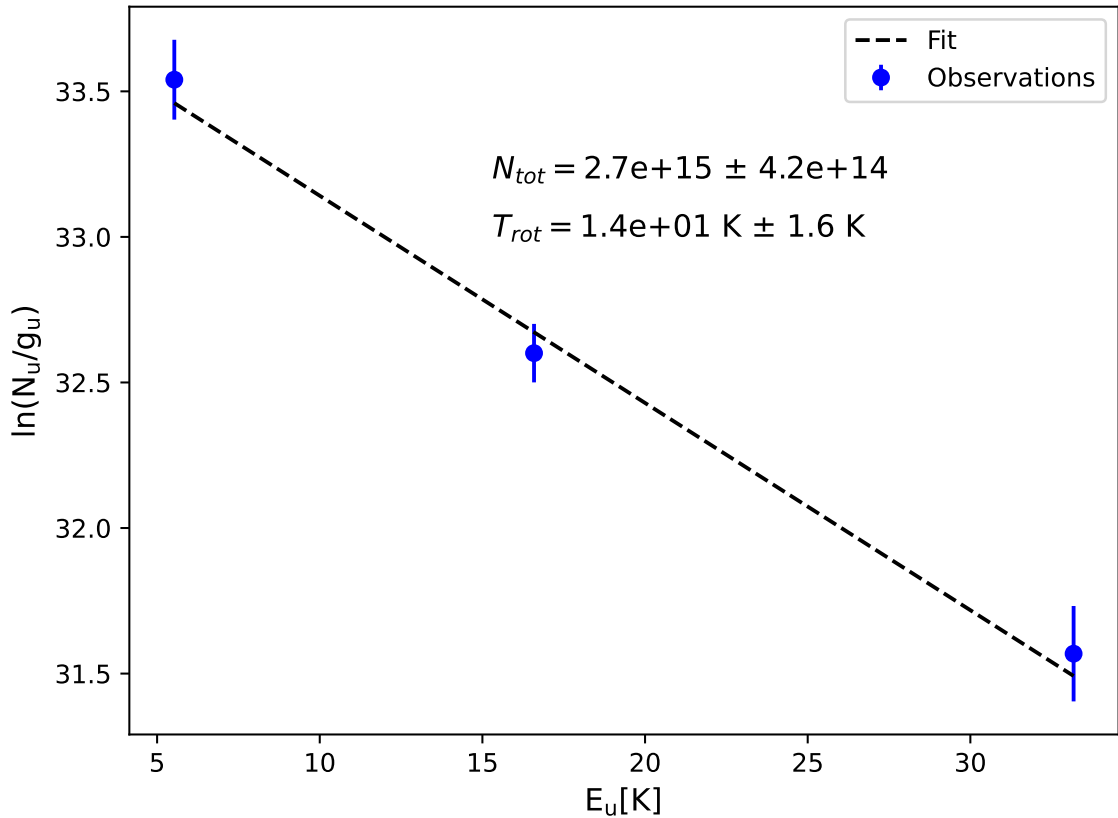


Figure 3.2: Example of a rotational diagram of CO, for a pixel in the blue-shifted lobe of Oph 12, close to the YSO. The derived values for T_{rot} and N_{tot} are indicated.

when the underlying assumptions fail. The RD method should be used with care, and methods that do not assume LTE or optically thin transitions will be more reliable if enough transitions are detected. An example of such a method is modeling the gas using a non-LTE radiative transfer code, such as RADEX. This method does not assume LTE and is able to constrain optically thick transitions. However, collisional coefficients of the species would need to be available in order to perform such an analysis.

3.1.8 T_{rot} and $N_{tot}(\text{CO})$ determination

For each 3σ pixel in our high- and low-mass fields, we determine the upper-level column density for all available transitions, using Equation 3.6. We then construct the RD for each pixel, using the upper-level energies retrieved from CDMS (Müller et al., 2001, 2005; Endres et al., 2016).

For our low-mass sample, we use least squares fitting to fit a line to the RD, and from the slope we immediately retrieve T_{rot} for each pixel. We interpolate Q to retrieve $Q(T_{rot})$, which allows us to determine $N_{tot}(\text{CO})$ from the intercept. Uncertainties were estimated from the covariance matrix. Any uncertainties in $Q(T_{rot})$ were neglected.

For our high-mass sample, the same method was used, although since there are only two detected transitions, uncertainties could not be estimated through the covariance matrix, and standard propagation of errors was used instead.

3.2 Results

As an example, the maps of T_{rot} and N_{rot} of G338.93 are indicated in Figure 3.3. For the remaining sources, the maps are indicated in Appendix A.2. In these maps, we indicate for the high-mass sources the continuum cores as traced by the DCN (3-2) transition (Cunningham et al., 2023), as well as the hot cores traced by CH₃OCHO (methyl formate, Bonfand et al., 2024). For the low-mass sample, we indicate the positions of sources in the Two Micron All Sky Survey (2MASS) Point Source Catalog (PSC, Skrutskie et al., 2006), that were identified as YSO in literature (Bontemps et al., 2001; Wilking et al., 2008; Pattle & Ward-Thompson, 2015; Connelley & Greene, 2010).

For each field, we determine the mean T_{rot} and $N_{tot}(\text{CO})$. We indicate these mean values below, however, care should be taken in interpreting these values as the temperature can vary significantly over a single field. We refer back to Appendix A.2 for a better overview of the ranges of values of T_{rot} and $N_{tot}(\text{CO})$ that were determined. In Section 3.2.1 and Section 3.2.2, we go into more depth about the ranges of temperatures that were found, and whether the underlying assumptions made for the RD method hold.

The mean rotational temperature over the low-mass fields ranges between 8.3 K and 21.8 K, with a weighted mean of 11.3 ± 0.6 K. For our high-mass sample, we find the mean temperature per field to range between 22.6 K and 58.9 K, with a weighted mean of 28 ± 6 K. If all assumptions of the RD method hold, we would find that high-mass protostellar outflows have higher rotational temperatures compared to low-mass protostellar outflows.

The mean CO column density over the low-mass fields ranges between $8 \cdot 10^{14} \text{ cm}^{-2}$ and $1.3 \cdot 10^{16} \text{ cm}^{-2}$, with a weighted mean of $2.0 \cdot 10^{15} \pm 0.2 \cdot 10^{15} \text{ cm}^{-2}$. The mean column density over the high-mass fields ranges between $6.3 \cdot 10^{15} \text{ cm}^{-2}$ and $2.6 \cdot 10^{17} \text{ cm}^{-2}$, with a weighted mean of $9.0 \cdot 10^{15} \pm 0.6 \cdot 10^{15} \text{ cm}^{-2}$. Therefore under RD assumptions, we find that low-mass protostellar outflows have lower CO column densities compared to high-mass protostellar outflows.

3.2.1 Optically thick transitions in high-mass fields

Since our high-mass sample is only detected in two transitions, it is important to determine whether our initial assumptions hold. Therefore, we determine for all fields whether T_{rot} is well-behaved. We find that multiple pixels return a negative value for T_{rot} , which is a clear indicator that the CO (2 – 1) line is optically thick in those pixels, and the RD method fails. Any of these pixels are masked out. Furthermore, there are many pixels with $T_{rot} >> 200\text{K}$, even upwards of $\sim 10^4\text{K}$, while a generous estimate for the maximum expected T_{rot} would be $\sim 100\text{K}$ (McKee & Tan, 2003). These extreme values further indicate that for many pixels,

the CO (2-1) line is optically thick and T_{rot} is overestimated. We thus mask out any pixel with $T_{rot} > 200\text{K}$, and do consider either T_{rot} or $N_{tot}(\text{CO})$ to be valid for this pixel.

Even when masking out these unrealistic values, we cannot determine whether pixels with ‘well-behaved’ temperatures are reliable, or if they are affected by optical thickness or non-LTE circumstances as well. Therefore, we assume all values for temperature estimates in the high-mass fields are upper limits. As a consequence, column densities are likely underestimated, therefore we treat them as lower limits.

For G328.25 and G338.93, many pixels in the middle of outflows are masked out due to negative or extreme values of T_{rot} , while for the other high-mass sources (G008.67, G337.92, and G351.77), the masked out pixels are either near the YSO or on the furthest parts of the outflows, and in total, fewer pixels are masked out. We therefore suspect that for the latter sources the problem is less significant, and the derived values are more reliable than the former sources. In Figure 3.3 multiple masked-out regions can be seen in the red-shifted lobe.

We attempted to constrain the temperatures and column densities of the high-mass fields more accurately by using the non-LTE modeling software *RADEX*, but we were unable to constrain a reliable fit, due to the limited amount of transitions available. More details on this process can be found in Appendix A.1.

3.2.2 Non-LTE or multiple component emission in low-mass fields

For the low-mass sources three transitions are detected, so optically thick transitions are more easily flagged. We find no pixels with negative temperatures, or temperatures higher than $\sim 50\text{ K}$. Furthermore, for each pixel the CO (1-0) transition lays at higher $\ln\left(\frac{N_{tot}(\text{CO})}{Q(T_{kin})}\right)$ than the CO (2-1) transition in the RD. Therefore, we assume that the low-mass fields are not generally affected by optically thick transitions.

The only pixel in all of the low-mass fields that is deemed unreliable is a pixel in the red-shifted maps of Oph 27. The RD of this pixel shows the CO (1-0) transitions to be lower than the CO (2-1) transition, indicating that the pixel is optically thick in the former transition. Van der Marel et al. (2013) find that this is the only source in their sample to be optically thick as well, further away from the source velocity. Their findings are based on the CO (3-2) and ^{18}CO (3-2) transitions. They find that these optically thick regions only occur in the blue-shifted lobes, while the optically thick pixel we identify is in the red-shifted lobe. Therefore, the derived T_{rot} and $N_{tot}(\text{CO})$ values for Oph 27 should be interpreted carefully.

Since we only detect a single pixel that is visibly optically thick in the CO (1-0) transition, and the RD is well-sampled for the low-mass sample, we do not consider the temperatures to be upper limits and column densities to be lower limits. There could be pixels in this field or another low-mass field with optically thick transitions that we do not identify, however, any overestimation of the rotational temperature will be mitigated by the other transitions that are available.

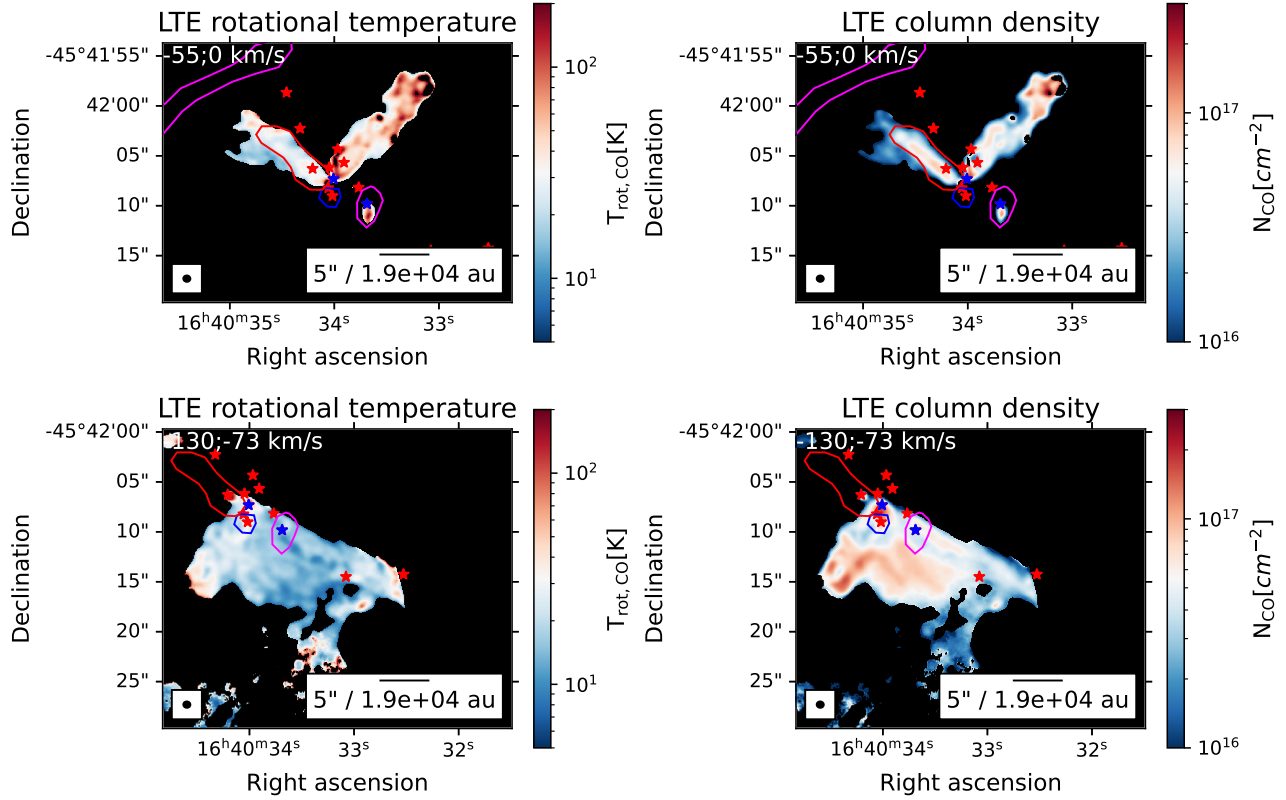


Figure 3.3: T_{rot} and $N_{\text{tot}}(\text{CO})$ maps for G338.93. The upper plots indicate the red-shifted lobes, integrated between -55 and 0 km s^{-1} . The lower plots indicate the blue-shifted lobes, integrated between -130 and -73 km s^{-1} . The beam size is indicated in the bottom left of each figure, a scale bar is indicated in the bottom right of each figure. SiO-identified outflows are indicated in red and blue for red-shifted and blue-shifted outflows, bipolar SiO-identified outflows are indicated in pink (Towner et al., 2023). Hot cores (Bonfand et al., 2024) are indicated as blue stars, while continuum cores (Cunningham et al., 2023) are indicated as red stars. In one of the red-shifted lobes, pixels are masked out, due to T_{rot} being either negative or extremely high. We suspect that the majority of pixels is optically thick in the CO (2-1) line, therefore we treat derived temperatures as upper limits and derived column densities as lower limits. *To do: Circle the masked-out regions, and consider if the figure might be too small*

Therefore we suspect that the estimated rotational temperatures are reliable, and we do not classify them as upper-limits.

We manually inspect the RD for certain pixels close to and far from the YSO, to ensure that the RD method is reliable for these fields. We find that there is a slight deviation in the RD for a minority of the pixels, across various sources. An example can be found in Figure 3.4. Such a deviation in the RD could be explained by the sources not being in LTE. Another explanation might be that there are multiple regions with different temperatures in the same beam. Therefore, the low-mass temperature and column density maps should be interpreted with care as well.

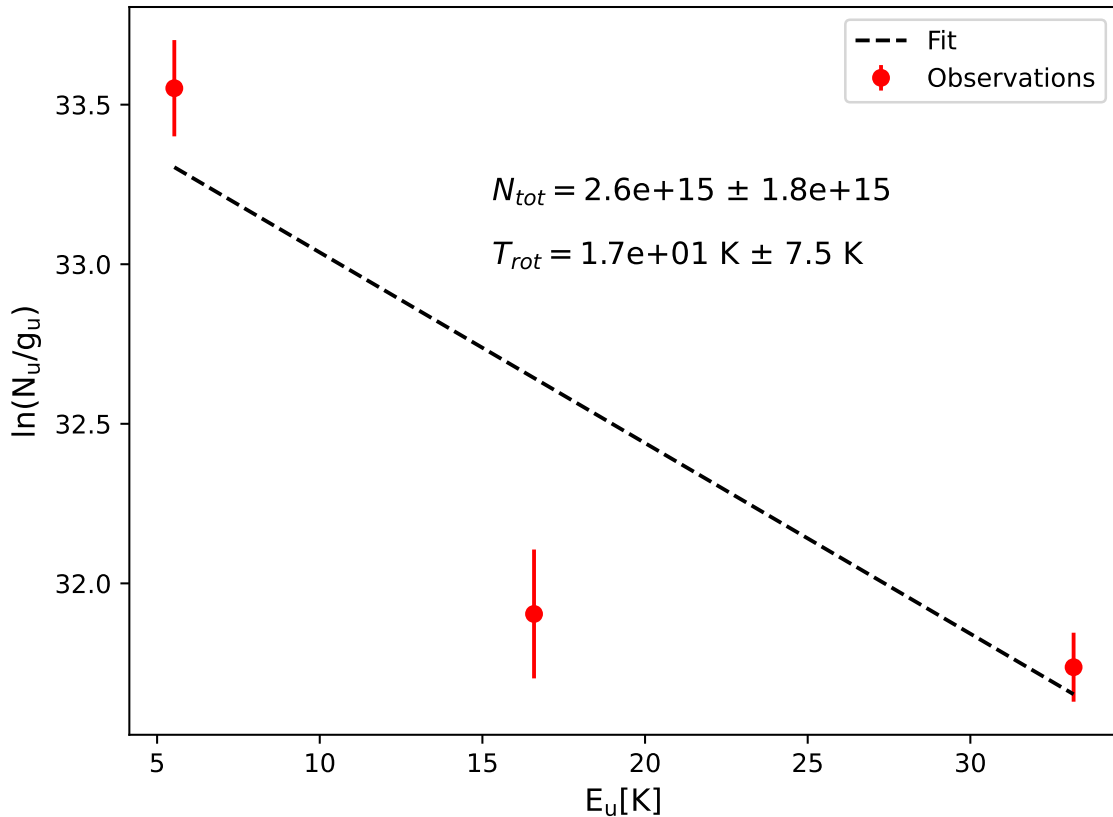


Figure 3.4: Example of the RD of a pixel in the red-shifted lobe in Oph 12. This RD displays a deviation, either caused by the gas not being in LTE, or there being multiple emitting regions with different temperatures in the same beam. The derived values for T_{rot} and $N_{tot}(\text{CO})$ are indicated.

4 . Morphology and outflow properties

same comment as at the beginning of chapter 3

4.1 Methodology

4.1.1 Integrated CO (2-1) maps

To determine the morphological parameters of the outflows in our samples, we construct integrated blue- and red-shifted CO (2-1) maps. This transition is the lowest upper-level energy that is detected for both samples. Since we will inspect the morphology of the sources using only the CO (2-1) line, no smoothing was done on these maps. The resolution of the maps can be found in Table 2.1 and Table 2.2. The maps were integrated over the same velocity ranges as were used in Chapter 3, which are indicated in Table 3.1. The maps can be found in Figure 4.3, Figure 4.4, and Figure 4.5. An in-depth description of each field can be found in Section 4.2.3.

4.1.2 Outflow classifications

From the CO (2-1) maps, we identify red-shifted and blue-shifted outflows by eye, which we then classify as either ‘Likely’ or ‘Possible’. ‘Likely’ lobes are isolated, clearly connected to a YSO, with a red- or blue-shifted counterpart. For the high-mass sample, we also visually compare the CO outflows to outflow identifications using SiO (Towner et al., 2023), to further confirm outflow identifications. ‘Likely’ lobes are included in further calculations. ‘Possible’ lobes are lobes that might be overlapping with other lobes, or lobes that are disconnected from a protostar, and are not included in any further calculations in this chapter. For all ‘Likely’ lobes, we determine the outflow radius R , the outer velocity v_{out} , the dynamical age t_{dyn} , and the opening angle α .

4.1.3 Radius determination

We determine the radius of the 25 ‘Likely’ lobes, which we eventually use to determine the dynamical ages of the outflows. We identify the outflow axis originating from the central YSO, by following the brightest contours of the integrated CO (2-1) maps. We then select the furthest point on this axis where the integrated emission is still higher than 3σ . The length of this axis is then defined as the radius R of the outflow. The uncertainty on R was found by convolving the major axis of the beam with 10% of R .

Since R is determined by following the brightest parts of the lobe, the axis might not always extend to the furthest point of the lobe, for example, if there is a cavity in the outflow or if the lobe is severely asymmetric. Furthermore, the true value of R is inclination-dependent, which can usually not be determined accurately. For the purposes of this project, we can use R to compare the relative sizes between low- and high-mass sources, but care should be taken when interpreting it as a physical parameter.

If the position of the YSO aligns with the brightest part of the lobe, the direction of the axis can not be determined accurately. In such a case, the outflow axis was chosen to extend to the furthest point of the lobe.

Due to the intrinsic astrometric inaccuracy of 2MASS, the starting point of the radii for some low-mass sources was not always chosen as the exact location of the YSO, if the reported YSO position appears offset from the outflow axis. 2MASS has a positional accuracy of 0.5" (Skrutskie et al., 2006), therefore we ensure that the offset between the YSO and the new starting point of the axis is no larger than this value.

4.1.4 Outer velocity determination

We determine v_{out} for each lobe by determining the furthest velocity bin away from the systematic velocity v_{LSR} where there is still a 3σ detection. In the high-mass fields, multiple outflows are often present in a single field. For each red- and blue-shifted lobe, v_{out} was determined separately. We then find $\Delta v = |v_{out} - v_{LSR}|$, which we eventually use to determine the dynamical age t_{dyn} . The uncertainty in Δv is found by convolving the spectral resolution of the CO (2-1) observations (1.3 km s^{-1} for the high-mass fields, 0.08 km s^{-1} for the low-mass fields) with 5% of Δv .

In literature (e.g. Van der Marel et al., 2013), v_{out} is defined as the last velocity bin where the emission is still above 1σ . However, since we determine the outflow radii R using a 3σ limit, we decided to determine v_{out} using a 3σ limit as well.

v_{out} is usually not a well-constrained parameter, and it should be interpreted with care. It depends significantly on the inclination, which is often unknown. Furthermore, outflows often have multiple epochs of activity (e.g. Arce et al., 2007; Plunkett et al., 2015), often follow a bow-shock (e.g. Cabrit et al., 1997) which includes forward and transverse motion, and outflows can show features such as cavities. Therefore, the measured v_{out} along the line of sight is not necessarily representative of the real velocity of the outflow. In this project, we use v_{out} to compare our low- and high-mass sources and to determine t_{dyn} , however it should not be interpreted as a physical velocity.

4.1.5 Dynamical age determination

We determine the dynamical age from $t_{dyn,obs} = \frac{R}{\Delta v}$, which is not corrected for inclination. An outflow in the plane of the sky (roughly $i = 90^\circ$) will have an overestimated dynamical age, while a pole-on source (roughly $i = 0^\circ$) will have an underestimated dynamical age. The corrected dynamical age is $t_{dyn,true} = \frac{t_{dyn,obs}}{\tan(i)}$.

In Chapter 5, we compare both the uncorrected and corrected dynamical ages between the high- and low-mass samples.

The calculation for t_{dyn} ignores any episodic activity and depends on all the caveats in R and v_{out} that were mentioned above. Therefore, t_{dyn} is rarely a true tracer of the age of the outflow, and should not be interpreted as such. We can however use it to compare the relative timescale of dynamic activity between low- and high-mass protostellar outflows. Downes & Cabrit (2007) have developed a more accurate method to determine t_{dyn} , using the half-width of the outflow lobe, however this method can only be applied on spatially well-resolved outflows, and might not be applicable to Class I sources or high-mass sources, since this method was only tested on low-mass Class 0 sources.

4.1.6 Opening angle determination

We determine the outflow angle α of each ‘likely’ outflow in our sample, using the method described by Dunham et al. (2024), first developed by Offner et al. (2011).

For each outflow, we mask out any pixel of the integrated CO (2-1) maps below 3σ , and any pixel not part of the outflow. In some fields, we also mask out pixels that are part of the outflow, for example, if the outflow is significantly asymmetric due to low-SNR lobes. In Figure 4.1, the included pixels are indicated in the shaded blue and red regions.

For all remaining pixels, we determined the angle between that pixel and the axis used to determine the outflow radius. Unlike Dunham et al. (2024), we treat the red-shifted and blue-shifted outflow separately, since the red and blue axes can be significantly offset. We plot this angle distribution and use non-linear least-squares fitting to fit a Gaussian distribution to it.

In Figure 4.2, an example is given of a source where parts of the angle distribution were masked out before fitting the Gaussian distribution, as justified by Dunham et al. (2024). Since there is a cavity in the red-shifted lobe, only the wings of the distribution properly represent the opening angle, and the center of the distribution can be masked out.

The full width at quarter maximum (FWQM) of the Gaussian fit provides us with a measure for the opening angle, which is indicated in Figure 4.1 relative to the fitted axis. The method used to determine the opening angle is more systematic than determining the opening angles ‘by eye’, however it is not always a good representation of the ‘true’ opening angle, if such a parameter can even be defined. The opening angle is strongly dependent on inclination, which is not available for the majority of our sources. Therefore we are likely overestimating the opening angle of our sources. However a comparison between high- and low-mass outflows still remains valid, as i should be distributed randomly for all sources in our high- and low-mass sample.

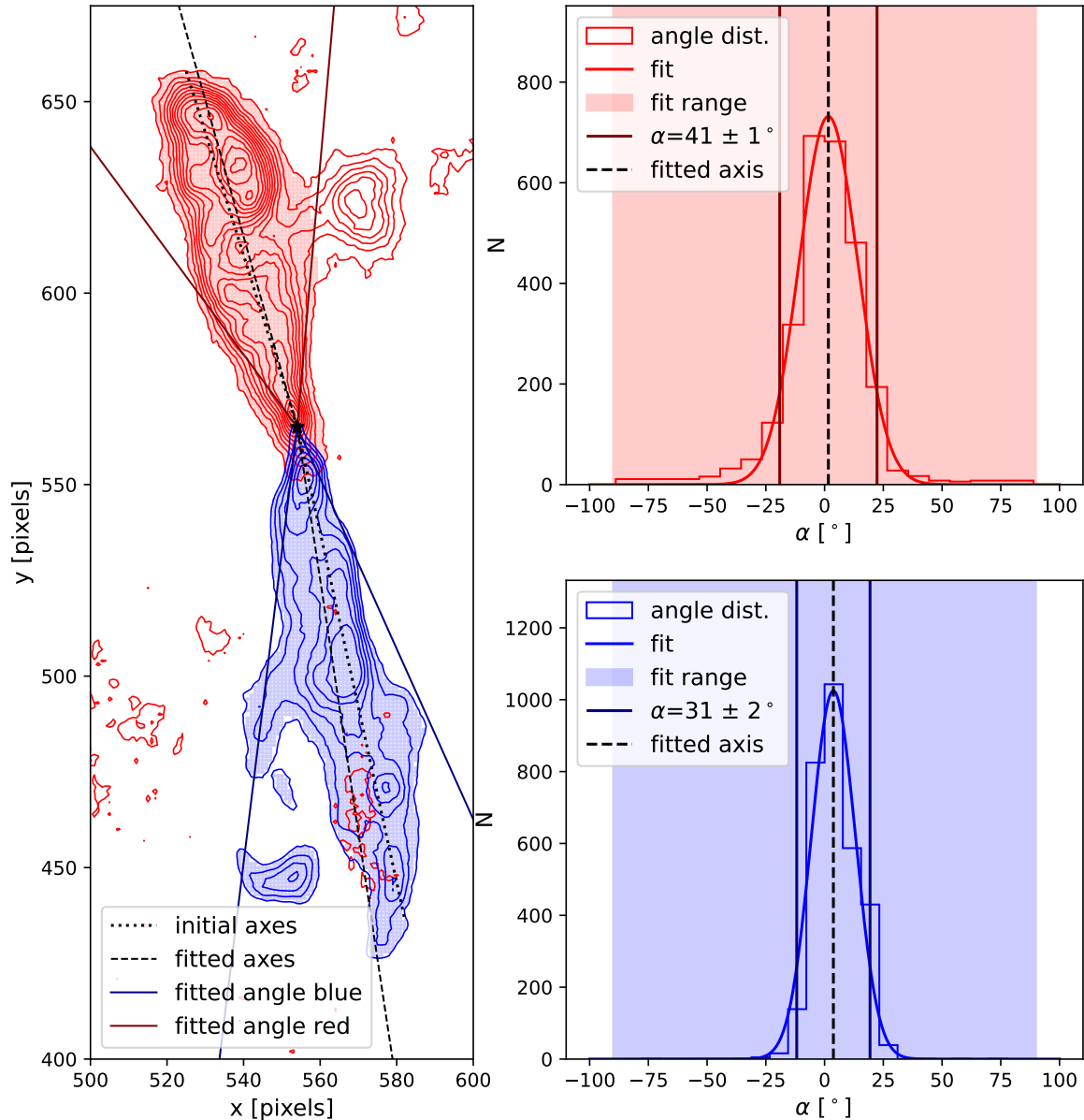


Figure 4.1: Left: Integrated blue- and red-shifted CO (2-1) emission showing the G328.25 outflow, integrated over the velocity interval reported in Table 3.1. The initial axes, indicated as dotted lines, are the axes used to determine the radii of the outflow. The pixels in the shaded areas are included in determining the opening angles. The fitted opening angles are indicated as solid lines, relative to the fitted axis indicated as a dashed line. The position of the YSO is indicated as a black star. Right: The histograms of the angle distributions used to determine the opening angles of the outflow, to which a Gaussian distribution is fitted. For this source, no angle distribution bins were excluded, which is indicated in the shaded region. The fitted axes are indicated as dashed lines, and the fitted opening angles are indicated as solid lines. *To do: improve the consistency in the colouring of the pixels, see if the axes can be in coordinates instead of pixels*

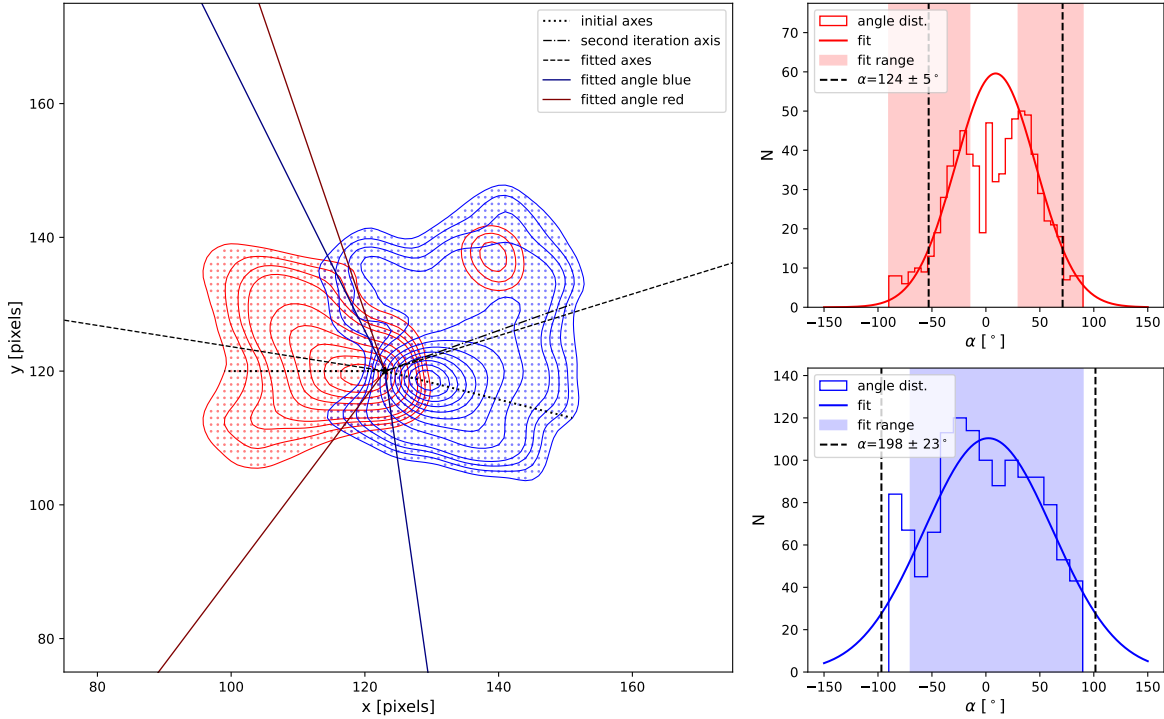


Figure 4.2: Left: Integrated blue- and red-shifted CO (2-1) emission showing the Oph 26 outflow, integrated over the velocity interval reported in Table 3.1. The initial axes, indicated as dotted lines, are the axes used to determine the radii of the outflow. The pixels in the shaded areas are included in determining the opening angles. The fitted opening angles are indicated as solid lines, relative to the fitted axis indicated as a dashed line. The position of the YSO is indicated as a black star. The red lobe is an example of a source where some bins in the angle distribution had to be masked out due to the presence of a cavity. For the red lobe, some bins had to be masked out due to the asymmetry of the source. Right: The histograms of the angle distributions used to determine the opening angles of the outflow, to which a Gaussian distribution is fitted. The shaded regions indicate which bins were included in the fitting. For this source, some bins in the red-shifted distribution are removed due to the cavity in the lobe. The fitted axes are indicated as dashed lines, and the fitted opening angles are indicated as solid lines.

4.2 Results

In Table 4.1, we summarize all parameters that were calculated in this chapter. We also indicate the inclination when available (Van der Marel et al., 2013). In Section 4.2.3, we justify for each source which outflows were identified and their classification, and any further source-specific detail about the determination of the outflow parameters.

Outflow ⁽¹⁾	$v_{\text{sys}}^{(2)}$ [km/s]	$i^{(3)}$ [°]	$R^{(4)}$ [$\times 10^4$ au]	$v_{\text{out}}^{(5)}$ [km/s]	Red			$C^{(7)}$	$\alpha^{(8)}$ [°]	$R^{(4)}$ [$\times 10^4$ au]	$v_{\text{out}}^{(5)}$ [km/s]	Blue		
					$t_{\text{dyn}}^{(6)}$ [$\times 10^2$ yr]	$C^{(7)}$	$\alpha^{(8)}$ [°]					$t_{\text{dyn}}^{(6)}$ [$\times 10^2$ yr]	$C^{(7)}$	$\alpha^{(8)}$ [°]
Oph 12	4.3 ^(a)	30	0.1 ± 0.02	11.4	6 ± 1	L	91 ± 7			0.09 ± 0.02	-2.7	6 ± 1	L	96 ± 9
Oph 26	3.8 ^(a)	10	0.06 ± 0.02	12.5	3 ± 1	L	124 ± 5			0.07 ± 0.02	-6.8	3.3 ± 0.8	L	198 ± 23
Oph 27	3.8 ^(a)	30	0.03 ± 0.02	13.3	1 ± 1	L	-			0.05 ± 0.02	-11.4	17 ± 0.6	L	167 ± 12
Oph 29	4.5 ^(a)	70	0.08 ± 0.02	7.6	13 ± 3	L	137 ± 15			-	-6.8	-	P	-
Oph 31	2.7 ^(b)	-	0.08 ± 0.02	9.0	6 ± 1	L	209 ± 14			-	-1.4	-	P	-
Oph 34	2.7 ^(a)	30	0.03 ± 0.02	5.1	6 ± 3	L	181 ± 21			0.08 ± 0.02	-9.2	3.3 ± 0.8	L	158 ± 7
Oph 39	3 ^(b)	-	0.04 ± 0.02	10.9	2 ± 1	L	123 ± 10			0.1 ± 0.02	-4.8	6 ± 1	L	86 ± 5
G008.67 _A	37.6 ^(c)	-	3.3 ± 0.4	76.5	40 ± 6	L	35 ± 12			5.0 ± 0.6	-26.4	37 ± 5	L	25 ± 2
G008.67 _B			1.9 ± 0.4	74.0	25 ± 6	L	39 ± 4			5.0 ± 0.6	-16.2	44 ± 6	L	57 ± 4
G008.67 _C			-	56.2	-	P	-			-	15.5	-	P	-
G008.67 _D			-	52.4	-	P	-			-	15.5	-	P	-
G328.25	-43 ^(c)	-	2.7 ± 0.3	26.4	18 ± 2	L	41 ± 1			3.5 ± 0.4	-117.1	22 ± 3	L	31 ± 2
G337.92	-40 ^(c)	-	4.3 ± 0.50	43.6	25 ± 3	L	50 ± 3			4.4 ± 0.5	-126.6	24 ± 3	L	61 ± 3
G338.93 _A	-62 ^(c)	-	4.4 ± 0.50	-11.4	41 ± 5	L	43 ± 3			-	-111.7	-	P	-
G338.93 _B			5.6 ± 0.6	28.0	29 ± 4	L	33 ± 1			-	-125.7	-	P	-
G338.93 _C			0.5 ± 0.3	-26.6	7 ± 4	L	-			-	-	-	P	-
G351.77 _A	-3 ^(c)	-	3.3 ± 0.40	126.1	12 ± 2	L	44 ± 4			-	-196.5	-	P	-
G351.77 _B			1.6 ± 0.3	102.0	7 ± 1	L	55 ± 4			-	-60.6	-	P	-

Table 4.1: The morphological parameters for all outflows in this project. (1) The name of the outflow. (2) The V_{LSR} values, where (a)=Van der Marel et al. (2013), (b)=this project, (c)=Wienen et al. (2015). (3) Outflow inclinations where available, from Van der Marel et al. (2013). (4) The outflow radii R , as described in Section 4.1.3, in units of 10^4 au. (5) The outer velocities v_{out} , as described in Section 4.1.4. (6) The dynamical ages t_{dyn} , uncorrected for inclination, as described in section 4.1.5. (7) The confidence in the outflow identification, where L = likely, P = possible. Only sources with the identification likely are included in the morphology calculations. (8) Opening angles α , as described in Section 4.1.6, uncorrected for inclination. Angles that could not be fit reliably are not indicated.

4.2.1 Radii, velocities, and dynamical timescales

The radii of the lobes in the low-mass sample are in a range between $3 \cdot 10^2$ au and 10^3 au, with a weighted mean value of $6.5 \cdot 10^2 \pm 5 \cdot 10^1$ au. The high-mass sample has a range of radii between $5 \cdot 10^3$ au and $5.5 \cdot 10^4$ au, with a weighted mean of $2.7 \cdot 10^4 \pm 1 \cdot 10^3$ au. The high-mass outflows are thus roughly a factor ~ 50 larger than the low-mass outflows.

The range of values we find for Δv in our low-mass sample is between 2.4 and 15.2 km s^{-1} , with a weighted mean of $4.9 \pm 0.1 \text{ km s}^{-1}$. For our high-mass sample, we find values of Δv between 35 and 129 km s^{-1} , with a weighted mean of $55 \pm 1 \text{ km s}^{-1}$. Therefore, we find that the high-mass sample has typical velocities ~ 10 times larger than the low-mass velocities.

We find dynamical timescales, uncorrected for inclination, in a range of $1.3 \cdot 10^2$ and $1.3 \cdot 10^3$ yr for the low-mass sample, with a weighted mean of $3.2 \cdot 10^2 \pm$

$0.2 \cdot 10^2$ yr. The high-mass sample has dynamical timescales in the range of $6.8 \cdot 10^2$ yr and $4.4 \cdot 10^3$ yr, with a weighted mean of $1.57 \cdot 10^3 \pm 0.07 \cdot 10^3$ yr. The high-mass outflows thus have typical uncorrected dynamic timescales ~ 5 times longer than the low-mass outflows.

4.2.2 Opening angles

Two examples of the opening angle determination method can be found in Figure 4.1 and Figure 4.2. For all other outflows in our high- and low-mass sample, we plot the determination of the opening angle in Appendix A.3.

For the low-mass sample, we find an average opening angle of $119 \pm 2^\circ$, while for the high-mass sample, we find an average opening angle of $38.5 \pm 0.6^\circ$. The low-mass outflows are thus much less collimated than the high-mass outflows.

We experienced a significant difference in the ‘ease of fitting’ between the high- and low-mass samples. The high-mass sources are generally more conical, and have smaller opening angles, so little manual masking had to be done on these sources. The low-mass sources are smaller and often have wider opening angles, which makes fitting the opening angle more difficult, and the method less reliable. Furthermore, there are often fewer pixels available to use for the fit of the low-mass sample, further complicating the determination of the opening angle for low-mass sources. In one case (the red-shifted lobe of Oph 27) no reliable fit could be achieved, therefore the value of α was not determined.

4.2.3 Details of individual outflows

In this section, we will describe for each field in our sample which outflows we were able to identify, their classification as either ‘Likely’ or ‘Possible’, and any comment on the determination of R , v_{out} , and t_{dyn} . We further comment on the determination of α and justify any masking done on the lobes and the angle distribution. Detailed figures of the opening angle determination can be found in appendix A.3 for each source.

Oph 12

The integrated blue- and red-shifted CO (2-1) maps of Oph 12 are indicated in Figure 4.3a. We identify a bipolar outflow along the northeast-southwest direction, which we label ‘Likely’. This outflow was also identified in Van der Marel et al. (2013), although they identified a northwest-southeast direction. This discrepancy in direction is likely because they observe a higher J-level (CO (3-2)) and at a lower resolution ($15''$). Therefore they might detect extended resolution that gets resolved out in our observations, while our data is sensitive to more compact emission, possibly influencing the direction and shape of the outflows that are identified.

Oph 12 has an inclination of 30° (estimated by Van der Marel et al. (2013)), which explains why the red and blue outflows overlap significantly. There is some unconnected blue emission, which was not included in the calculation of the opening angle. No other flux was masked out.

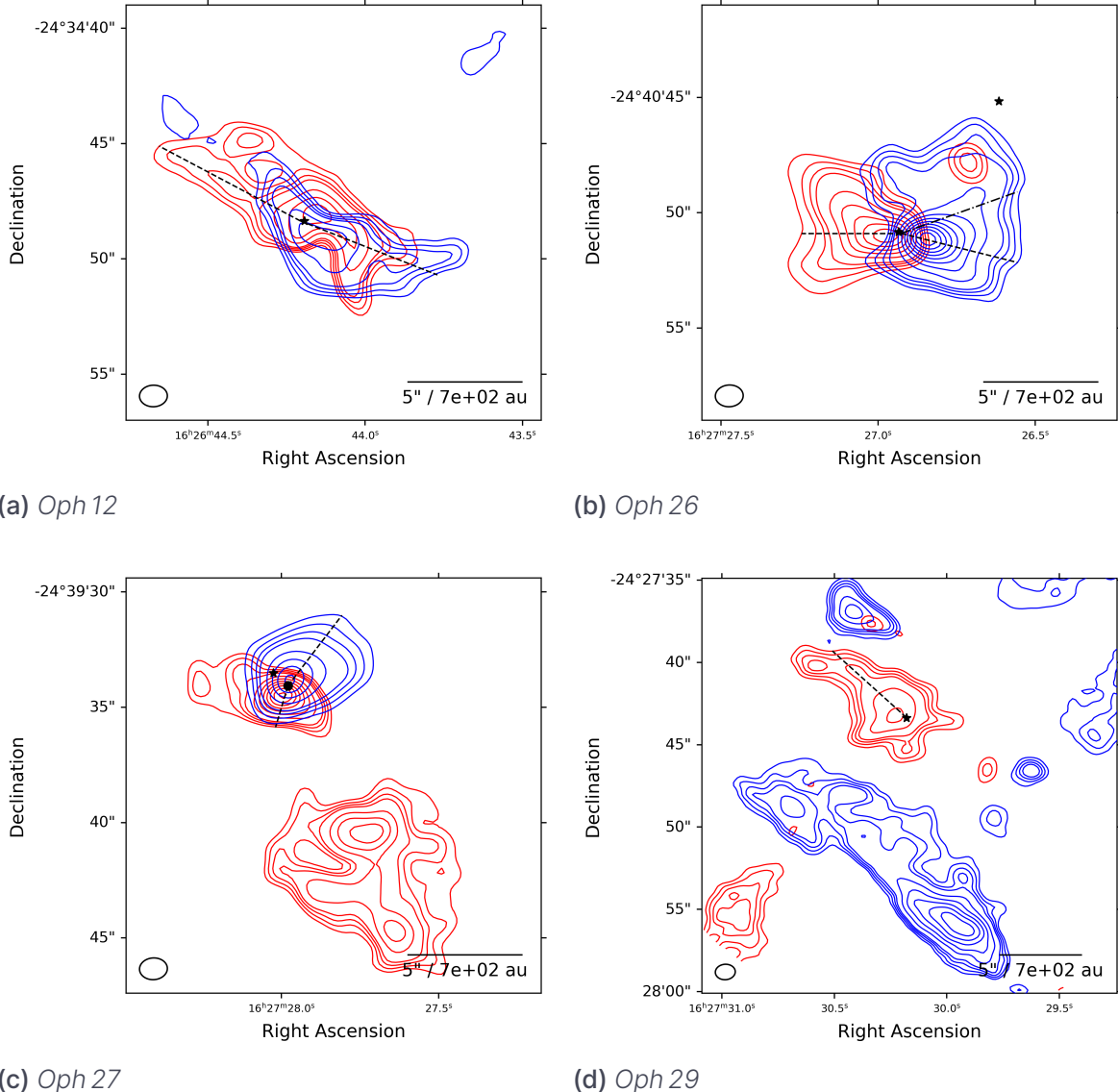


Figure 4.3: Integrated blue- and red-shifted CO (2-1) maps of sources in our low-mass sample. No smoothing was done on these maps. The velocity ranges used to create the maps are indicated in Table 3.1. The contour levels are at 3σ , 4σ , 5σ , 6σ , and then at intervals of 3σ . The positions of the YSOs are indicated as black stars, if the position of the outflow axis is manually altered from the position of the YSO, the new position is indicated as a black circle. Oph 26: The axis used for the second iteration of the angle determination is indicated as a dashed-dotted line.

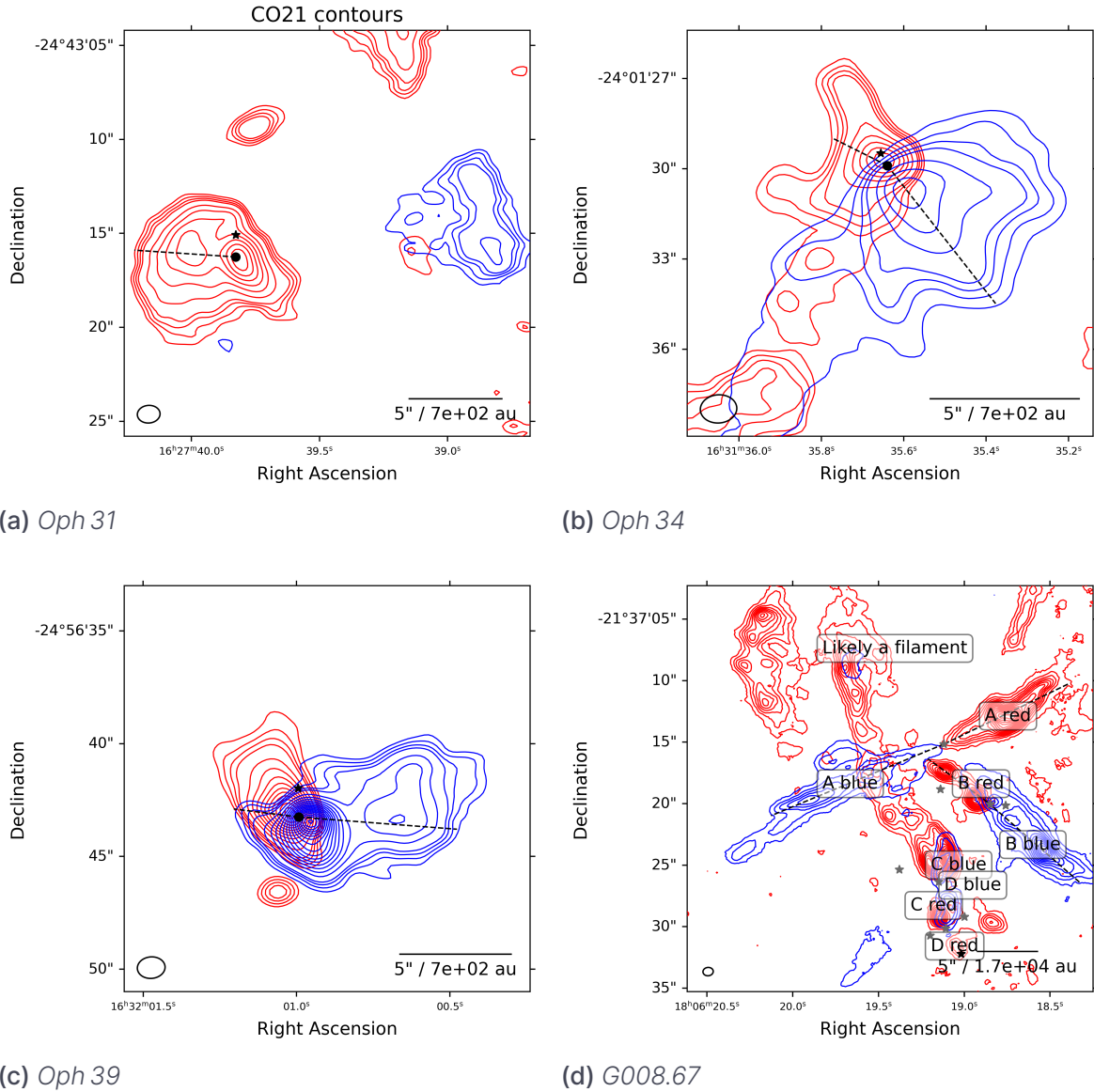
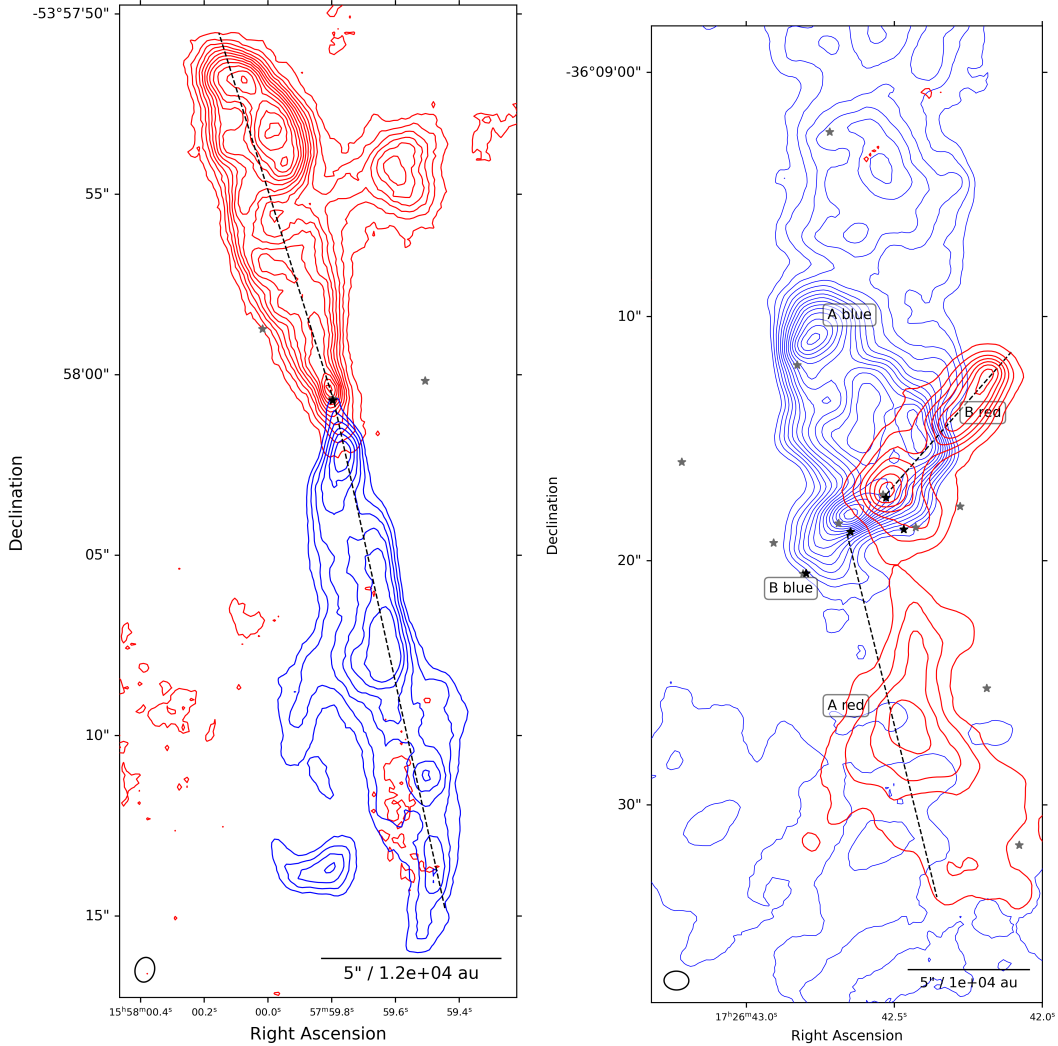
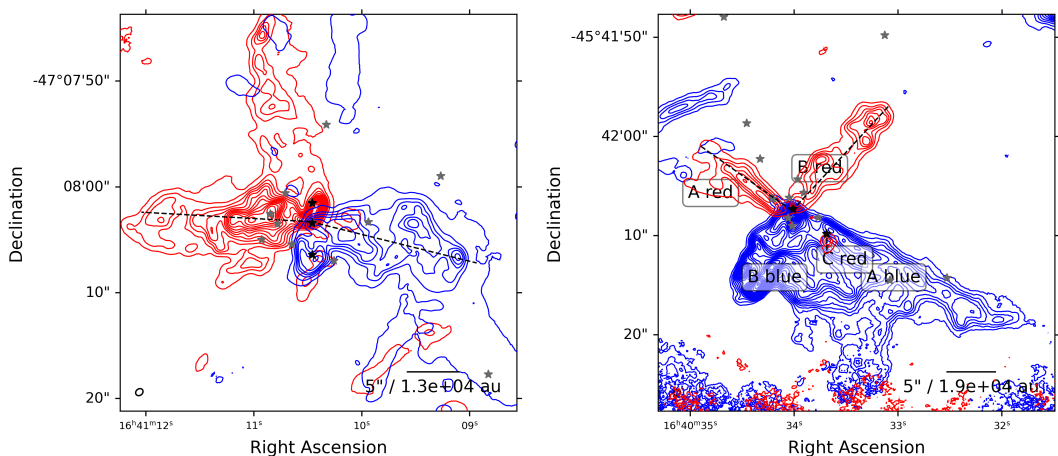


Figure 4.4: Integrated blue- and red-shifted CO (2-1) maps of sources in our low-mass sample (subfigure a-c) and high-mass sample (subfigure d). No smoothing was done on these maps. The velocity ranges used to create the maps are indicated in Table 3.1. For the low-mass sources, the contour levels are at 3σ , 4σ , 5σ , 6σ , and then at intervals of 3σ . The positions of the YSOs are indicated as black stars, if the position of the outflow axis is manually altered from the position of the YSO, the new position is indicated as a black circle. For the high-mass source G008.67, contour levels start at 3σ , and are then at intervals of 5σ . The positions of the hot cores are indicated as black stars, the positions of the continuum cores are indicated as gray stars.



(a) G328.25. The red contour levels start at 3σ , and are then at intervals of 5σ . The blue contour levels are at $(3, 4, 5, 6, 7, 8)\sigma$, and then at intervals of 5σ .

(b) G351.77. The red contour levels start at 3σ , and are then at intervals of 10σ . The blue contour levels start at 3σ , and then at intervals of 20σ .



(c) G337.92. The red contour levels start at 3σ , and are then at intervals of 10σ . The blue contour levels start at 3σ , and then at intervals of 20σ .

(d) G338.93. The contour levels start at 3σ , and are then at intervals of 5σ . The overlapping blue lobes are not included in any further calculations.

Figure 4.5: Integrated blue- and red-shifted CO (2-1) maps of sources in our high-mass sample. No smoothing was done on these maps. The velocity ranges used to create the maps are indicated in Table 3.1. Contour levels for specific sources are indicated in the sub-captions. The positions of the hot cores are indicated as black stars, the positions of the continuum cores are indicated as gray stars.

Oph 26

The integrated blue- and red-shifted CO (2-1) maps for Oph 26 are indicated in Figure 4.3b. We identify an isolated bipolar outflow in the east-west direction, which was also detected by Van der Marel et al. (2013). They estimate an inclination of 10° , so we are likely observing the source almost pole-on, which is in line with the overlapping lobes and broad angle of this source. Both lobes were labeled as ‘Likely’ and were included in the further morphology analysis.

For the determination of the opening angle, the central bins of the angle distribution of the red lobe were excluded, as the red-shifted lobe contains a slight cavity which would influence the Gaussian fit. The blue lobe is asymmetric, which causes the fitted axis to be significantly offset from the initial axis. A second iteration was therefore done to determine the opening angle of the blue lobe, in which we used the fitted axis from the first iteration as the initial axis. This second iteration axis is indicated in the figure as a dashed-dotted line. By using this new axis for the determination of the opening angle, the opening angle could be fit more reliably.

Oph 27

The integrated blue- and red-shifted CO (2-1) maps of Oph 27 can be found in Figure 4.3c. We identify an outflow in the northwest-southeast direction, which we label as ‘Likely’. There is some additional redshifted emission to the south, which was not included in any further calculation since it is disconnected from the YSO and the bipolar outflow. Van der Marel et al. (2013) has also identified this outflow, and they determine an inclination of 30° , which indicates that we are looking at the outflow quite pole-on. We indeed see quite some overlap between the red and blue lobes.

The pixel chosen for the origin of the axis is slightly offset from the position of the YSO, although the offset is smaller than the astrometric inaccuracy of 2MASS. The new origin was chosen to be in between the peak flux density of the red and blue lobes. The YSO is indicated as a black star in Figure 4.3c, while the origin is indicated as a black circle.

The red lobe is significantly flattened out, which might indicate there is an unresolved cavity influencing the shape of the lobe. Due to this shape, along with the relatively small number of pixels due to the small size of the outflow, no reliable fit could be achieved, and no opening angle was determined for this lobe.

Oph 29

The integrated blue- and red-shifted CO (2-1) maps of Oph 29 can be found in Figure 4.3d. We identify a red-shifted lobe, however the blue-shifted lobe does not seem to be connected to the central YSO. The blue lobe was therefore not included in any further calculations.

Van der Marel et al. (2013) also identify this outflow, although they find a very broad red-shifted lobe to the east and a broad blue-shifted outflow to the west, coinciding with the disconnected blue lobe we find. Their identification indicates that we might be resolving out some emission. Furthermore, they observe a

larger field of view and indicate the presence of a different YSO with an outflow, which falls just outside of the field of view of our observations. Therefore we find that this field might be quite chaotic, with multiple outflows interacting.

We thus only identify the radius, dynamical age, and opening angle of the redshifted lobe, which we label as 'Likely'. The blue lobe is labeled 'Possible' and is not included in further calculations. For the determination of the opening angle, we mask out some pixels on the opposite side of the YSO, as these pixels will influence the fitting. Furthermore, we mask out the parts furthest from the protostar. The opening angle is determined by the wings of the distribution, therefore masking out the central parts of the distribution is allowed.

Oph 31

The integrated blue- and red-shifted CO (2-1) maps of Oph 31 can be found in Figure 4.4a. We identify a red lobe and a disconnected blue lobe in an east-west direction. When comparing it to the smoothed images, we find some blue-shifted flux that is being resolved out in the unsmoothed images. Therefore, we labeled the blue lobe 'Possible' and did not include it in any further calculations. The red lobe is labeled as 'Likely'. Since this source was not included in the sample by Van der Marel et al. (2013), we cannot make a comparison with literature and have no estimation for the inclination.

The starting point of the initial axis of the red lobe was shifted, to better constrain the opening angle. The fitted opening angle is quite wide ($\alpha = 209 \pm 14^\circ$).

Oph 34

The integrated blue- and red-shifted CO (2-1) maps of Oph 34 can be found in Figure 4.4b. We identify a bipolar outflow in the northeast-southwest direction, which we label as 'Likely'. The opening angle appears wide, and there are low SNR wings on the south side for both the red and blue lobes. The identification of these sources corresponds well with the findings of Van der Marel et al. (2013), who further estimate this source to be quite pole-on, with an inclination of 30°.

For the determination of the opening angles, the southern parts of the red and blue lobes were masked out, as they carry the same weight as parts of the outflow with much higher flux densities, and would disproportionately influence the fit. Furthermore, a cavity can be seen for both the red and blue lobes. Therefore, the central bins were masked out before fitting the Gaussian distribution, which is allowed as only the wings of the distribution determine the opening angle.

Oph 39

The integrated blue- and red-shifted CO (2-1) maps of Oph 39 can be found in Figure 4.4c. We identify a bipolar outflow in the northwest-southeast direction, with a relatively wide opening angle. We label both lobes of this outflow as 'Likely'. The red and blue lobes do not seem to be aligned, possibly because the outflow might be an unresolved binary outflow, or because the axis might have shifted over time. No inclination is known from literature for Oph 39, although from the overlapping lobes we can suspect it is relatively pole-on.

For the determination of the opening angle, some small disconnected red emission was masked out, as it is likely not part of the red lobe. Some central bins were excluded from the fit, as the angle distribution appears flattened, which might indicate an unresolved cavity. Furthermore a peak in the distribution near -90° was removed, which appeared to be a consequence of the asymmetric morphology of the source. Similarly for the blue lobe, we exclude a peak in the distribution near 60° , which we suspect is caused by the outflow being an unresolved binary, and therefore asymmetric.

G008.67

The integrated blue- and red-shifted CO (2-1) maps of G008.67 can be found in Figure 4.4d. G008.67 is a complex field, at least four bipolar outflows can be identified in the field. Due to the complexity of the field, we also refer to the SiO maps by Towner et al. (2023) to identify the outflows. Outflow A, which has a red and a blue component in the northwest-southeast direction, can be confidently coupled to a continuum core (Cunningham et al., 2023), and has been identified using SiO (Towner et al., 2023). The same is true for outflow B, which has a northeast-southwest direction. Both outflow A and B are classified as 'Likely'. Outflows C and D overlap, and we cannot confidently state which lobe is part of which outflow. Therefore, we do identify these outflows, but classify them as 'Possible' and do not include them in any further calculations. Furthermore, there is some red-shifted emission, which is not coupled to any SiO emission and can not clearly be coupled to a protostar or a blue-shifted lobe. We therefore suspect this emission is a filament rather than an outflow.

For outflow B, some of the angle distribution of the red and blue lobes was masked out. No literature values for the inclination are available, however since the lobes overlap, we suspect outflow B is more pole-on compared to outflow A.

G328.25

The integrated blue- and red-shifted CO (2-1) maps of G328.25 can be found in Figure 4.5a. We identify a bipolar outflow, which appears to be quite edge-on. The blue lobe is at a significantly lower SNR compared to the red lobe, however we find that σ is higher for the blue-shifted map as well, which might explain the discrepancy. This offset in σ does not significantly influence the determined radii and opening angles.

The redshifted lobe has an asymmetric feature far away from the protostar, which might be old emission or unrelated to the outflow. This feature was masked out in the determination of the opening angle.

G337.92

The integrated blue- and red-shifted CO (2-1) maps of G337.92 are shown in Figure 4.5c. At first sight, the source looks like a single bipolar outflow, however there are many hot cores (Bonfand et al., 2024) and continuum cores (Cunningham et al., 2023) identified in the central parts of the field. Towner et al. (2023) also identify multiple disconnected outflows in SiO, although not all red-shifted lobes can be coupled to blue-shifted lobes. We identify a bipolar outflow in the

east-west direction and use this outflow for further morphology calculation, but there are likely multiple overlapping outflows in the vertical direction. Therefore we mask out some parts of the outflow when determining the opening angle, that are likely overlapping. The masked-out parts are near the center of the outflow.

G338.93

The integrated blue- and red-shifted CO (2-1) maps of G338.93 can be found in Figure 4.5d. We identify two bipolar outflows, in a northeast-southwest direction (outflow A) and in a northwest-southeast direction (outflow B). It might be a very wide single outflow, since the blue-shifted lobes overlap. However, the direction of the SiO emission suggests that they are two separate outflows. In the region of the overlapping blue-shifted lobes, a small redshifted lobe connected to a hot core can be identified, which we label outflow C. However, we cannot disentangle the blue-shifted lobe belonging to outflow C from the blue lobes of outflows A and B. Therefore, the red lobes of outflows A, B, and C are classified as 'Likely', while the blue lobes are classified as 'Possible', and not included in further calculations. Due to the limited amount of pixels in the redshifted outflow C, no angle determination was made for this source. However we can determine a radius and dynamical age for the red lobe of outflow C.

G351.77

The integrated blue- and red-shifted CO (2-1) maps of G351.77 can be found in Figure 4.5b. We identify two binary outflows, outflow A in the north-south direction, and outflow B in the northwest-southeast direction. The blue lobes overlap significantly, and we therefore do not use them in further calculations. For the red lobe of outflow B, some parts of the lobe were masked out when determining the opening angle, to account for emission on the opposite side of the YSO.

5. Discussion

Again, I think it would help to have an introductory paragraph here to put things into context: even just a summary of what you are going to discuss and why

Also, having your conclusion statements as header titles is quite original.
But you could also consider these as in fact your bullet points conclusions?
In which case you may have to revise the header titles.

5.1 High-mass outflows might be warmer than low-mass outflows.

In Figure 5.1, we compare the mean value of T_{rot} for our high- and low-mass samples. The mean was taken over the entire field since the resolution of the smoothed maps was too low to accurately identify individual outflows. The high-mass outflows are indicated as upper limits, as we suspect the majority of pixels in the high-mass fields is optically thick in the CO (2-1) transition, causing us to overestimate T_{rot} (see Section 3.2.1 and below). The rotational temperatures for the low-mass sample are likely affected by non-LTE effects, as suspected by the deviation in the RDs of some low-mass sources (see Section 3.2.2). T_{rot} remains only an estimation of the true kinetic temperature of the gas. Non-LTE modeling would be required to properly constrain the kinetic temperature of the low-mass sources. Since we cannot determine whether we overestimate or underestimate the temperatures, we do not plot the rotational temperatures for the low-mass sample as upper limits.

The values of T_{rot} in our low-mass field range between ~ 6 K to ~ 60 K. We determine the mean value of T_{rot} over our low-mass fields, and find a range between 8.3 K and 21.8 K, with a weighted mean over all fields of 11.3 ± 0.6 K. These values are in line with values found from other studies ($T_{ex} \sim 10 - 50$ K, e.g. Lada, 1985; Blake et al., 1995; Bontemps et al., 1996; Yıldız et al., 2012; Dunham et al., 2014). In this project we only study outflows using low-J transitions of CO, therefore we are unable to trace warmer parts of the outflows, which might be detected using high-J CO transitions.

The values for T_{rot} in the high-mass fields range from negative numbers to $\sim 10^4$ K. These values are nonphysical, as negative rotational temperatures cannot exist, and the observed temperature range of outflows is 10 – 50 K. These nonphysical values are caused by the majority of the pixels in the high-mass fields being optically thick in the CO (2-1) transition. Therefore, we mask out any negative values and any pixel with $T_{rot} > 200$ K, and interpret the high-mass rotational temperatures as upper limits. Observations of higher-J CO transitions or observations of CO isotopologues would be required to determine the rotational temperatures of the high-mass outflows more accurately.

When we determine the mean value of T_{rot} over each field, we find a range between 22.6 K and 58.9 K, with a weighted mean over all fields of 28 ± 6 K. As

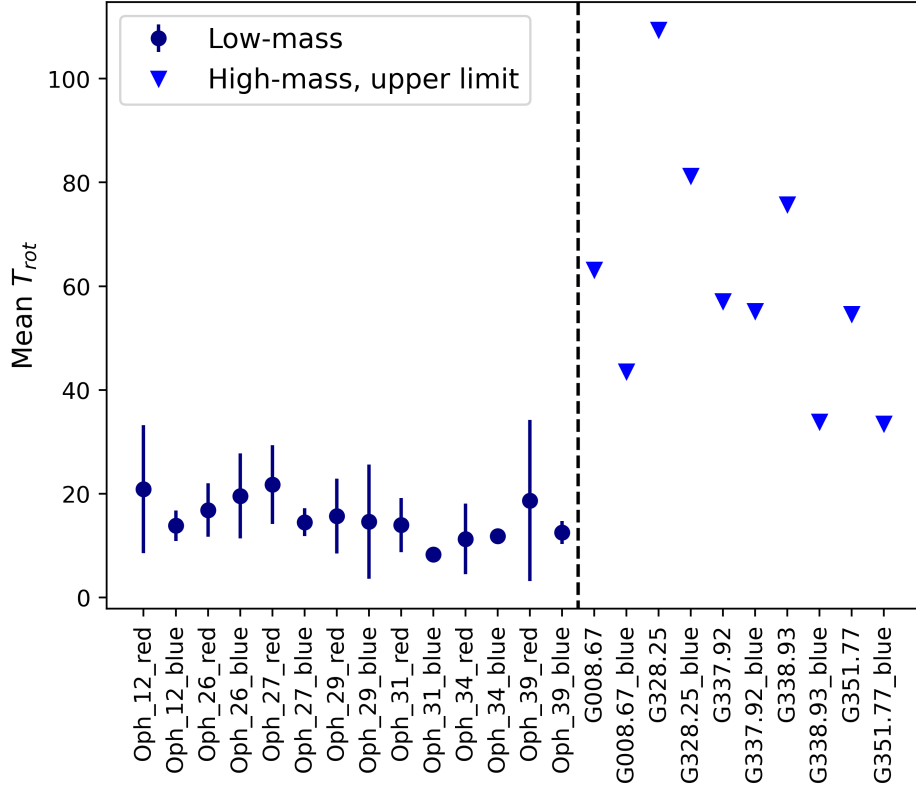


Figure 5.1: Mean values of the rotational temperatures over the entire field, separately for the red- and blue-shifted maps. The high-mass temperatures are indicated as upper limits and are plotted as the derived values from the RD method plus 1σ .

we only determine upper limits on T_{rot} for our high-mass sample, comparisons with the low-mass sample or with literature are limited. McKee & Tan (2003) state that high-mass stars initially emerge from the same temperature gas as low-mass stars, and eventually reach temperatures of $T \sim 50 - 100$ K. The values we find for our high-mass sample do not contradict this statement, but we are unable to confirm it. In conclusion, the rotational temperatures for high-mass outflows are indeed slightly higher than the temperatures derived for low-mass outflows. However, due to severe limitations in our analysis, we cannot determine whether it is a significant difference.

5.2 High-mass fields have more molecular material than low-mass outflows

We indicate the mean CO column densities that we derived for both our low-mass and high-mass samples in Figure 5.2, where the mean was taken over the entire red- and blue-shifted fields.

For the low-mass fields, mean column densities per field range between $8 \cdot 10^{14} \text{ cm}^{-1}$ and $1.26 \cdot 10^{16} \text{ cm}^{-1}$, with a weighted mean of $2.0 \cdot 10^{15} \pm 0.2 \cdot 10^{15} \text{ cm}^{-1}$. Compared to the column densities found by Tychoniec et al. (2019), the weighted

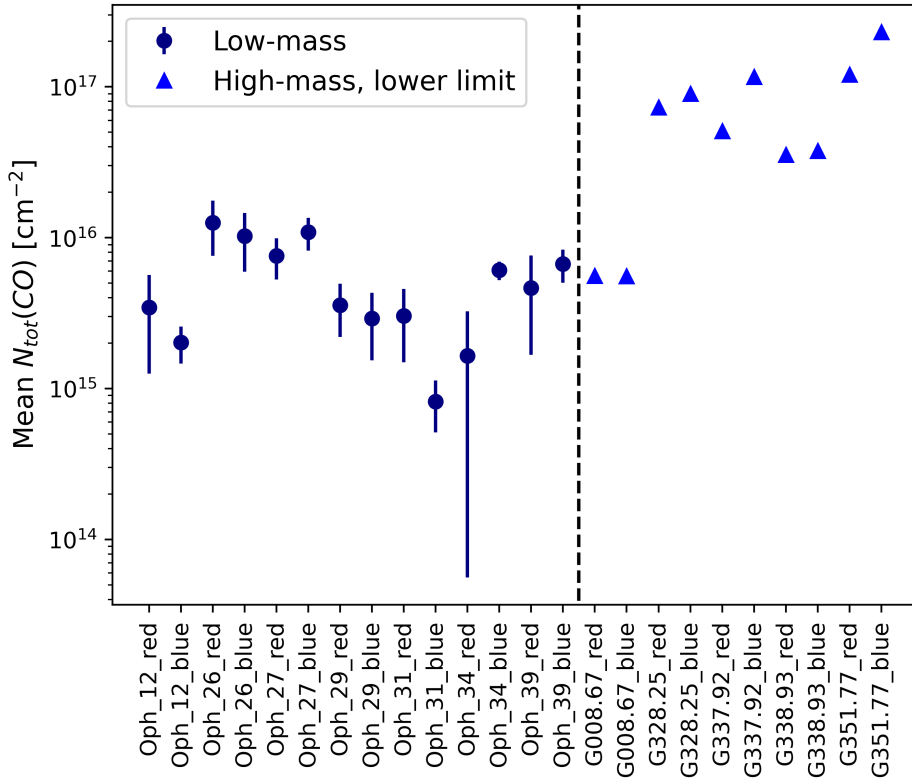


Figure 5.2: Mean column densities over the high- and low-mass fields, separately for the red- and blue-shifted maps. For high-mass fields, values are lower limits and indicated as the value derived from the RD method minus 1σ .

mean column density of our low-mass samples is lower than the values they find in any of their sources (range between $4 \cdot 10^{16}$ and $5 \cdot 10^{17}$ cm $^{-2}$ for low-mass fields). This difference might be caused by a limited sample size in both of our works, as well as a difference in methodology. They determine column densities using the CO (2-1) line and an assumed value of T_{ex} of 75 K, which is a higher value than typical values of T_{rot} determined in this work. Furthermore, we have stated that low-mass sources might not be in LTE, or could contain multiple gas components, which might further influence the results we find.

For the high-mass fields, we only determine lower-limit values for the column densities, as we suspect the majority of pixels is optically thick. The mean column densities per field we find for the high-mass sample range between $6.3 \cdot 10^{15}$ cm $^{-1}$ and $2.6 \cdot 10^{17}$ cm $^{-1}$, with a weighted mean of $9.0 \cdot 10^{15} \pm 0.6 \cdot 10^{15}$ cm $^{-1}$. Comparisons to literature are difficult due to these lower limits. However, our results is in line with the findings by Lefloch et al. (2015), who observe an intermediate-mass outflow using low-J CO transitions and find column densities of $9 \cdot 10^{16}$ cm $^{-2}$, which is indeed higher than the lower-limit column densities we find.

We find that the high-mass fields have significantly higher CO column densities than the low-mass fields. This result is in line with previous studies, as high-mass outflows are typically both larger (e.g. Maud et al., 2015a) and more massive

(e.g. Li et al., 2018) than low-mass outflows, suggesting that there is also a larger content of molecular gas.

5.3 High-mass outflows are larger and move faster than low-mass outflows

The outflow radii of our low-mass sample are between $3 \cdot 10^2$ au and 10^3 au, which are significantly lower than the values determined by Van der Marel et al. (2013), who find low-mass outflow radii between $3 \cdot 10^3$ and $1 \cdot 10^4$ au. As indicated in Chapter 4, we find that Van der Marel et al. (2013) observe at a lower resolution ($15''$), and they observe a larger field of view. Therefore, we might be resolving out emission that is observable in their sample, and we might be more sensitive to compact emission that is unresolvable in their observations.

We find values of R for our high-mass sample between $1.5 \cdot 10^4$ au and $5.5 \cdot 10^4$ au, with an outlier for G338.93_C of $5 \cdot 10^3$ au.. Maud et al. (2015a) have observed 99 high-mass YSOs in the J=3-2 transition of C¹⁸O, and Maud et al. (2015b) have observed this same sample using ¹²CO and ¹³CO, at a resolution of $15.3''$. They determine radii by defining a source aperture and calculating an effective circular radius. This radius is then deconvolved from the beam. They find a range of deconvolved radii between $1 \cdot 10^4$ au and $5 \cdot 10^4$ au. Therefore we find that the determined radii in our work are in the same order of magnitude compared to their work.

For our low-mass sample, we find values for $\Delta v = v_{out} - v_{LSR}$, between 2.4 and 15.2 km s^{-1} for Δv , which coincides well with the velocity ranges defined by Van der Marel et al. (2013), who find values of Δv between 3 and 12 km s^{-1} .

We find values of Δv for our high-mass sample in the range of 35 to 90 km s^{-1} . An outlier is G351.77, which has velocities up to 130 km s^{-1} . Reasons for this source being an outlier are described below. Maud et al. (2015a) find a range of high-mass outflow velocities between 5 and 35 km s^{-1} , significantly smaller than the velocities we define. The difference in high-mass velocity ranges might be caused by them defining the velocities using C¹⁸O, which might be detectable in a smaller range of velocity bins compared to CO emission. Towner et al. (2023) find values of Δv roughly between 15 and 100 km s^{-1} from SiO observations of the same sources in our sample, which is more in line with the velocities we detect.

We find significantly higher radii for the high-mass sample compared to the low-mass sample. The weighted mean of the radii for our low-mass sample is $6.5 \cdot 10^2 \pm 5 \cdot 10^1$ au, while the weighted mean radius for the low-mass sample is $2.7 \cdot 10^4 \pm 1 \cdot 10^3$ au. This value might be biased, as high-mass YSOs are more distant, and therefore we only identify massive outflows with larger radii. However, the absence of such large radii in the low-mass sample indicates that high-mass sources are generally larger than low-mass outflows.

This result is in line with expectations, as high-mass stars tend to show larger mass-loss rates than low-mass outflows (Bally, 2016; Arce & Sargent, 2006), which should correspond to larger outflows. The increased mass-loss rates

and larger outflows might be caused by higher accretion rates that are required since high-mass stars have to accrete more mass in a similar accretion timescale ($5 - 10 \cdot 10^5$ yr, Arce & Sargent, 2006).

We find higher values for Δv for our high-mass sample compared to our low-mass sample. The weighted mean in Δv is $4.90 \pm 0.09 \text{ km s}^{-1}$ for the low-mass sample, while the weighted mean in Δv for the high-mass sample is $54.8 \pm 0.9 \text{ km s}^{-1}$. This difference might tell us that high-mass sources are more energetic and have a larger outflow force. Van der Marel et al. (2013) state that the outflow force F_{CO} is calculated as

$$F_{CO} = \frac{M(\Delta v)^2}{R}, \quad (5.1)$$

where M is the mass of the outflow. Since the outflow force is more strongly dependent on Δv than on R , we might find that the high-mass sources have a higher outflow force compared to low-mass outflows. However, since we do not determine M in this project, we can not confidently determine such a relation.

An outlier in Δv is G351.77, which has significantly higher values of Δv compared to other high-mass sources. Leurini et al. (2009) identify extremely high-velocity wings $|v - v_{\text{lsr}}| > 120 \text{ km s}^{-1}$ in CO lines for this source, which coincides with the high values of v_{out} we identify. We find that there is quite some emission in the field, both red- and blue-shifted, that we cannot couple to an outflow. Towner et al. (2023) study the SiO (5-4) transition of G351.77 and also find additional large-scale, high-velocity emission that does not appear to trace individual outflows. They identify multiple possible explanations, such as there being an 'explosive outflow', or that a massive protostar has recently undergone an episodic accretion event in the field. A third possibility is that multiple outflows are aligned with each other, causing the high-velocity wings. However, this explanation is not preferred due to the low likelihood of both outflow axis alignment alignment of red-shift and blue-shift. Towner et al. (2023) has announced a future separate paper specifically on the high-velocity wings of this source

5.4 High-mass outflows show longer periods of dynamical activity than low-mass outflows

We have determined t_{dyn} for each identified lobe in our high- and low-mass sample in Section 4.1.5, as indicated in Figure 5.3. For sources with known inclination, we correct for this value. For sources with no known inclination, we correct for possible values of i ($i = [30, 50, 70]^\circ$).

We find that when we compare the uncorrected values, high-mass outflows (weighted mean of $1.57 \cdot 10^3 \pm 0.07 \cdot 10^3$ yr) have significantly larger dynamical timescales compared to low-mass outflows (weighted mean of $3.2 \cdot 10^2 \pm 0.2 \cdot 10^2$ yr). This difference is in agreement with the findings of Li et al. (2020), who find that dynamical timescales increase with core mass.

The dynamical timescales we determine for the high-mass sample are significantly smaller than the dynamical timescales determined by Maud et al. (2015b),

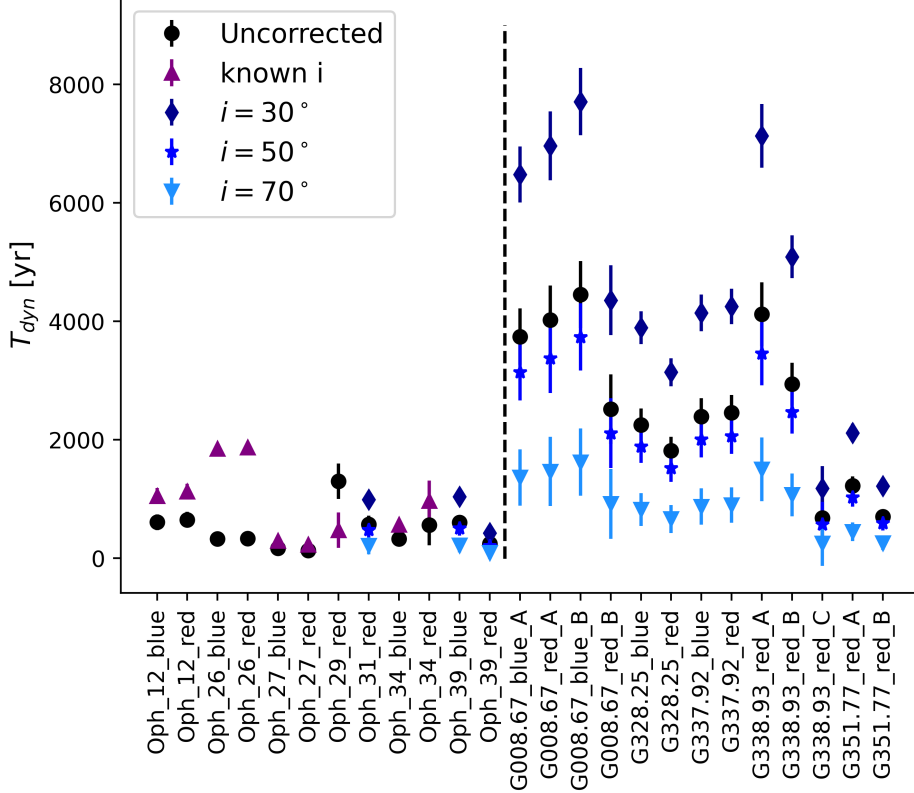


Figure 5.3: Dynamical timescales for all sources in our low-mass (left) and high-mass (right) sample. The values uncorrected for inclination are indicated as black dots. For the low-mass sources with known inclination (Van der Marel et al., 2013), the corrected value is indicated as a purple triangle. For all other sources with no known inclination, corrected dynamical timescales are indicated for $i = [30, 50, 70]^\circ$.

who find values between $2 \cdot 10^4$ yr and $2.5 \cdot 10^5$ yr. However, their radii were determined using a different method, and their sources were not fully resolved, which might explain the discrepancies in the results.

Outliers in t_{dyn} are G338.93_C and G351.77, which are high-mass sources with similar dynamical timescales compared to the low-mass sources. G338.93_C is an outflow that is significantly shorter than the other outflows in the cluster (A and B), which is likely why we find smaller dynamical timescales. This outflow could have been launched more recently, or it might be a low-mass outflow in a high-mass cluster. The values of t_{dyn} for G351.77 are smaller than other high-mass outflows, likely because of the high-velocity wings that have been reported for this source (Leurini et al., 2009; Towner et al., 2023). The shorter dynamical timescales might indicate that the source is highly dynamic.

Care should be taken in interpreting t_{dyn} , as often it is not representative of the true age of the outflow. Such a comparison would only hold if the outflow is launched as the protostar is formed, and keeps ejecting mass continuously over time. This is not realistic, as outflows are highly episodic (e.g. Billot et al., 2012; Safron et al., 2015; Mairs et al., 2017), which means that t_{dyn} is rather

representative of the timescale of the dynamical activity, and thus the timescale of consecutive accretion events. It should therefore only be used to estimate dynamical parameters between studies using the same methods.

5.5 High-mass outflows are more collimated than low-mass outflows

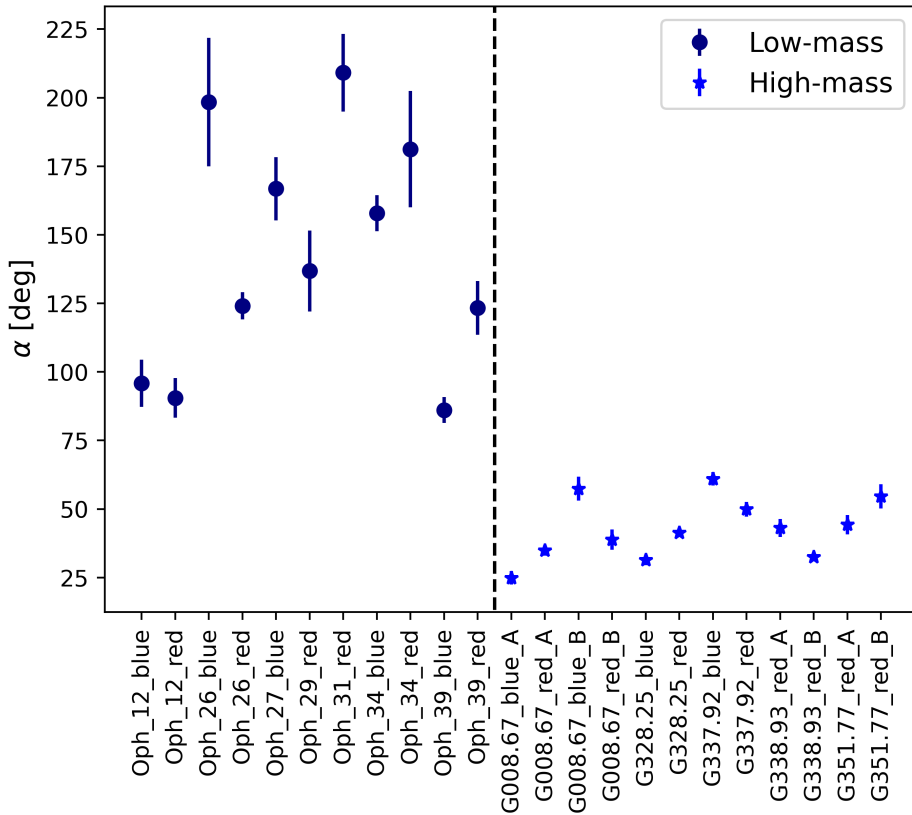


Figure 5.4: Derived opening angles for all outflows in our low- and high-mass sample. Opening angles are uncorrected for inclination.

In Figure 5.4, we compare the derived opening angles, as determined in Chapter 4, between the high- and low-mass samples. We find that high-mass sources have significantly smaller opening angles compared to high-mass sources. For the low-mass sample, we find a weighted mean opening angle of $119 \pm 2^\circ$, while for the high-mass sample, we find a weighted mean opening angle of $38.5 \pm 0.6^\circ$. The mean opening angle we find for our high-mass sample is in line with Mignon-Risse et al. (2021), who find high-mass outflow opening angles in the range of 30-70°.

Outflow opening angles are dependent on inclination since all angles observed are projected on the plane of the sky. Since for most sources, the inclination is either unknown or highly uncertain, no inclination correction was applied on the opening angles. However, we expect the inclination to be distributed randomly for the high- and low-mass samples, therefore our comparison still holds. We find

that high-mass outflows have smaller opening angles than low-mass outflows, and are thus more collimated.

High-mass sources having smaller opening angles is in conflict with the findings by Richer et al. (2000) and Wu et al. (2004), who find high-mass outflows to be less collimated than low-mass outflows. However, Richer et al. (2000) determine that their results might be biased by selection effects, as high-mass outflows with small opening outflows might have been missing from the sample. Wu et al. (2004) also mention that multiple outflows might be unresolved and identified as a single outflow, which would be more prevalent for high-mass outflows as they occur in more clustered environments (e.g. Tan et al., 2014; Zhang et al., 2015). Therefore the difference between our work and earlier research might be caused by the limited resolution and sample size of high-mass sources.

Since high-mass stars typically form in more clustered environments, it might be expected that high-mass protostellar outflows would have larger opening angles than low-mass stars. In clustered environments, there is significant sub-structure and clumpy material, and surrounding YSOs and outflows are more likely to interact with the outflow. Both of these factors would increase the opening angle of a high-mass protostellar outflow.

The smaller opening angles for high-mass outflows that we find might be explained by them having larger outflow forces and being more energetic, as was also suggested in Section 5.3. The increased energy in an outflow would allow it to remain collimated for longer, despite the clustered environment.

According to the high-mass outflow evolutionary track established by Beuther & Shepherd (2005), well-collimated high-mass outflows are young and are not associated with an UCHII region yet, and the opening angle increases as a wide-angled wind starts to dominate. As we mostly identify small opening angles for the high-mass sources, we suggest that the high-mass outflows we identified are typically quite young. However, since the proposed evolutionary track does not indicate specific ranges of opening angles, this statement can not be quantified.

The results we find might be biased by selection effects, as we identify and classify outflows 'by eye'. Since high-mass outflows occur in more clustered environments, we might be more likely to label less-collimated outflows as 'Possible', when they overlap or interact with other outflows in the field. Low-mass outflows are often isolated, therefore we often classify an outflow as 'likely', even if it is barely collimated.

5.6 The evolution of opening angles with age

It is generally accepted that outflow opening angles grow as a source ages, due to the interactions with the envelope (e.g. Velusamy & Langer, 1998; Arce & Sargent, 2006; Lee & Ho, 2005). In Figure 5.5, we plot the opening angle of each lobe against the dynamical timescale. We find no correlation between dynamical timescales and opening angles, likely because the dynamical timescale is not a proxy for the true age of a YSO, and rather measures the timescale of dynamical activity.

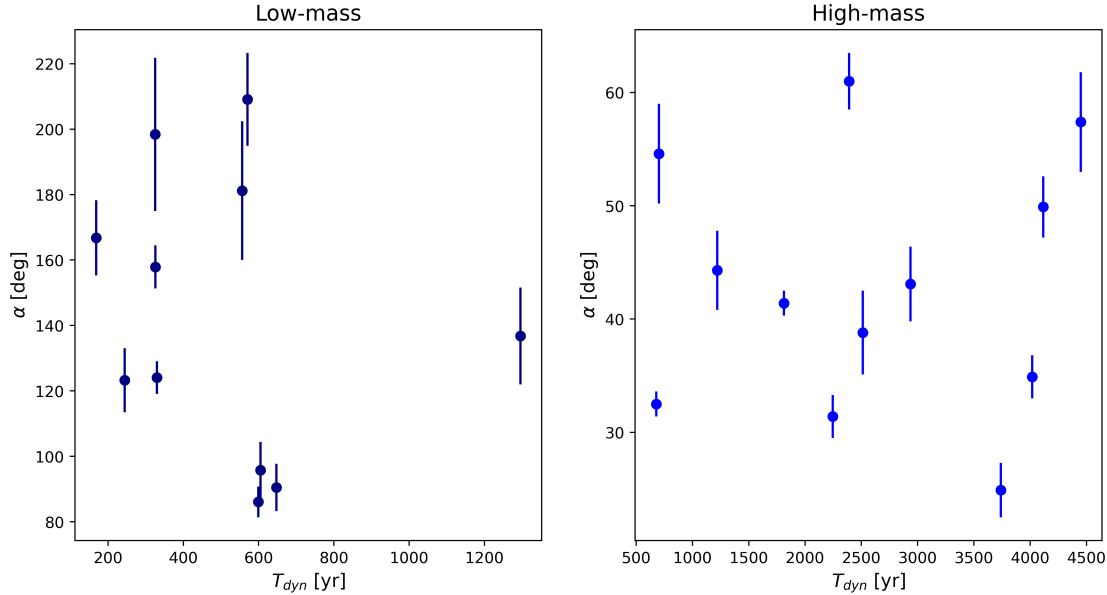


Figure 5.5: Opening angles of low-mass (left) and high-mass (right) outflow lobes, as a function of the dynamical timescale. No correlation can be determined.

In an attempt to determine a relationship between the evolutionary stage and opening angle, we compare our derived opening angles with the evolutionary stages known from Motte et al. (2022) for the high-mass sample, and Van Kempen et al. (2009) for the low-mass sample.

It is important to note that for the high-mass sources, no evolutionary stage is known for individual YSOs. Rather, the evolutionary stage of the clump is known, which is classified as either ‘Young’, ‘Intermediate’, or ‘Evolved’. Of the 12 high-mass lobes for which we define the opening angle, six are in a ‘Young’ cluster, and six are in an ‘intermediate’ cluster. We find the mean opening angle of the ‘Young’ lobes is $43 \pm 2^\circ$, while the mean opening angle for the ‘Intermediate’ lobes is $42 \pm 3^\circ$. Thus, we find no correlation between the protocluster evolutionary stage and opening angles, although this result might be limited by sample size. A relationship might be found if we were to compare the opening angle with the evolutionary stage of individual high-mass YSOs, rather than the cluster evolutionary stage.

For the low-mass samples, evolutionary stages have been determined for individual YSOs. We are again limited by sample size, as four outflows (Oph 12, Oph 26, Oph 27, and Oph 29) are classified as Class I embedded YSO, but only Oph 31 is a Class II source with a protostellar disk. Oph 34 was classified as Class I(T), a source in transition between Class I and Class II. The relation we find in Figure 5.6 does not contradict opening angles growing with the evolutionary stage, however there are too few Class II sources in our sample to properly determine a relation between the opening angle and evolutionary stage.

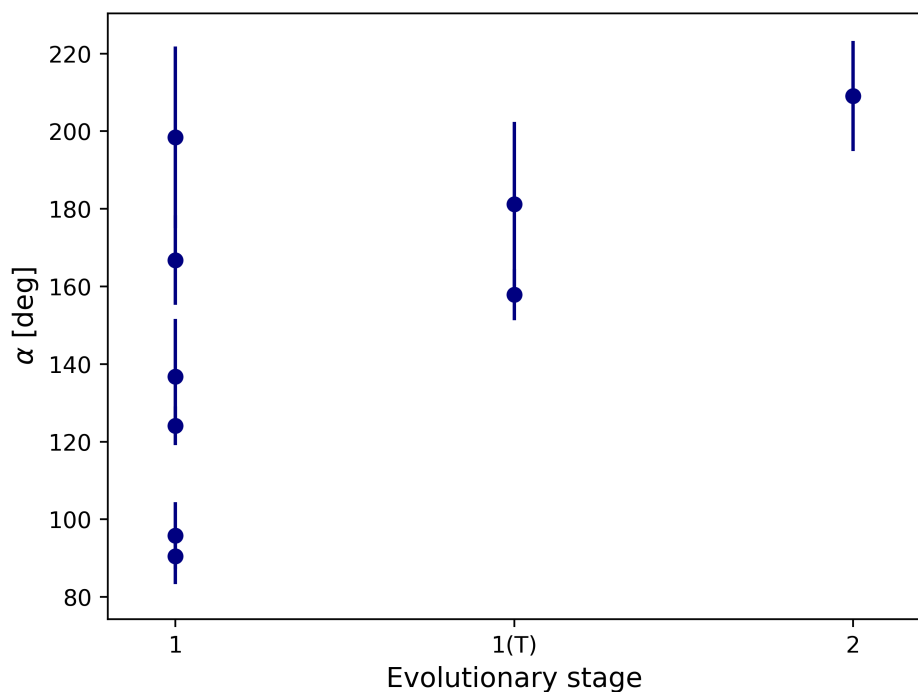


Figure 5.6: The opening angles of low-mass outflow lobes, as a function of the evolutionary stage that was defined by Van Kempen et al. (2009).

6. Conclusions

To be written

A. Appendix

A.1 Constraining the physical high-mass parameters using *RADEX*

As can be seen in figures ..., the assumption that our high-mass fields are optically thin might not always hold. Therefore, the rotational temperatures and column densities we find for the high-mass sources might be unreliable. Since there are only two CO transitions available for the high-mass field, we cannot determine using the rotational diagram whether certain regions in the outflows are optically thin or thick, and whether the LTE assumption truly holds.

We attempted to constrain the excitation temperatures and hydrogen densities independent of optical depth using *RADEX* (van der Tak et al., 2007). *RADEX* is a statistical equilibrium radiative transfer code. Where the rotation diagram method requires the assumption that all transitions are optically thin and in local thermodynamic equilibrium, *RADEX* uses the escape probability formulation assuming an isothermal and homogeneous medium without large-scale velocity fields, which can also deal with optically thick transitions.

We ran *RADEX* for a range of input parameters, from which the code returns a grid of molecular line fluxes in [K km/s] for the CO (2-1) and CO (3-2) lines, which we can then fit to the velocity-integrated fluxes in our fields. Since there are only two lines available that we can fit to, we can only keep two *RADEX* parameters free and we must fix all others. We started with running *RADEX* for G328.25 as for this source it is very apparent that optically thick parts exist since the rotation diagram method resulted in negative temperatures.

The kinetic temperature was entered in a range between 25 K and 225 K, in steps of 25 K. This range was based on results by Hoang et al. (2023), who found an outflow temperature range between 120 and 220 K for high CO ($> J = 11-10$) lines, and on results by Van Kempen et al. (2016) who found temperatures above 50K for outflows observed in CO (6-5). We opted to make this range broader to account for the fact that the lower CO lines we observe might trace colder regions of the outflows. The other free parameter was the hydrogen number density, for which we defined a grid of values between 1e3 and 1e7 [cm⁻³].

We fixed the input column density at $1 \cdot 10^{17}$ [cm⁻²], which were chosen based on the LTE maps of G328.25. For the line width, we selected a fixed value of 15km/s, based on the average of a Gaussian fit to the line wings. Furthermore, we selected the homogeneous slab geometry.

Running *RADEX* using these input parameters resulted in a grid of values for the flux density of the CO (2-1) and CO (3-2) lines, for different combinations of kinetic temperatures and hydrogen number densities. We used the χ^2 goodness-of-fit test to determine which of the values in this grid fit best with the observed velocity-integrated flux densities from our CO (2-1) and CO (3-2) maps. These observed flux densities were determined by taking the mean velocity-integrated flux density over the whole outflow, separately for both the red-shifted and blue-shifted components. The resulting χ^2 values were higher than 80, which indicated that even the lowest χ^2 values would not provide a reliable constraint on the physical circumstances.

Several different attempts were made to constrain the parameters better. By integrating the observed flux densities over smaller regions within the outflow, we expected that the regions would be more homogeneous. This did not result in a better fit. We also ran *RADEX* in a finer grid, which also did not provide a better fit. By changing the column densities to $1\text{e}18[\text{cm}^{-2}]$, lower χ^2 values were found (between 25 and 50), however, this fit resulted in unreliablely high hydrogen densities.

We further attempted to constrain the kinetic temperature and hydrogen number density would be to increase the number of molecular lines available, however, no other ALMA CO measurements are available. It is possible to include multiple molecules in a *RADEX* analysis, different from the rotation diagram method. In the ALMA-IMF program, multiple other molecular lines are available. It is important to ensure these lines trace the same gas as CO. Candidates were the C¹⁸O (2-1) line and the SiO (5-4) line. We opted for the SiO line, as the C¹⁸O line did not seem to be tracing the same gas since no high-velocity wings were detected. The SiO line could also trace different regions since SiO is known to also trace the high-velocity jet. We selected a small region where both the SiO and the CO were emitting strongly and performed the same experiment as above. This does require the SiO column density to be fixed, which was taken as $7 \cdot 10^{12}[\text{cm}^{-2}]$ (e.g. Gibb et al., 2004). Even when including the SiO transition, we were still not able to constrain the physical parameters any better, which might be caused by the SiO line tracing different gas than the CO lines.

As a final attempt, we performed the initial test, so without any SiO detections, on some of the other fields, where fewer pixels had a negative temperature. These provided slightly better χ^2 values, for example between 15 and 40 for the outflows in G338.93. However, the values found for the hydrogen number density would then be $5 \cdot 10^3 \text{ cm}^{-3}$, which is unphysically low (cite!).

We conclude that there is simply too little data available to provide a reliable fit of the high-mass fields using the *RADEX* software. We thus state that it is likely that for parts of the LTE maps, the lines are optically thick, and therefore the resulting temperature in some parts of the high-mass outflows might be overestimated.

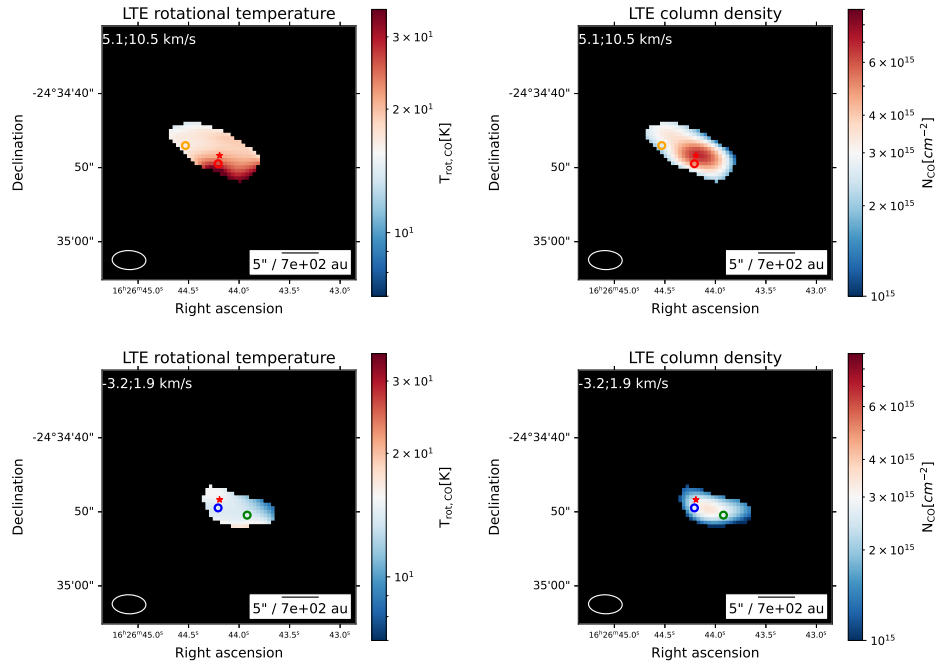


Figure A.1: Caption

A.2 LTE rotational temperature and column density maps

Captions and text to be written

A.3 Angle determination plots

Captions and text to be written

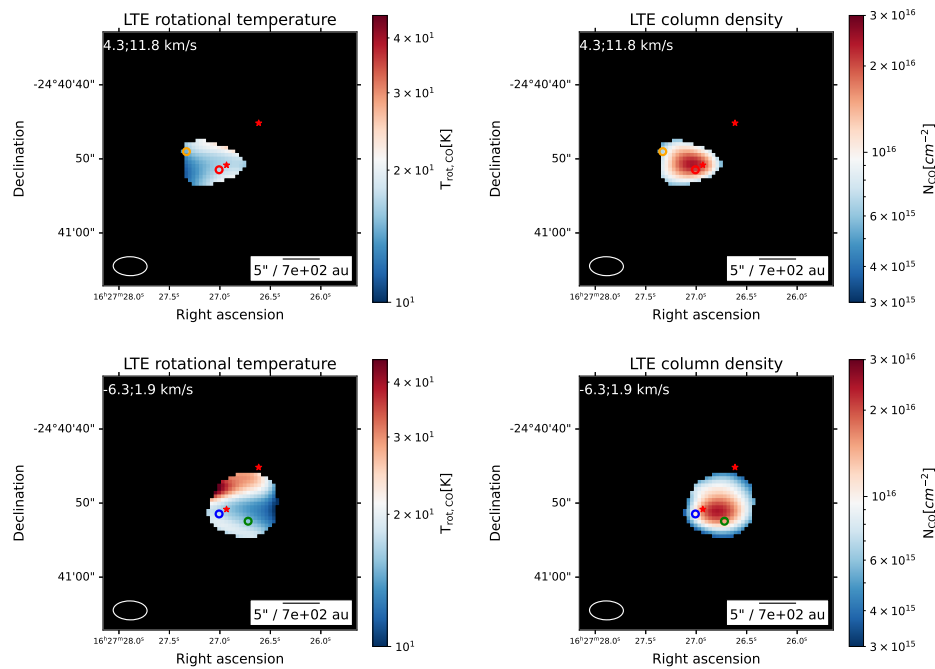


Figure A.2: Caption

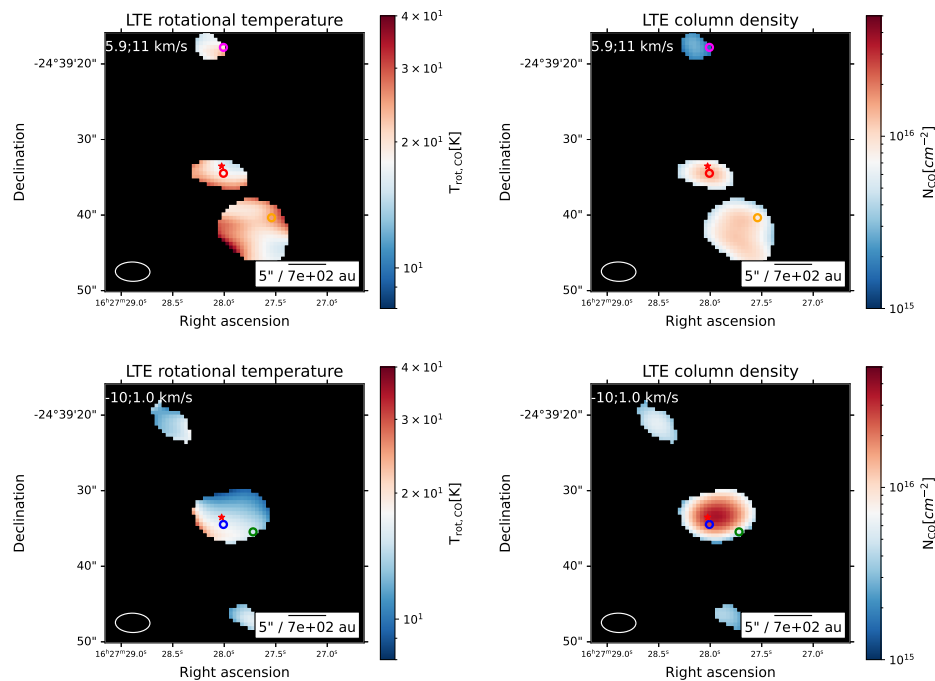
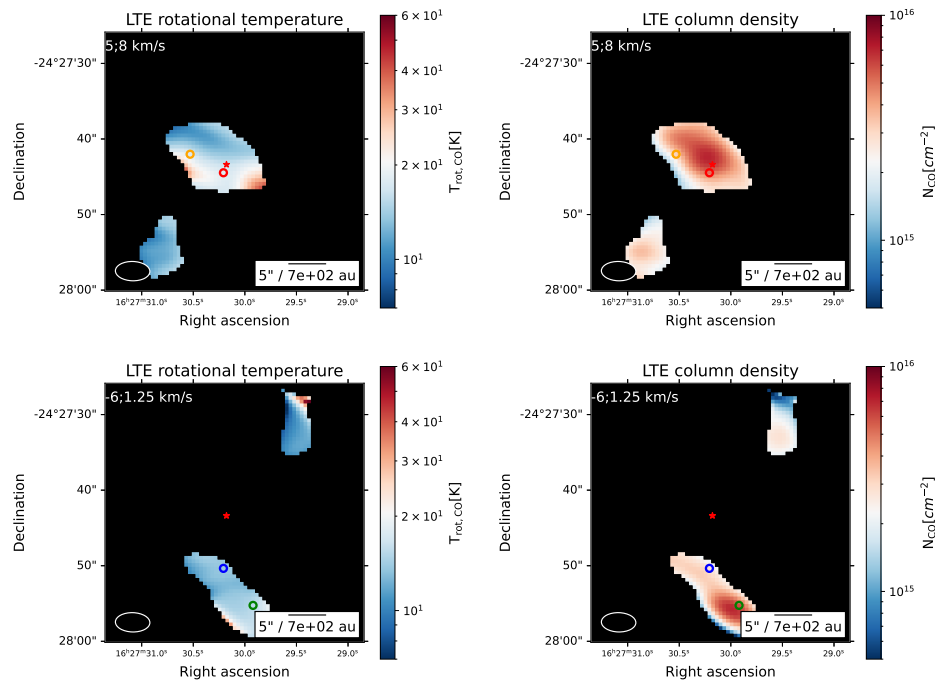
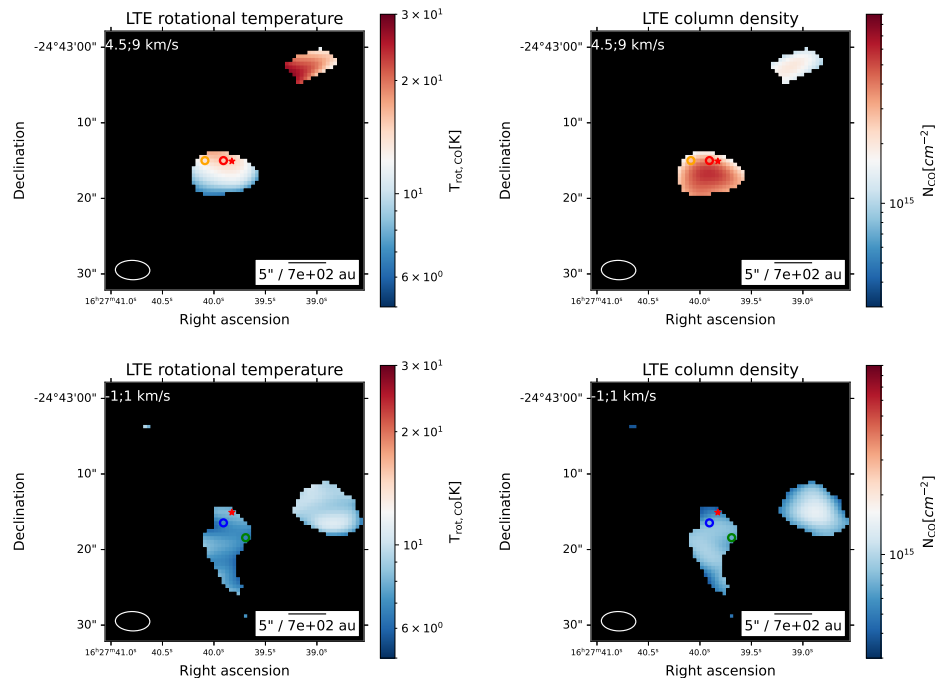
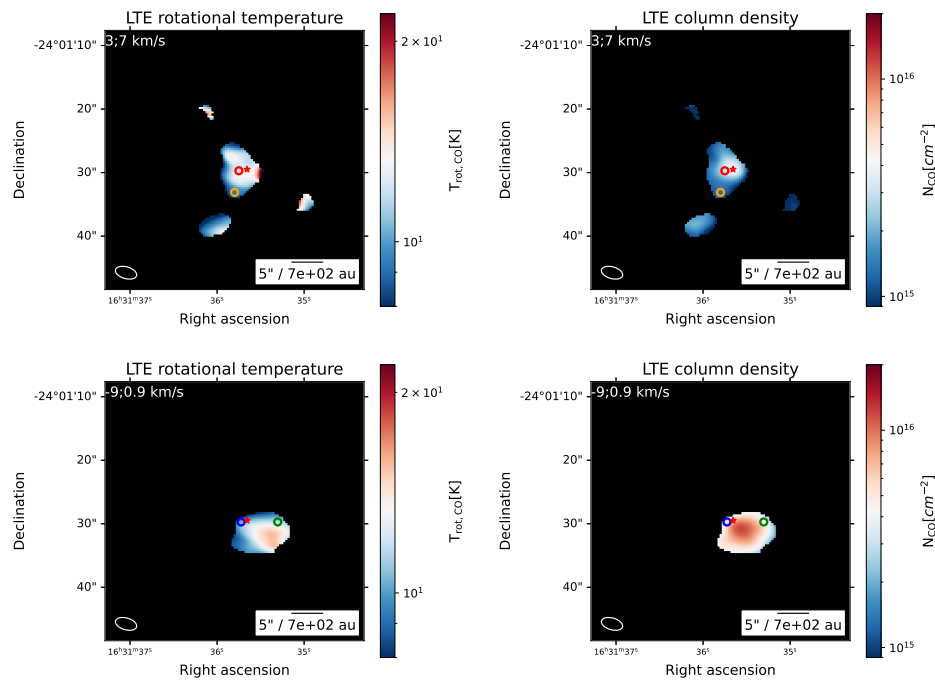
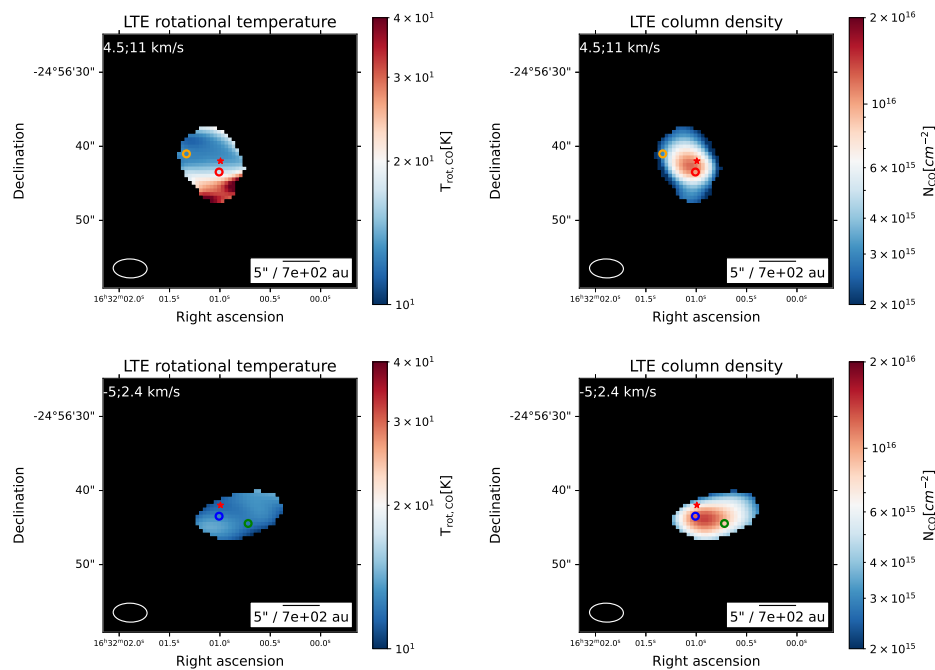
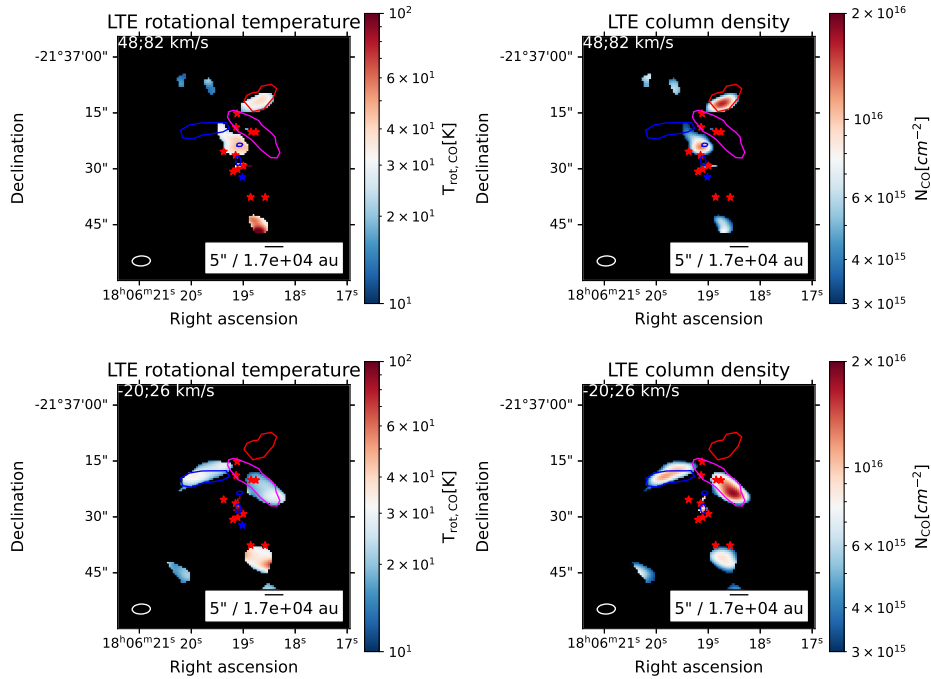
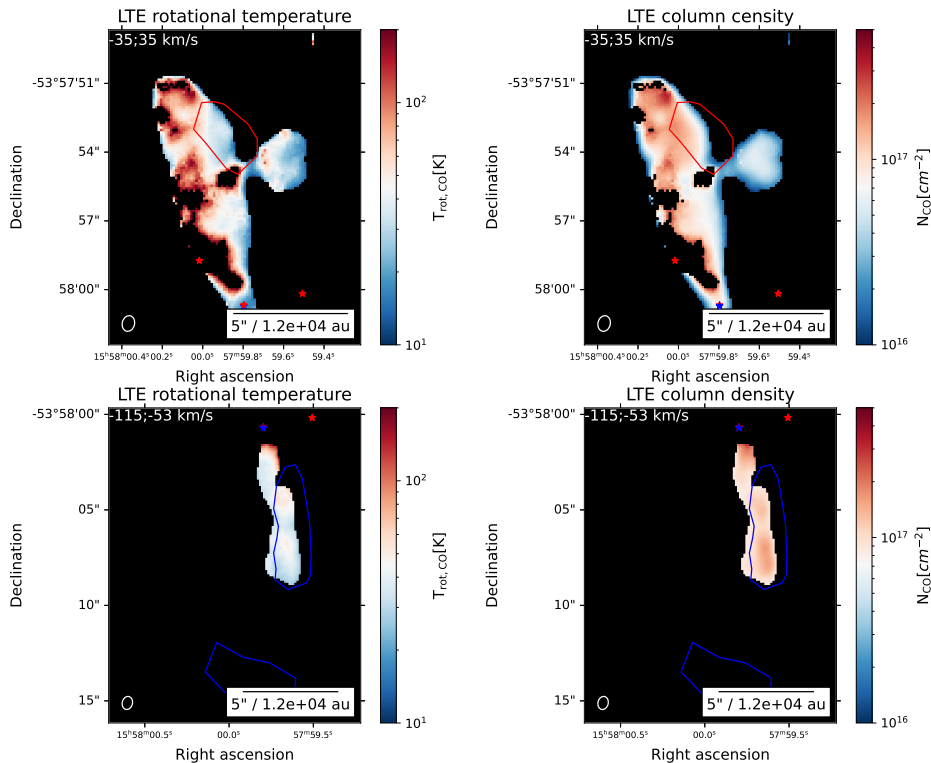
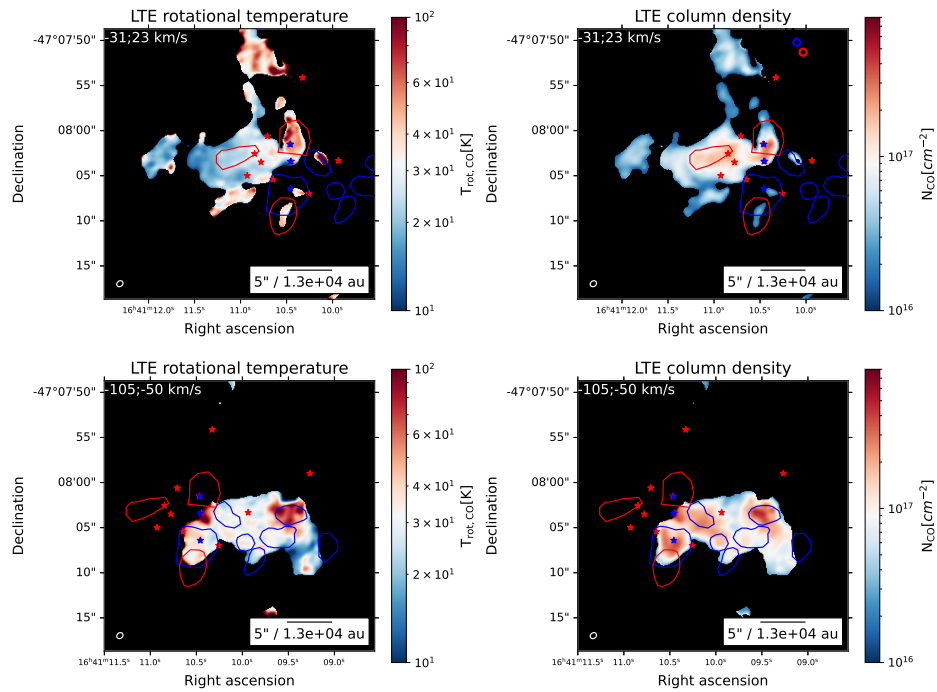
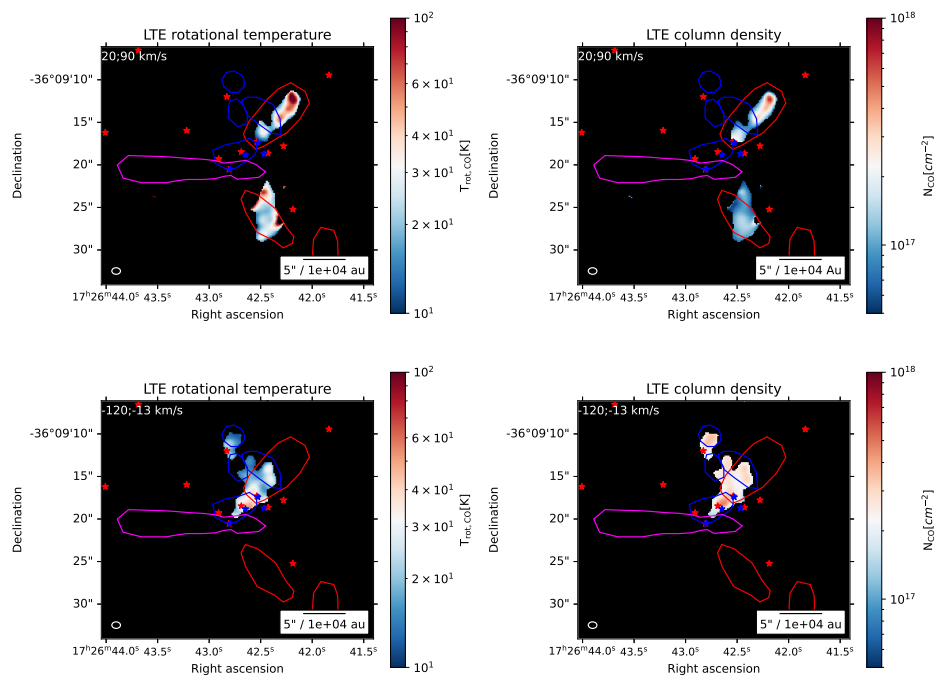


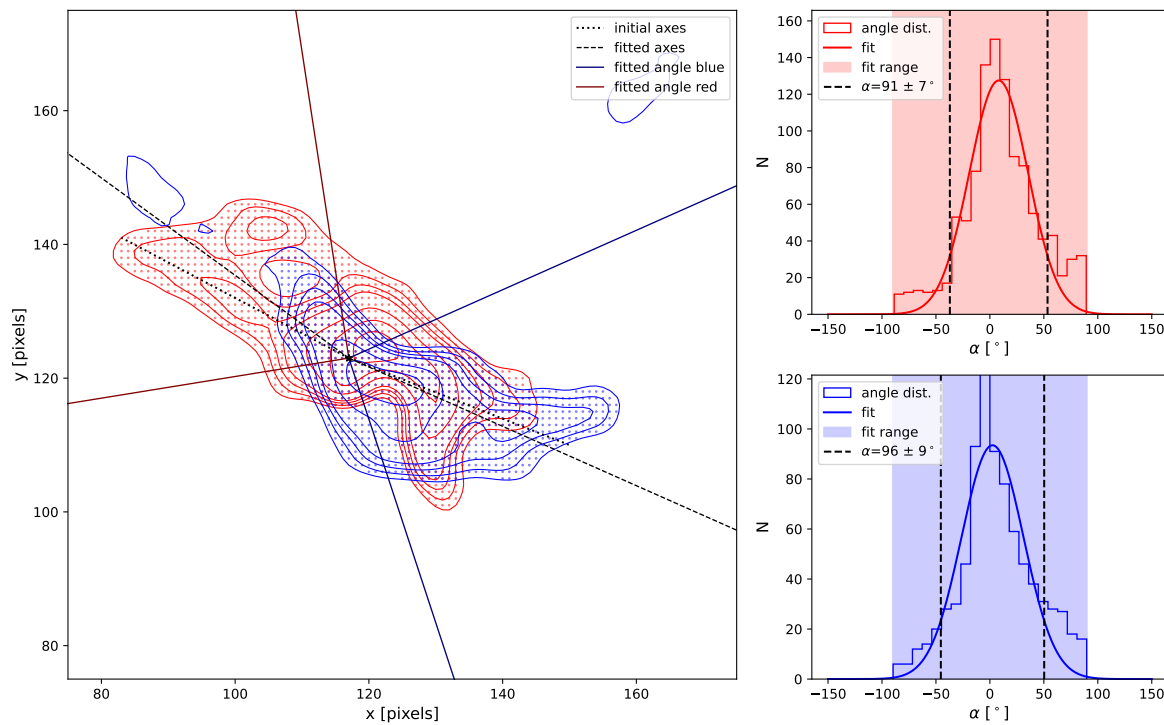
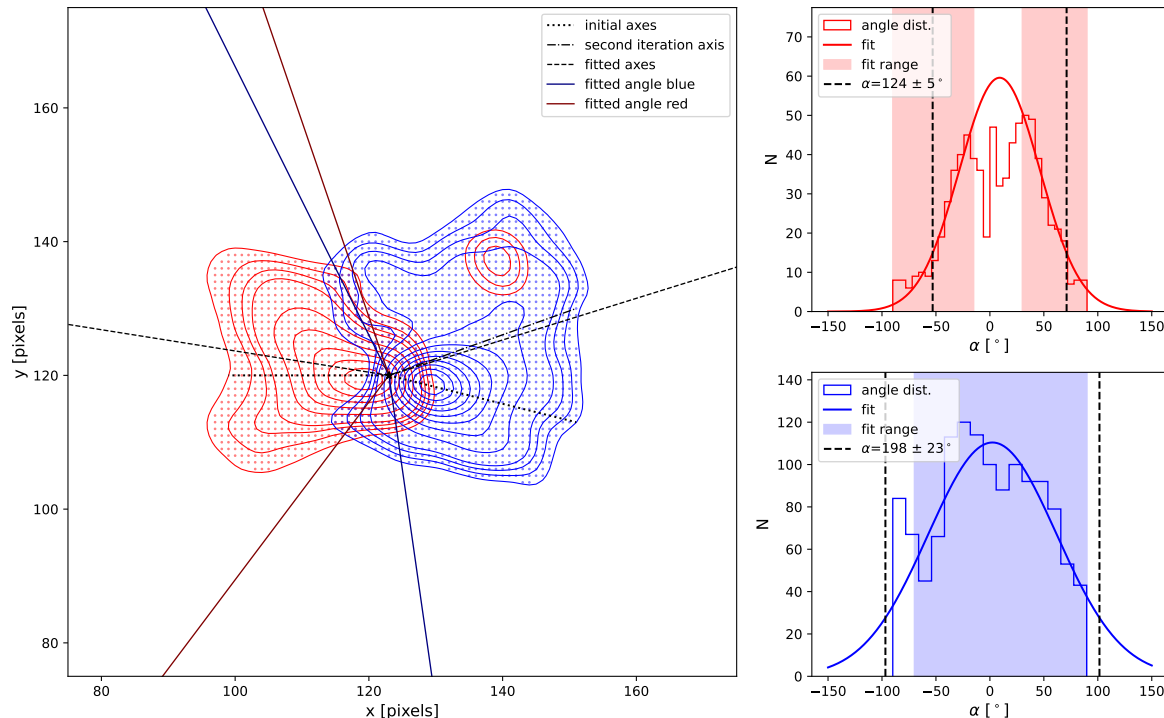
Figure A.3: Caption

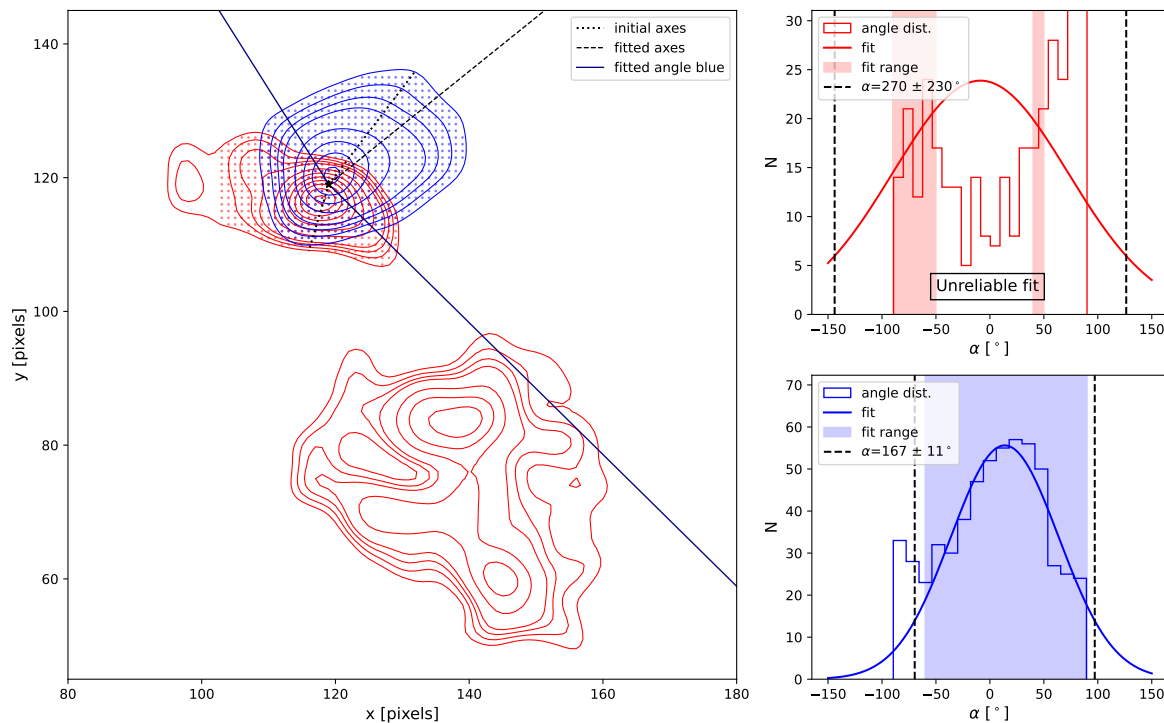
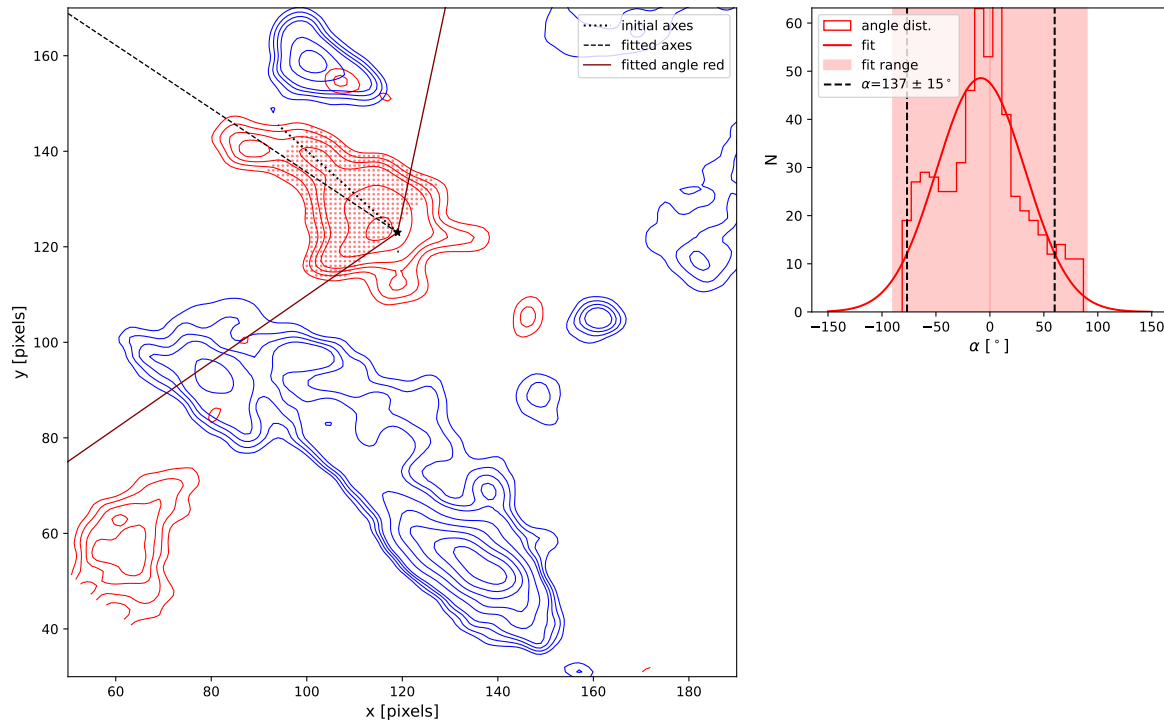
**Figure A.4:** Caption**Figure A.5:** Caption

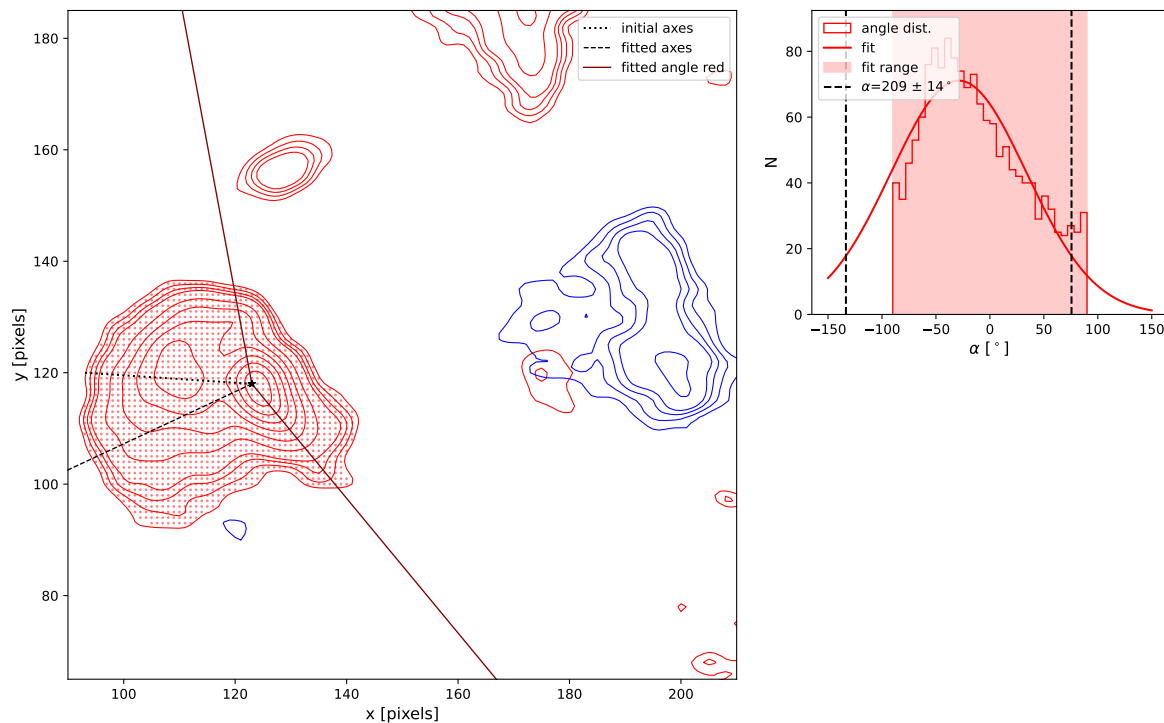
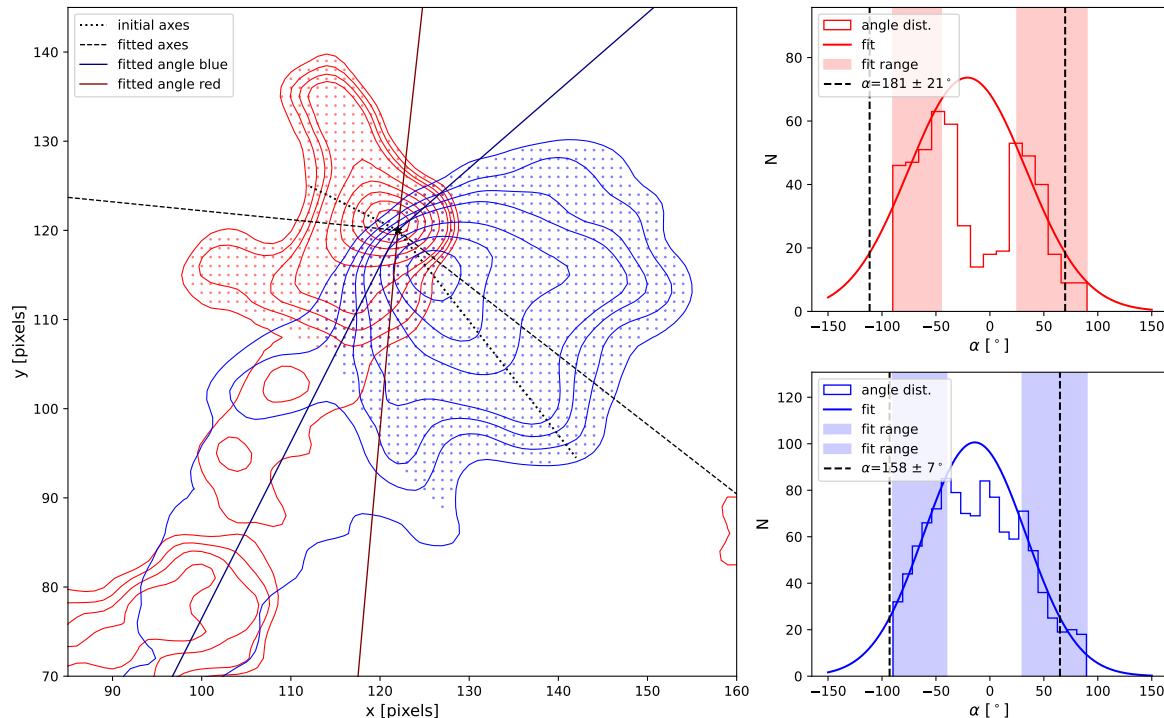
**Figure A.6:** Caption**Figure A.7:** Caption

**Figure A.8:** Caption**Figure A.9:** Caption

**Figure A.10:** Caption**Figure A.11:** Caption

**Figure A.12:** Caption**Figure A.13:** Caption

**Figure A.14:** Caption**Figure A.15:** Caption

**Figure A.16:** Caption**Figure A.17:** Caption

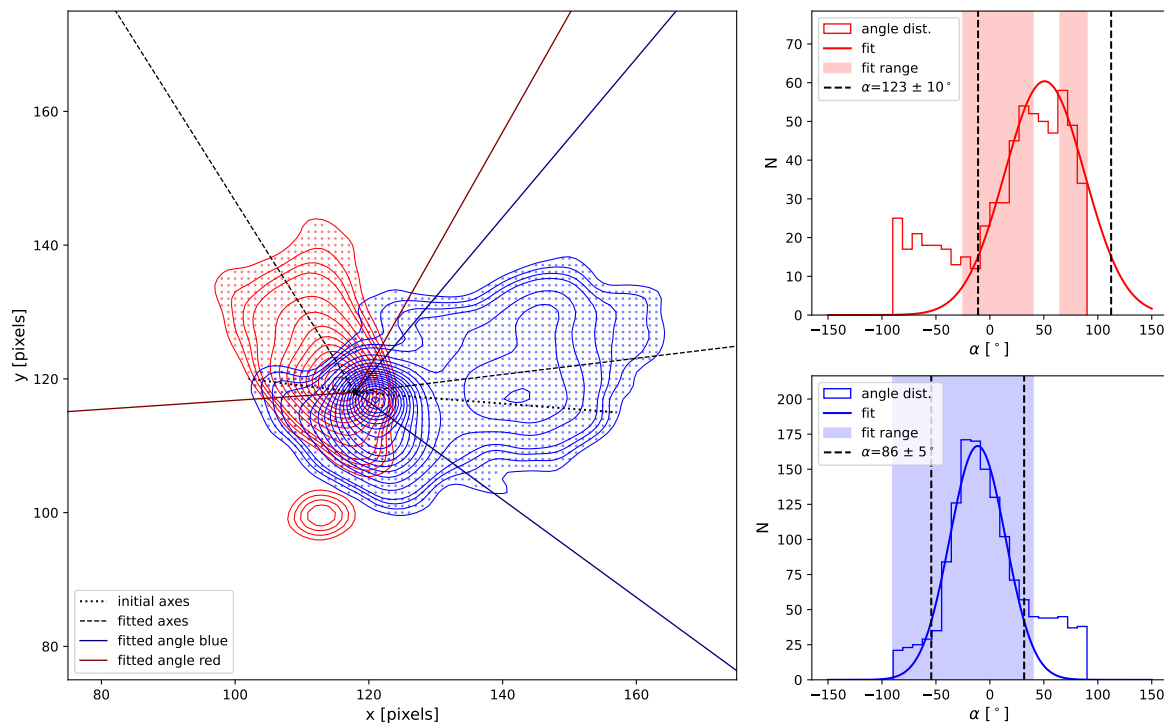


Figure A.18: Caption

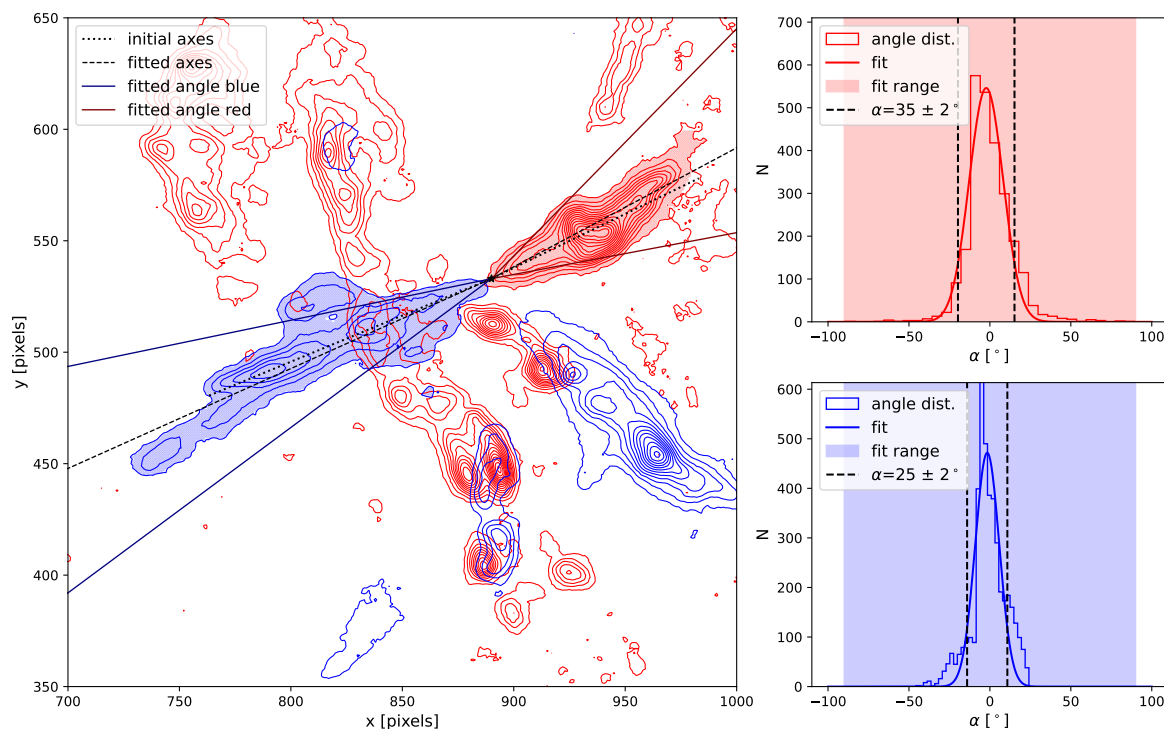


Figure A.19: Caption

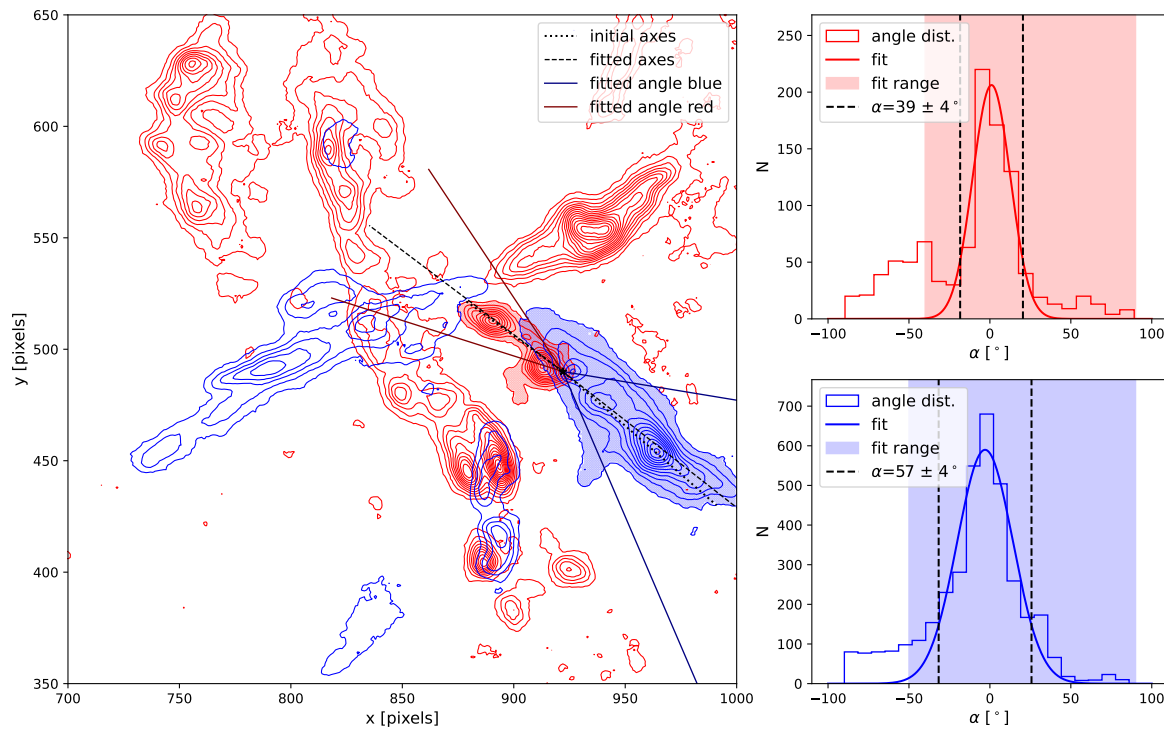


Figure A.20: Caption

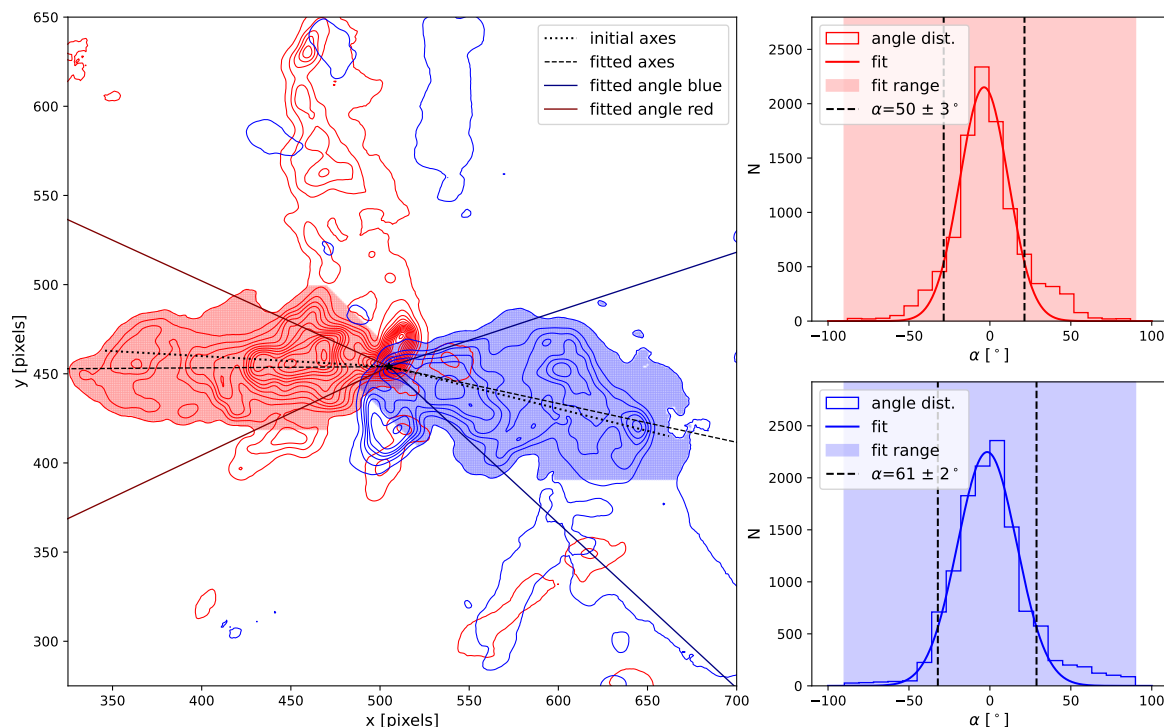


Figure A.21: Caption

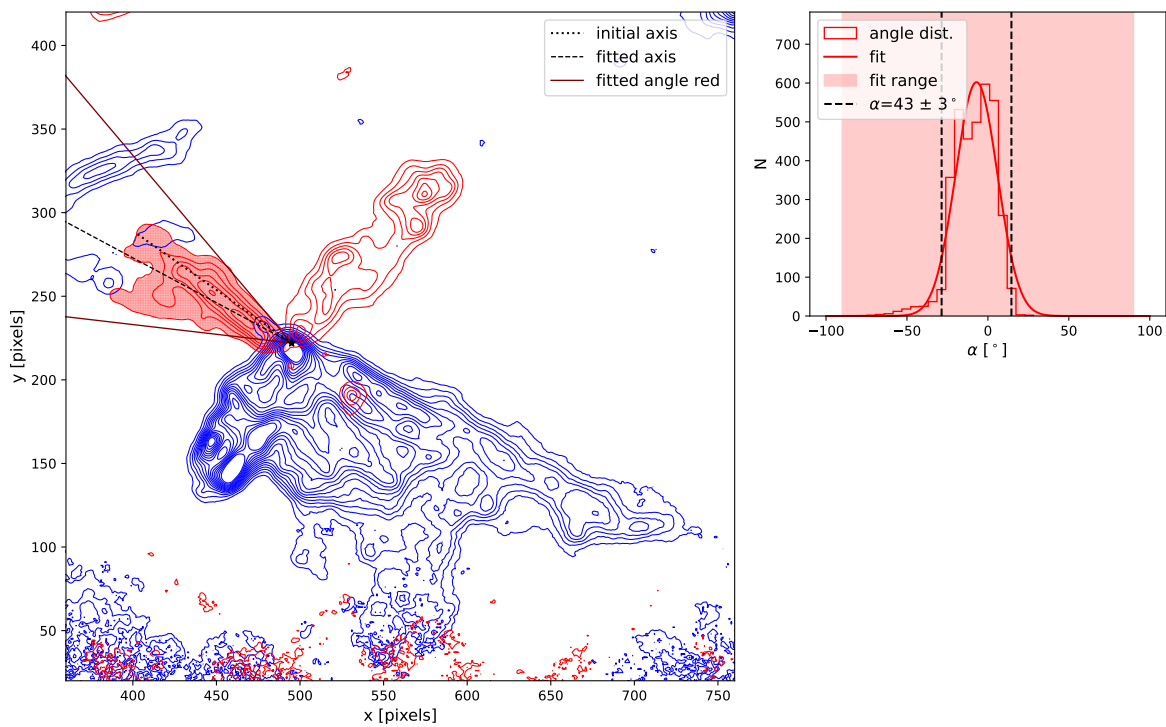


Figure A.22: Caption

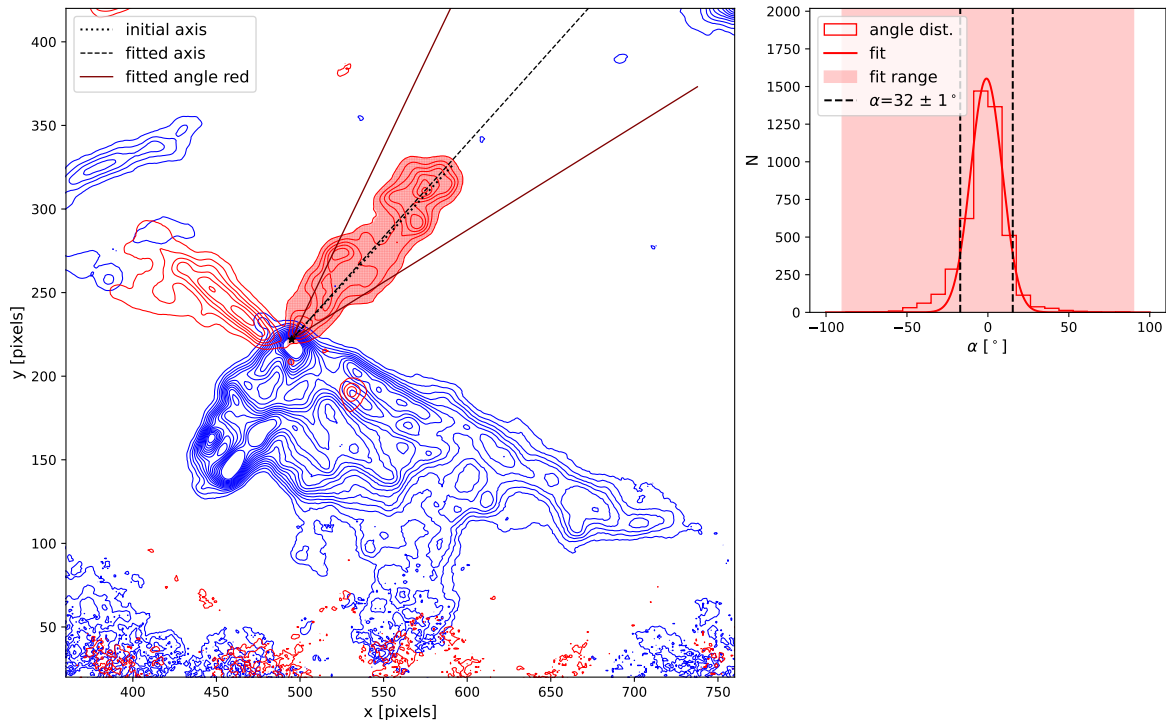


Figure A.23: Caption

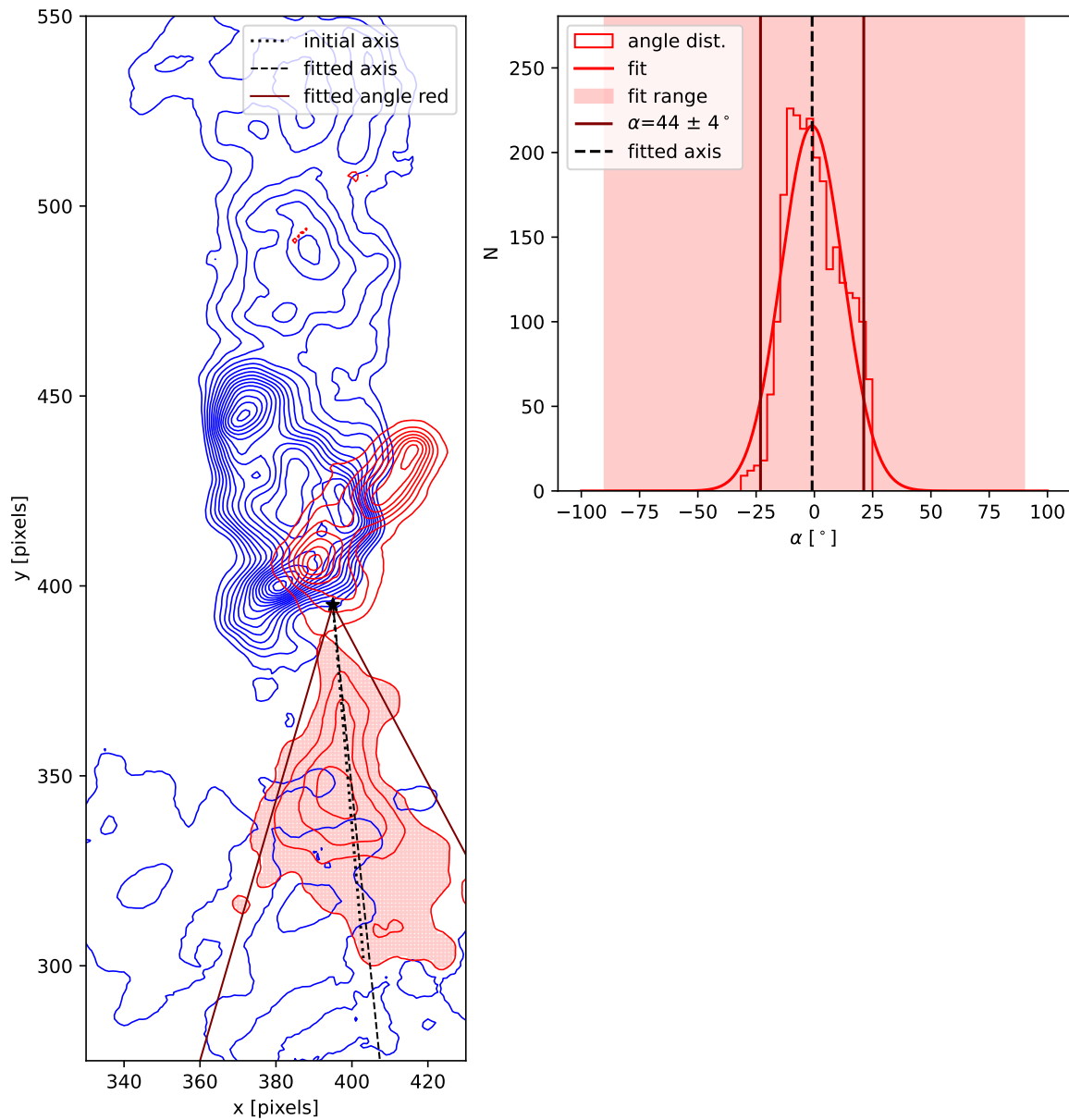


Figure A.24: Caption

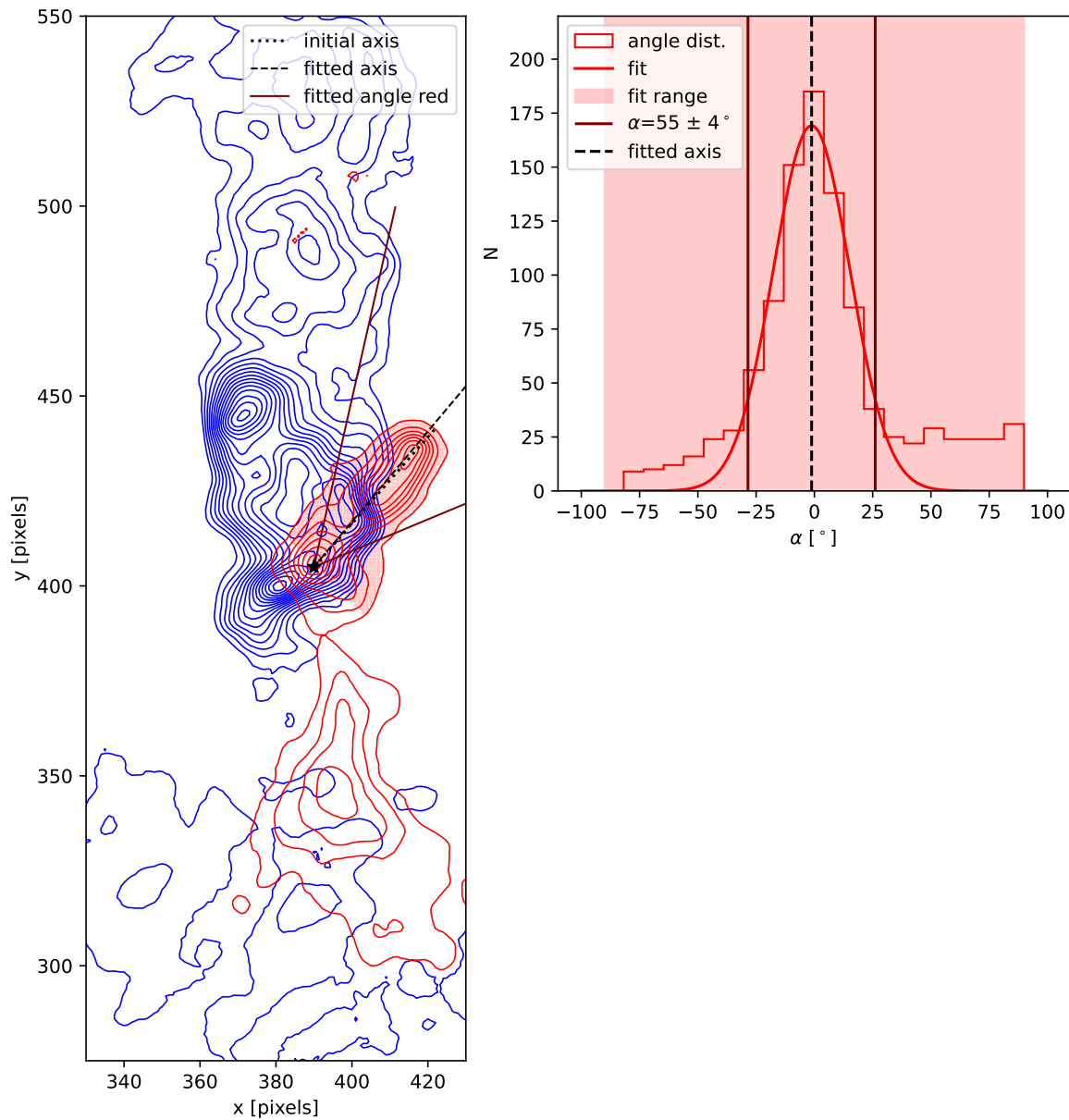


Figure A.25: Caption

Bibliography

- Alves, J., Lombardi, M., & Lada, C. J. 2007, A&A , 462, L17, doi: [10.1051/0004-6361:20066389](https://doi.org/10.1051/0004-6361:20066389)
- Andre, P., & Montmerle, T. 1994, ApJ , 420, 837, doi: [10.1086/173608](https://doi.org/10.1086/173608)
- Arce, H. G., Borkin, M. A., Goodman, A. A., Pineda, J. E., & Beaumont, C. N. 2011, ApJ , 742, 105, doi: [10.1088/0004-637X/742/2/105](https://doi.org/10.1088/0004-637X/742/2/105)
- Arce, H. G., Mardones, D., Corder, S. A., et al. 2013, The Astrophysical Journal, 774, 39, doi: [10.1088/0004-637x/774/1/39](https://doi.org/10.1088/0004-637x/774/1/39)
- Arce, H. G., & Sargent, A. I. 2006, ApJ , 646, 1070, doi: [10.1086/505104](https://doi.org/10.1086/505104)
- Arce, H. G., Shepherd, D., Gueth, F., et al. 2007, in Protostars and Planets V, ed. B. Reipurth, D. Jewitt, & K. Keil, 245, doi: [10.48550/arXiv.astro-ph/0603071](https://arxiv.org/abs/astro-ph/0603071)
- Bachiller, R. 1996, Annual Review of Astronomy and Astrophysics, 34, 111–154, doi: [10.1146/annurev.astro.34.1.111](https://doi.org/10.1146/annurev.astro.34.1.111)
- Bally, J. 2016, Annual Review of Astronomy and Astrophysics, 54, 491–528, doi: [10.1146/annurev-astro-081915-023341](https://doi.org/10.1146/annurev-astro-081915-023341)
- Bally, J., & Lada, C. J. 1983, ApJ , 265, 824, doi: [10.1086/160729](https://doi.org/10.1086/160729)
- Beuther, H., Schilke, P., Sridharan, T. K., et al. 2002, A&A , 383, 892, doi: [10.1051/0004-6361:20011808](https://doi.org/10.1051/0004-6361:20011808)
- Beuther, H., & Shepherd, D. 2005, in Astrophysics and Space Science Library, Vol. 324, Astrophysics and Space Science Library, ed. M. S. N. Kumar, M. Tafalla, & P. Caselli, 105, doi: [10.1007/0-387-26357-8_8](https://doi.org/10.1007/0-387-26357-8_8)
- Billot, N., Morales-Calderón, M., Stauffer, J. R., Megeath, S. T., & Whitney, B. 2012, ApJL , 753, L35, doi: [10.1088/2041-8205/753/2/L35](https://doi.org/10.1088/2041-8205/753/2/L35)
- Blake, G. A., Sandell, G., van Dishoeck, E. F., et al. 1995, ApJ , 441, 689, doi: [10.1086/175392](https://doi.org/10.1086/175392)
- Bonfand, M., Csengeri, T., Bontemps, S., et al. 2024, Astronomy & Astrophysics, 687, A163, doi: [10.1051/0004-6361/202347856](https://doi.org/10.1051/0004-6361/202347856)

- Bonnell, I. A., Bate, M. R., Clarke, C. J., & Pringle, J. E. 2001, MNRAS , 323, 785, doi: [10.1046/j.1365-8711.2001.04270.x](https://doi.org/10.1046/j.1365-8711.2001.04270.x)
- Bonnell, I. A., Bate, M. R., & Zinnecker, H. 1998, MNRAS , 298, 93, doi: [10.1046/j.1365-8711.1998.01590.x](https://doi.org/10.1046/j.1365-8711.1998.01590.x)
- Bontemps, S., Andre, P., Terebey, S., & Cabrit, S. 1996, A&A , 311, 858
- Bontemps, S., André, P., Kaas, A. A., et al. 2001, Astronomy & Astrophysics, 372, 173–194, doi: [10.1051/0004-6361:20010474](https://doi.org/10.1051/0004-6361:20010474)
- Braatz, J., Biggs, A., Sanhueza, P., & Corvillon, A. 2021, ALMA Cycle 8 2021 Proposer's Guide (ALMA). <https://almascience.nrao.edu/documents-and-tools/cycle8/alma-proposers-guide>
- Cabrit, S., Raga, A., & Gueth, F. 1997, in IAU Symposium, Vol. 182, Herbig-Haro Flows and the Birth of Stars, ed. B. Reipurth & C. Bertout, 163–180
- Caselli, P., Hartquist, T. W., & Havnes, O. 1997, A&A , 322, 296
- Chabrier, G. 2003, PASP , 115, 763, doi: [10.1086/376392](https://doi.org/10.1086/376392)
- Connelley, M. S., & Greene, T. P. 2010, AJ , 140, 1214, doi: [10.1088/0004-6256/140/5/1214](https://doi.org/10.1088/0004-6256/140/5/1214)
- Csengeri, T., Bontemps, S., Wyrowski, F., et al. 2017, Astronomy & Astrophysics, 601, A60, doi: [10.1051/0004-6361/201628254](https://doi.org/10.1051/0004-6361/201628254)
- Cunningham, A. J., Krumholz, M. R., McKee, C. F., & Klein, R. I. 2018, Monthly Notices of the Royal Astronomical Society, 476, 771–792, doi: [10.1093/mnras/sty154](https://doi.org/10.1093/mnras/sty154)
- Cunningham, N., Ginsburg, A., Galván-Madrid, R., et al. 2023, Astronomy & Astrophysics, 678, A194, doi: [10.1051/0004-6361/202245429](https://doi.org/10.1051/0004-6361/202245429)
- Deil, C., & Ginsburg, A. 2024, reproject 0.14.0. <https://pypi.org/project/reproject/>
- Downes, T. P., & Cabrit, S. 2007, A&A , 471, 873, doi: [10.1051/0004-6361:20066921](https://doi.org/10.1051/0004-6361:20066921)
- Dunham, M. M., Arce, H. G., Mardones, D., et al. 2014, ApJ , 783, 29, doi: [10.1088/0004-637X/783/1/29](https://doi.org/10.1088/0004-637X/783/1/29)
- Dunham, M. M., Stephens, I. W., Myers, P. C., et al. 2024, Monthly Notices of the Royal Astronomical Society, 533, 3828–3861, doi: [10.1093/mnras/stae2018](https://doi.org/10.1093/mnras/stae2018)
- Dunne, L., Eales, S., Ivison, R., Morgan, H., & Edmunds, M. 2003, Nature , 424, 285, doi: [10.1038/nature01792](https://doi.org/10.1038/nature01792)
- Edwards, S., & Snell, R. L. 1982, ApJ , 261, 151, doi: [10.1086/160326](https://doi.org/10.1086/160326)

- . 1983, ApJ , 270, 605, doi: [10.1086/161152](https://doi.org/10.1086/161152)
- . 1984, ApJ , 281, 237, doi: [10.1086/162093](https://doi.org/10.1086/162093)
- Ellerbroek, L. E., Podio, L., Kaper, L., et al. 2013, A&A , 551, A5, doi: [10.1051/0004-6361/201220635](https://doi.org/10.1051/0004-6361/201220635)
- Endres, C. P., Schlemmer, S., Schilke, P., Stutzki, J., & Müller, H. S. 2016, Journal of Molecular Spectroscopy, 327, 95–104, doi: [10.1016/j.jms.2016.03.005](https://doi.org/10.1016/j.jms.2016.03.005)
- Enoch, M. L., Evans II, N. J., Sargent, A. I., et al. 2008, The Astrophysical Journal, 684, 1240–1259, doi: [10.1086/589963](https://doi.org/10.1086/589963)
- Fall, S. M., Krumholz, M. R., & Matzner, C. D. 2010, ApJL , 710, L142, doi: [10.1088/2041-8205/710/2/L142](https://doi.org/10.1088/2041-8205/710/2/L142)
- Gibb, A. G., Richer, J. S., Chandler, C. J., & Davis, C. J. 2004, The Astrophysical Journal, 603, 198–212, doi: [10.1086/381309](https://doi.org/10.1086/381309)
- Greene, T. P., Wilking, B. A., Andre, P., Young, E. T., & Lada, C. J. 1994, The Astrophysical Journal, 434, 614, doi: [10.1086/174763](https://doi.org/10.1086/174763)
- Gusdorf, A., Pineau Des Forêts, G., Cabrit, S., & Flower, D. R. 2008, A&A , 490, 695, doi: [10.1051/0004-6361:200810443](https://doi.org/10.1051/0004-6361:200810443)
- Hansen, C. E., Klein, R. I., McKee, C. F., & Fisher, R. T. 2012, The Astrophysical Journal, 747, 22, doi: [10.1088/0004-637x/747/1/22](https://doi.org/10.1088/0004-637x/747/1/22)
- Hoang, T. D., Karska, A., Lee, M. Y., et al. 2023, Astronomy & Astrophysics, 679, A121, doi: [10.1051/0004-6361/202347163](https://doi.org/10.1051/0004-6361/202347163)
- Hogerheijde, M. 1998, PhD thesis, University of California, Berkeley, Department of Astronomy
- Könyves, V., André, P., Men'shchikov, A., et al. 2015, Astronomy & Astrophysics, 584, A91, doi: [10.1051/0004-6361/201525861](https://doi.org/10.1051/0004-6361/201525861)
- Könyves, V., André, P., Arzoumanian, D., et al. 2020, Astronomy & Astrophysics, 635, A34, doi: [10.1051/0004-6361/201834753](https://doi.org/10.1051/0004-6361/201834753)
- Kroupa, P. 2002, Science, 295, 82, doi: [10.1126/science.1067524](https://doi.org/10.1126/science.1067524)
- Krumholz, M. R., & Matzner, C. D. 2009, ApJ , 703, 1352, doi: [10.1088/0004-637X/703/2/1352](https://doi.org/10.1088/0004-637X/703/2/1352)
- Kuiper, G. P. 1938, ApJ , 88, 472, doi: [10.1086/143999](https://doi.org/10.1086/143999)
- Lada, C. J. 1985, ARA&A , 23, 267, doi: [10.1146/annurev.aa.23.090185.001411](https://doi.org/10.1146/annurev.aa.23.090185.001411)
- Lada, C. J. 1987, in IAU Symposium, Vol. 115, Star Forming Regions, ed. M. Peimbert & J. Jugaku, 1

- Lada, C. J., & Fich, M. 1996, ApJ , 459, 638, doi: [10.1086/176929](https://doi.org/10.1086/176929)
- Lada, C. J., & Lada, E. A. 2003, ARA&A , 41, 57, doi: [10.1146/annurev.astro.41.011802.094844](https://doi.org/10.1146/annurev.astro.41.011802.094844)
- Lee, C.-F., & Ho, P. T. P. 2005, ApJ , 624, 841, doi: [10.1086/429535](https://doi.org/10.1086/429535)
- Lefloch, B., Gusdorf, A., Codella, C., et al. 2015, A&A , 581, A4, doi: [10.1051/0004-6361/201425521](https://doi.org/10.1051/0004-6361/201425521)
- Leurini, S., Codella, C., Zapata, L. A., et al. 2009, Astronomy & Astrophysics, 507, 1443–1454, doi: [10.1051/0004-6361/200912783](https://doi.org/10.1051/0004-6361/200912783)
- Li, Q., Zhou, J., Esimbek, J., et al. 2018, The Astrophysical Journal, 867, 167, doi: [10.3847/1538-4357/aae2b8](https://doi.org/10.3847/1538-4357/aae2b8)
- Li, S., Sanhueza, P., Zhang, Q., et al. 2020, The Astrophysical Journal, 903, 119, doi: [10.3847/1538-4357/abb81f](https://doi.org/10.3847/1538-4357/abb81f)
- López-Vázquez, J. A., Lee, C.-F., Shang, H., et al. 2024, arXiv e-prints, arXiv:2411.01728, doi: [10.48550/arXiv.2411.01728](https://doi.org/10.48550/arXiv.2411.01728)
- Mairs, S., Johnstone, D., Kirk, H., et al. 2017, ApJ , 849, 107, doi: [10.3847/1538-4357/aa9225](https://doi.org/10.3847/1538-4357/aa9225)
- Matzner, C. D., & McKee, C. F. 2000, The Astrophysical Journal, 545, 364–378, doi: [10.1086/317785](https://doi.org/10.1086/317785)
- Maud, L. T., Lumsden, S. L., Moore, T. J. T., et al. 2015a, MNRAS , 452, 637, doi: [10.1093/mnras/stv1334](https://doi.org/10.1093/mnras/stv1334)
- Maud, L. T., Moore, T. J. T., Lumsden, S. L., et al. 2015b, Monthly Notices of the Royal Astronomical Society, 453, 645–665, doi: [10.1093/mnras/stv1635](https://doi.org/10.1093/mnras/stv1635)
- McKee, C. F., & Tan, J. C. 2003, ApJ , 585, 850, doi: [10.1086/346149](https://doi.org/10.1086/346149)
- Mignon-Risse, R., González, M., & Commerçon, B. 2021, Astronomy & Astrophysics, 656, A85, doi: [10.1051/0004-6361/202141648](https://doi.org/10.1051/0004-6361/202141648)
- Minier, V., Ellingsen, S. P., Norris, R. P., & Booth, R. S. 2003, Astronomy & Astrophysics, 403, 1095–1100, doi: [10.1051/0004-6361:20030465](https://doi.org/10.1051/0004-6361:20030465)
- Motte, F., Bontemps, S., Csengeri, T., et al. 2022, Astronomy & Astrophysics, 662, A8, doi: [10.1051/0004-6361/202141677](https://doi.org/10.1051/0004-6361/202141677)
- Müller, H. S., Schlöder, F., Stutzki, J., & Winnewisser, G. 2005, Journal of Molecular Structure, 742, 215–227, doi: [10.1016/j.molstruc.2005.01.027](https://doi.org/10.1016/j.molstruc.2005.01.027)
- Müller, H. S. P., Thorwirth, S., Roth, D. A., & Winnewisser, G. 2001, Astronomy & Astrophysics, 370, L49–L52, doi: [10.1051/0004-6361:20010367](https://doi.org/10.1051/0004-6361:20010367)

- Nakamura, F., & Li, Z.-Y. 2012, in AIP Conference Proceedings (AIP), 30–37, doi: [10.1063/1.4754324](https://doi.org/10.1063/1.4754324)
- Nakano, T., Hasegawa, T., & Norman, C. 1995, ApJ , 450, 183, doi: [10.1086/176130](https://doi.org/10.1086/176130)
- Nutter, D., Ward-Thompson, D., & André, P. 2006, MNRAS , 368, 1833, doi: [10.1111/j.1365-2966.2006.10249.x](https://doi.org/10.1111/j.1365-2966.2006.10249.x)
- Offner, S. S. R., Lee, E. J., Goodman, A. A., & Arce, H. 2011, The Astrophysical Journal, 743, 91, doi: [10.1088/0004-637x/743/1/91](https://doi.org/10.1088/0004-637x/743/1/91)
- Pattle, K., & Ward-Thompson, D. 2015, in IAU General Assembly, Vol. 29, 2245772
- Plunkett, A., Arce, H., Mardones, D., et al. 2015, Nature, 527, 70, doi: [10.1038/nature15702](https://doi.org/10.1038/nature15702)
- Pokhrel, R., Myers, P. C., Dunham, M. M., et al. 2018, The Astrophysical Journal, 853, 5, doi: [10.3847/1538-4357/aaa240](https://doi.org/10.3847/1538-4357/aaa240)
- Pontoppidan, K. 2023, Rho Ophiuchi (NIRCAM image) | Webb. <https://webbtelescope.org/contents/media/images/2023/128/01H449193V5Q4Q6GFBKXAZ3S03?news=true>
- Preibisch, T., & Zinnecker, H. 1999, AJ , 117, 2381, doi: [10.1086/300842](https://doi.org/10.1086/300842)
- Pudritz, R. E., & Ray, T. P. 2019, Frontiers in Astronomy and Space Sciences, 6, doi: [10.3389/fspas.2019.00054](https://doi.org/10.3389/fspas.2019.00054)
- Purcell, C. R. 2006, PhD thesis, University of New South Wales, Australia
- Reipurth, B., & Bally, J. 2001, ARA&A , 39, 403, doi: [10.1146/annurev.astro.39.1.403](https://doi.org/10.1146/annurev.astro.39.1.403)
- Richer, J. S., Shepherd, D. S., Cabrit, S., Bachiller, R., & Churchwell, E. 2000, in Protostars and Planets IV, ed. V. Mannings, A. P. Boss, & S. S. Russell, 867, doi: [10.48550/arXiv.astro-ph/9904097](https://arxiv.org/abs/astro-ph/9904097)
- Robitaille, T. P., Whitney, B. A., Indebetouw, R., Wood, K., & Denzmore, P. 2006, ApJS , 167, 256, doi: [10.1086/508424](https://doi.org/10.1086/508424)
- Rohde, P. F., Walch, S., Clarke, S. D., et al. 2020, Monthly Notices of the Royal Astronomical Society, 500, 3594–3612, doi: [10.1093/mnras/staa2926](https://doi.org/10.1093/mnras/staa2926)
- Rosen, A. L., Krumholz, M. R., McKee, C. F., & Klein, R. I. 2016, MNRAS , 463, 2553, doi: [10.1093/mnras/stw2153](https://doi.org/10.1093/mnras/stw2153)
- Rosen, A. L., Offner, S. S. R., Sadavoy, S. I., et al. 2020, SSRv , 216, 62, doi: [10.1007/s111214-020-00688-5](https://doi.org/10.1007/s111214-020-00688-5)
- Safron, E. J., Fischer, W. J., Megeath, S. T., et al. 2015, ApJL , 800, L5, doi: [10.1088/2041-8205/800/1/L5](https://doi.org/10.1088/2041-8205/800/1/L5)

- Schilke, P., Walmsley, C. M., Pineau des Forets, G., & Flower, D. R. 1997, A&A , 321, 293
- Shu, F. H., Adams, F. C., & Lizano, S. 1987, ARA&A , 25, 23, doi: [10.1146/annurev.aa.25.090187.000323](https://doi.org/10.1146/annurev.aa.25.090187.000323)
- Skrutskie, M. F., Cutri, R. M., Stiening, R., et al. 2006, The Astronomical Journal, 131, 1163–1183, doi: [10.1086/498708](https://doi.org/10.1086/498708)
- Staff, J. E., Tanaka, K. E. I., & Tan, J. C. 2019, The Astrophysical Journal, 882, 123, doi: [10.3847/1538-4357/ab36b3](https://doi.org/10.3847/1538-4357/ab36b3)
- Stahler, S. W. 1994, ApJ , 422, 616, doi: [10.1086/173754](https://doi.org/10.1086/173754)
- Sutton, E. C., Peng, R., Danchi, W. C., et al. 1995, The Astrophysical Journal Supplement Series, 97, 455, doi: [10.1086/192147](https://doi.org/10.1086/192147)
- Tan, J. C., Beltrán, M. T., Caselli, P., et al. 2014, in Protostars and Planets VI, ed. H. Beuther, R. S. Klessen, C. P. Dullemond, & T. Henning, 149–172, doi: [10.2458/azu_uapress_9780816531240-ch007](https://doi.org/10.2458/azu_uapress_9780816531240-ch007)
- Towner, A. P. M., Ginsburg, A., Dell’Ova, P., et al. 2023, The Astrophysical Journal, 960, 48, doi: [10.3847/1538-4357/ad0786](https://doi.org/10.3847/1538-4357/ad0786)
- Turner, B. E. 1991, The Astrophysical Journal Supplement Series, 76, 617, doi: [10.1086/191577](https://doi.org/10.1086/191577)
- Tychoniec, Ł., Hull, C. L. H., Kristensen, L. E., et al. 2019, A&A , 632, A101, doi: [10.1051/0004-6361/201935409](https://doi.org/10.1051/0004-6361/201935409)
- Van der Marel, N., Kristensen, L. E., Visser, R., et al. 2013, Astronomy & Astrophysics, 556, A76, doi: [10.1051/0004-6361/201220717](https://doi.org/10.1051/0004-6361/201220717)
- van der Tak, F. F. S., Black, J. H., Schöier, F. L., Jansen, D. J., & van Dishoeck, E. F. 2007, Astronomy & Astrophysics, 468, 627–635, doi: [10.1051/0004-6361:20066820](https://doi.org/10.1051/0004-6361:20066820)
- Van Kempen, T. A., van Dishoeck, E. F., Salter, D. M., et al. 2009, Astronomy & Astrophysics, 498, 167–194, doi: [10.1051/0004-6361/200810445](https://doi.org/10.1051/0004-6361/200810445)
- Van Kempen, T. A., Hogerheijde, M. R., van Dishoeck, E. F., et al. 2016, Astronomy & Astrophysics, 587, A17, doi: [10.1051/0004-6361/201424725](https://doi.org/10.1051/0004-6361/201424725)
- Velusamy, T., & Langer, W. D. 1998, Nature , 392, 685, doi: [10.1038/33624](https://doi.org/10.1038/33624)
- Walsh, A. J., Burton, M. G., Hyland, A. R., & Robinson, G. 1999, Monthly Notices of the Royal Astronomical Society, 309, 905–922, doi: [10.1046/j.1365-8711.1999.02890.x](https://doi.org/10.1046/j.1365-8711.1999.02890.x)
- Whitney, B. A., Wood, K., Bjorkman, J. E., & Wolff, M. J. 2003, ApJ , 591, 1049, doi: [10.1086/375415](https://doi.org/10.1086/375415)

- Wienen, M., Wyrowski, F., Menten, K. M., et al. 2015, *Astronomy & Astrophysics*, 579, A91, doi: [10.1051/0004-6361/201424802](https://doi.org/10.1051/0004-6361/201424802)
- Wilking, B. A., Gagné, M., & Allen, L. E. 2008, in *Handbook of Star Forming Regions, Volume II*, ed. B. Reipurth, Vol. 5, 351, doi: [10.48550/arXiv.0811.0005](https://arxiv.org/abs/0811.0005)
- Woosley, S. E., Heger, A., & Weaver, T. A. 2002, *Reviews of Modern Physics*, 74, 1015, doi: [10.1103/RevModPhys.74.1015](https://doi.org/10.1103/RevModPhys.74.1015)
- Wu, Y., Wei, Y., Zhao, M., et al. 2004, *A&A* , 426, 503, doi: [10.1051/0004-6361:20035767](https://doi.org/10.1051/0004-6361:20035767)
- Yıldız, U. A., Kristensen, L. E., van Dishoeck, E. F., et al. 2012, *Astronomy & Astrophysics*, 542, A86, doi: [10.1051/0004-6361/201118368](https://doi.org/10.1051/0004-6361/201118368)
- Zhang, Q., Wang, K., Lu, X., & Jiménez-Serra, I. 2015, *The Astrophysical Journal*, 804, 141, doi: [10.1088/0004-637x/804/2/141](https://doi.org/10.1088/0004-637x/804/2/141)